Double Nanohole Optical Tweezer for Single Molecule and Nanoparticle Analysis

by

Abhay Kotnala
B.Eng., Kumaun University, 2007
M.Tech., Indian Institute of Technology Banaras Hindu University, 2009

A Dissertation Submitted in Partial Fulfillment
of the Requirements for the Degree of

DOCTOR OF PHILOSOPHY

in the Department of Electrical and Computer Engineering

Supervisory Committee

Double Nanohole Optical Tweezer for Single Molecule and Nanoparticle Analysis

by

Abhay Kotnala
B.Eng., Kumaun University, 2007
M.Tech.,Indian Institute of Technology, Banaras Hindu University, 2009

Supervisory Committee

Dr. Reuven Gordon, Department of Electrical and Computer Engineering
Supervisor

Dr. Tao Lu, Department of Electrical and Computer Engineering
Departmental Member

Dr. Martin Byung-Guk Jun, Department of Mechanical Engineering
Outside Member

Abstract

Supervisory Committee

Dr. Reuven Gordon, Department of Electrical and Computer Engineering
Supervisor

Dr. Tao Lu, Department of Electrical and Computer Engineering
Departmental Member

Dr. Martin Byung-Guk Jun, Department of Mechanical Engineering
Outside Member

This dissertation presents novel techniques applied to double nanohole (DNH) optical tweezer with the idea of characterizing and developing capabilities of nanoaperture trap, for single molecule and nanoparticle analysis. In addition, an alternative approach for fabrication of double nanoholes using template stripping is presented. The strength of the DNH tweezer was characterized quantitatively in terms of trap stiffness using two techniques: autocorrelation of Brownian-induced intensity fluctuations and trapping transient. These experimental techniques have, for the first time, been applied to an aperture based trap used for trapping Rayleigh particles in the range of few nanometres. These techniques can be used for calibration and comparison of the aperture based traps among themselves and with other nano-optical tweezers. A statistical technique based on the parameters, time-to-trap and the transient jump due to optical trapping was used for sensing the concentration, size and refractive index of the nanoparticles. The time-to-trap showed a linear dependence with particle size and a -2/3 power dependence with particle concentration, which is in agreement with the diffusion theory based on simple microfluidic considerations. The transient jump in the trapping signal at the trapping instant scales empirically as the Clausius–Mossotti factor for different refractive index particles. The ability of the DNH tweezer to hold small Rayleigh particles with high efficiency and also the increased sensitivity of the transmission signal to the trapped

particle during detection makes it favourable for studying the dynamics and interactions of biomolecules. In this direction, the unzipping of the hairpin DNA and its interaction with the tumour suppressor p53 transcription protein, which suppresses the unzipping, were detected using double nanohole optical tweezer. The energy associated with the suppression of unzipping was found to be close to the binding energy of p53-DNA complex. The mutant p53 inability to supress the unzipping of the DNA was also confirmed, showing the ability of the DNH tweezer to distinguish between the mutant p53 and the wild-type. An extraordinary acoustic Raman (EAR) technique was used to study the vibrational modes of ssDNA molecule. The resonant vibrational modes were found to be in the sub 100 GHz range and could be tuned based on the base sequence and length of the DNA strand. The vibrational modes were verified using 1-D lattice vibration theory. Finally, an alternative approach of template stripping for fast and cheaper fabrication of DNH is presented. The template strip process can be used reliably for mass production of gold slide containing DNH's and also results in cost reduction by 70 % for a single gold slide. Also, we have successfully used this approach to transfer DNH structure to the tip of the cleaved fiber, which would make the DNH tweezer module more compact and scalable. This would open up opportunities for many other applications for single molecule and nanoparticle analysis such as transfer of molecules in-situ to other biomolecular solution for studying their interactions and many others.

Table of Contents

Supervisory Committee ii
Abstract iii
Table of Contents v
List of Tables vii
List of Figures viii
Acknowledgments xiii
Dedication xiv
Glossary xv
Chapter 1. Introduction 1
1.1 Optical Tweezers 1
1.2 Applications of Optical Tweezers 3
1.3 Limitation of Conventional Optical Tweezers 6
1.4 Nano-Optical Tweezers (Enhanced gradient force based plasmonic tweezers) . 8
1.5 Limitations of Enhanced Gradient Force based Plasmonic Nano-optical Tweezers 11
1.6 Motivation and Contribution of Thesis 13
Chapter 2. Nanoaperture Tweezers 18
2.1 Introduction 18
2.2 Stable Trapping of Rayleigh Particles 18
2.3 Bethe's Theory 21
2.4 Nanoaperture Tweezers: Principle, Design and Detection 24
2.4.1 Principle: Self-Induced Back Action (SIBA) Trapping 24
2.4.2 Design 26
2.4.3 Detection 27
2.5 DNH Optical Tweezer Experimental Set-up 29
2.6 Fabrication of DNH 31
2.7 Chip Assembly 34
2.8 Characteristics of Nanoaperture Tweezers 35
2.8.1 Single Molecule Trapping 36
2.8.2 Free-solution and Label-free 38
2.8.3 Temperature 39
2.8.4 High SNR 41
2.8.5 Easy to Integrate 41
2.8.6 Other 41
Chapter 3. Quantification of DNH Stiffness 43
3.1 Introduction 43
3.2 Theory 45
3.2.1 Autocorrelation of Brownian-Induced Intensity Fluctuations 45
3.2.2 Trapping Transient Analysis 46
3.2.3 Trap Stiffness Calculation 47

3.3 Experiment and Results 50
3.4 Discussion 55
Chapter 4. DNH Optical Tweezers for Sensing 58
4.1 Introduction 58
4.2 Theory 58
4.2.1 Time-to-trap as a Function of Size of Nanoparticles 59
4.2.2 Time-to-trap as a Function of Concentration of Nanoparticles 60
4.3 Experiment and Results 60
4.3.1 Procedure 63
4.3.2 Nanoparticle Size Sensing 65
4.3.3 Nanoparticle Concentration Sensing 66
4.3.4 Nanoparticle Refractive Index Sensing 67
4.3.5 Heterogeneous Populations 70
4.4 Discussion 71
Chapter 5. Single Molecule Protein-DNA Interactions using DNH Tweezer 73
5.1 Introduction 73
5.2 Experiment and Results 74
5.2.1 Unzipping of 20 base Hairpin DNA (Stem-loop Configuration) 75
5.2.2 Wild-type p53 Interaction with Hairpin DNA 78
5.2.3 p53 Mutant (cys135ser) Interaction with Hairpin DNA 80
5.2.4 p53 Mutant and Wild-type Trapping 82
5.3 Discussion 83
Chapter 6. Mapping Low Frequency Vibrational Spectra of ssDNA 85
6.1 Introduction 85
6.2 Theory 86
6.2.1 Application of 1-D Lattice Vibration Theory to ssDNA 87
6.3 Experimental Set-up 91
6.4 Experiment and Results 94
6.5 Impact of Size and Sequence of ssDNA on the Vibrational Spectrum 96
6.6 Discussion 99
Chapter 7. Conclusion and Outlook 101
7.1 Conclusion of Thesis 101
7.2 Future Work 103
7.2.1 Intercalation of DNA 103
7.2.2 Conformational Dynamics using Intensity Modulation of Trapping Laser 103
7.2.3 Compact Lab-on-chip Tweezer 104
7.2.4 Integration with Other Single Molecule Techniques 105
Bibliography 107
Appendix A. Fabrication of DNH using Template Stripping 121
A.1 Introduction 121
A.2 Template Stripped DNHs 122
Appendix B. Microfluidic DNH Chip for Sensing Applications 127
B.1 Microfluidic Chip for Optical Trapping 127

List of Tables

Table 3.1Comparison of trap stiffness for different optical traps scaled for 10 nm dielectric sphere. a Exp.: Experimental, Sim.: Simulation, b Scaled by Clausius-Mossotti factor to account for increased refractive index contrast used in calculations. 56
Table 6.1 Different length sequences of ssDNA used for trapping and measurement of the corresponding vibrational spectrum. The total mass (m) of the ssDNA is the sum of mass of individual bases A, T, G, C in the specimen and M is the average mass obtained by dividing the total mass (m) by the total number of bases (N_b) for the given ssDNA. . 97
Table 6.2 Different sequences of 30 base ssDNA used for trapping and measurement of the corresponding vibrational spectrum. The total mass (m) of the ssDNA is the sum of mass of individual bases A, T, G, C in the specimen and M is the average mass obtained by dividing total mass with number of bases for a single strand of DNA. 98

List of Figures

Figure 1.1 (a) The gradient and scattering force acting on a dielectric particle displaced from the axis of a Gaussian laser beam. The curved lines at the left and right represent the shape of the laser beam and the Gaussian curve represent the intensity profile of the beam. Two rays of light from the laser beam are shown as a and b. The refraction of light by the particle changes the momentum of the photons, which results in the forces F_a and F_b. (b) Conventional optical tweezer use strongly focussed beam of light to trap object such as the colloidal particles. The intensity gradient pulls the particle towards the focus, while the radiation pressure of the beam pushes the particle along the optical axis. Higher gradient forces in comparison to scattering forces due to radiation pressure results in formation of a stable three dimension trap [8]. Figure reprinted with permission from Ref. [8]. 2
Figure 1.2 (a) Schematic of an experiment using optical tweezers for the measurement of the forces on an optically trapped sphere and the extension of the DNA-protein complex. The different curves show typical stretching curve of DNA [28], stalling of a protein filament assembly and force damping [29] and translocation and pausing by RNA polymerase [30]. (b) Unwinding of DNA hairpin by helicases using optical tweezers. (c) Optical tweezer with fluorescence microscopy of fluorescently labelled proteins for measurement of real time binding, unbinding on DNA [31, 32]. Figure reprinted with permission from Ref. [26]. 6
Figure 1.3 Nanostructures used for optical trapping (a) sharp metallic tip*(1997) [36] (b) nanoaperture in opaque metal film* (1999) [38] (c) gold disks# (2007) [39] (d) nanopillars #(2008) [43] (e) nanobars #(2009) (f) bowtie# (2012) [44] (g) tunable microcavities* (2008) [48] (h) slot waveguide# (2009) [11] (i) plasmonic nanoblock pair# (2013) [49] . * Theoretical, # Experimental. Figure reprinted with permission from corresponding References. 11
Figure 2.1 Schematic illustration of conventional tweezer, nano-optical tweezer and aperture tweezer showing the SIBA effect along with their corresponding potential energy profile. Conventional tweezers trap nanoparticles at the focal point of the laser beam and form a Gaussian trapping potential well with trapping space of nearly equal to the diffraction limit of light. The plasmonic tweezer trap particle in the confined active nanospace which in the present case is the area between the cusps of the DNH. The potential energy profile depends on the shape of the structure and is much smaller than the diffraction limit of light. The SIBA based trap provide a dynamic potential energy change by the presence of the particle in the active area by increasing the potential depth as the particle tries to escape from the active trapping area. 21
Figure 2.2 Optical transmission through a single subwavelength hole: (a) without particle; (b) transmission enhanced with a dielectric particle in the hole (dielectric loading). The presence of the dielectric particle makes the hole optically larger through dielectric loading, red-shifting the transmission curve and giving the change ΔT in transmission. 23

Figure 2.3 The numerically computed optical force in the circular nanohole optical trap based on FDTD simulations, while trapping 100 nm polystyrene spheres. Two physical formulations are compared: the comprehensive MST analysis and the perturbative gradient force approximation. It is found that the perturbative gradient force approximation is no longer a good approximation for computing optical forces in a circular aperture trap, and the MST analysis predicts a much larger optical force than the gradient approximation does [62]. Figure reprinted with permission from Ref. [62]. 26
Figure 2.4 Nanoaperture designs (a) Circular aperture [61] (b) Rectangular plasmonic nanocavity [64] (c) Double nanohole aperture [65] (d) Bowtie nanoaperture (BNA) at the fiber tip [66] (e) Coaxial nanoaperture [67]. Figures reprinted with permission from corresponding References. 27
Figure 2.5 The fluorescence and transmission signal through the bowtie nanoaperture (BNA) as a function of time. The step change in the fluorescence signal (blue) and the transmission signal (red) at around t=23 sec corresponds to the trapping of the single 20 nm polystyrene nanosphere in the BNA. Figure reprinted with permission from Ref. [66]. 28
Figure 2.6 Schematic of optical trapping experiment. Abbreviations used: ODF: optical density filter; HWP: half wave plate; BE: beam expander; MR: mirror; OIMO: oil immersion microscope objective; APD: avalanche photodiode; DAQ: data acquisition card. 31
Figure 2.7 Scanning electron microscope (SEM) images of DNH showing the impact of the milling time (milling time=dwell time × number of passes) on the DNH structure. The dwell time was fixed to 5μs and the numbers of passes were varied. (a) 20 pass (b) 30 pass (c) 40 pass (d) 50 pass. The gap is not milled completely for less than 40 passes, while increasing above 40 passes might increase the cusps gap width beyond the desired size. 32
Figure 2.8 (a) Bitmap image used to make DNH using FIB. (b) Typical SEM image of the DNH. (c) CCD image of the DNH encircled by ring used as marker on the gold sample. The red spot at the center shows the laser spot focused on the DNH. 34
Figure 2.9 (a) 3-D perspective of the chip containing the nanoparticles. It shows the gold sample with DNH and the chamber with nanoparticles suspended in water. (b) Front view schematic of the chip placed between the oil immersion objective and the condenser lens. 35
Figure 2.10 Optical trapping event showing trapping of more than one particle at the DNH trap site after some interval of time. This is random and a rare event as has been seen throughout the work and can be discarded while doing statistical analysis of the data. 38
Figure 2.11 (a) SEM image of the split hole resonator (SHR) nanoaperture (b) Temperature distribution on the surface of the SHR nanostructure not exceeding 300 K, much below the destruction threshold of the metal [71]. Figure reprinted with permission from Ref. [71] 40
Figure 3.1 Restoring force acting on the particle, when the particle is displaced by x from the center of the potential well at $x = 0$. Analogous illustration showing the particle connected to a stationary block by a Hookean spring. When the particle is displaced from the center position, a restoring force acts on the particle which is defined in terms of the spring constant κ of the spring. 44

Figure 3.2 Typical time trace of a trapping event of 20 nm polystyrene nanosphere using DNH. The DNH has a gap nearly 28 nm. The transmission signals through the DNH for t< 30.28 s (black) shows the untrapped signal with no particle. At nearly t=30.28s there is a step change in the transmission corresponding to the trapping transient of the particle. For t > 30.3s the particle is trapped in the DNH aperture with large Brownian-induced intensity fluctuation as shown in the transmission signal (red). The transmission signal is down sampled to 1 KHz. 51
Figure 3.3 Autocorrelation function of the transmission signal in the untrapped (blue) and trapped (red) state. The autocorrelation is taken for a section of the transmission signal through the DNH aperture of length 2-3 s to accurately determine the autocorrelation function. 52
Figure 3.4 (left) Potential energy diagram showing the particle being sucked into the potential well against the viscous drag due to the surrounding medium. (Right) Trapping transient (blue) showing the change in transmission signal through the DNH aperture from untrapped to trapped state as the particle enters the trapping region. The signal is the zoomed version of the transient signal (blue) as shown in Figure 3.2, with an exponential fit (red) to determine the transient time(τ_t). 53
Figure 3.5 Mean characteristic time constants (left axis) and trap stiffness (right axis) calculated using the autocorrelation of Brownian-induced intensity fluctuations (red) and trapping transient (black) methods for different incident laser power obtained from multiple trapping events at each power value (N > 10). 55
Figure 4.1 Experimental setup of the DNH tweezer for use as a sensor. A microfluidic chip is used for optical trapping and the solution is flowed into the channel using a syringe pump. A detailed view and fabrication details of the microfluidic chip is presented in Appendix B. 62
Figure 4.2 SEM images of DNH with different cusp gap size for efficient trapping of different size of nanoparticles (a) 28 nm (b) 50 nm (c) 68 nm 62
Figure 4.3 Typical trapping event for 0.1 w/v % concentration of 20 nm polystyrene particle. The laser was turned on at t=362.5 s and used as reference to measure the time to trap which occurs at approximately t=455 s. (b) Distribution of time-to-trap (tt) for 60 nm polystyrene particles with Rayleigh fit. 63
Figure 4.4 Time series of two consecutive trapping events for 0.1 w/v % of 20 nm polystyrene nanospheres, showing switching of the laser beam on and off and the release of the particle. The laser is turned off for nearly 70 s before turning it on. 64
Figure 4.5 Mean time-to-trap for different polystyrene spheres of diameters 20 nm, 40 nm and 60 nm. The horizontal and vertical error bars are standard deviation (manufacturer specified) and standard error of nanosphere size and trapping time respectively. The straight line represents linear fit to the data. 66
Figure 4.6 Average time-to-trap for varying concentrations of 20 nm polystyrene nanospheres in aqueous solution on a log-log scale. The dot represents the mean trapping time over multiple events (typically 10-20) for each concentration. The bar represents the standard error of the data. The straight line represents the power fit to the data. 67
Figure 4.7 Percentage change in the transmission signal measured at the trapping instant when the particle goes from the untrapped to trapped state for different refractive index particles, silica (n=1.46), polystyrene (n=1.57) and Titania (n= 2.44). The dot represents

the mean value of the percent voltage change for multiple trapping events (N >10) and the error bar the standard deviation in the data. 69
Figure 4.8 Typical trapping event of trapping of 20 nm silica, polystyrene and titania spheres. The percentage change in transmission is more for a higher refractive index particle..... 70
Figure 5.1 SEM image of the DNH with cusp separation of ~ 10 nm used for trapping the ssDNA and the protein. 75
Figure 5.2 (a) Typical optical trapping event of a single strand DNA. (b) Typical trapping event of hairpin DNA showing the unzipping with an intermediate step of ~ 100 ms. (c) Energy reaction diagram of single strand DNA. (d) Energy reaction diagram showing the change in the potential energy diagram due to the energy barrier provided by the base pairing in the stem region. k_B: Boltzmann constant, T: Temperature 77
Figure 5.3 p53 interaction with DNA hairpin (a) Typical trapping event of p53 protein-DNA complex showing an increase in the intermediate step of ~ 5s (b) Energy reaction model showing the increase in the unzipping barrier by ΔU due to the binding of the p53 protein with the consensus hairpin DNA. 79
Figure 5.4 (a) Typical trapping event of mutant p53 protein-DNA complex showing an intermediate step of ~ 50 ms (b) A comparison of the cumulative probability distribution of the unzipping times Δt for hairpin DNA, wild-type p53-DNA and mutant p53–DNA. The wild type p53 can be easily distinguished from its mutant form based on the unzipping time distribution. 81
Figure 5.5 Distribution of the unzipping times Δt for hairpin DNA, wild-type p53-DNA and mutant p53–DNA complex for multiple events with a log-normal fit. The distribution of the hairpin and mutant-DNA overlap over similar range of unzipping times, showing minimum effect of the mutant in acting against the unzipping of the hairpin. 82
Figure 5.6 Typical optical trapping event of individual p53 protein for both wild-type and its mutant (Cys135Ser). 83
Figure 6.1 Model of ssDNA as a linear chain of atoms with mass M that are connected by effective springs with a spring constant κ. The mass is the average mass obtained from the total mass of ssDNA chain divided by the number of bases in the DNA strand. The distance between the bases is, a , and the length of the ssDNA is L. 88
Figure 6.2 Slightly detuned lasers showing the beating laser signal leading to the modulation of the electrostriction force which excites the vibrational modes of the particle..... 91
Figure 6.3 Double nanohole dual-laser optical tweezer setup. Abbreviations: optical spectrum analyzer (OSA), fiber coupler (50/50), fiber polarization controller (FPC), fiber launcher (FL), optical isolator (ISO), half wave plate (HWP), 45 degree mirror (MIR), dichroic reflector (DI), optical density filter (ODF), avalanche photodiode (APD), charged coupled device camera (CCD). 92
Figure 6.4 (a) Intensity fluctuations and corresponding Gaussian fit of the transmission signal through the DNH aperture for a trapped 20 base ssDNA. The transmission signal 30-60 sec (blue) corresponds to the non–resonant beat frequency points in the frequency range, f=13-15 GHz (solid, blue) and the transmission signal 350-380 sec (red) correspond to the near–resonant beat frequency points from 38.5-40.5 GHz as shown in figure 6.4b (solid, red) (b) Normalized RMSD as a function of scanned beat frequencies showing resonance at 40 GHz..... 95

Figure 6.5 Normalized root mean squared (RMS) deviation of the scattered transmission signal for (a) 20 base ssDNA showing the fundamental resonant frequency at f=39 GHz and a second order harmonic at f=73 GHz. (b) 30 base ssDNA showing the fundamental resonant frequency at f=28.3 GHz and a second order harmonic at f=58GHz. 96
Figure 6.6 Resonant mode frequency as a function of number of bases of ssDNA molecule. The line (black) shows the mean resonant frequency along with the standard deviation found experimentally. The circles (red) are the resonant frequency calculated by modelling ssDNA using 1-D lattice vibration theory. 97
Figure 6.7 Resonant frequencies of three different sequences of 30 base ssDNA molecules (Seq. 1: MW 4336.2 Da, Seq. 2: MW 3895.9 Da, Seq. 3: MW 3463.4 Da). The solid circles (black) shows the mean resonant frequency along with the standard deviation found experimentally. The circles (red) are the resonant frequency calculated by modelling ssDNA using the 1-D lattice vibration theory. 99
Figure 7.1 (Left) Tilted SEM image of the optical fiber with gold on the tip of the cleaved end and the SEM image of the DNH milled into the active region of the fiber. (Right) Trapping event for a 20 nm polystyrene sphere in a DNH on the cleaved end of a fiber. 105
Figure A.1 Process flow for fabrication of template stripped DNH. 124
Figure A.2 (a, b) Template stripped DNH fabricated from the silicon template shown in Figure c and d respectively. 125
Figure B.1 Fabrication procedure flow diagram showing the making of a microfluidics chip along with DNH integration. 129
Figure B.2 (a) Top view of the chip. (b) Side view of the chip. (c) Aluminum clamp. . 130

Acknowledgments

गुरुर्ब्रह्मागुरुर्विष्णुर्गुरुर्देवोमहेश्वरः।
गुरुरेवपरंब्रह्मतस्मैश्रीगुरवेनमः॥१॥

(Guru is like Brahma, the creator who inculcates knowledge in the mind of students. Guru is like Vishnu, the preserver who helps in keeping up the knowledge and like Shiva, the destroyer, who destroys and gets rid of the ignorance from the student mind. The one who is beyond all attributes and forms and is the supreme self (the Brahman). I salute to that guru.)

First of all, I would like to acknowledge Dr. Reuven Gordon who has been a "*guru*" who according to the Indian philosophy is much more than a teacher, a supervisor. He introduced me to the fascinating field of Optical Tweezers and through his guidance I learnt the skills and the temperament for research. I am also grateful to him for providing me the financial assistance during my research without which everything would be impossible.

I would also like to thank the other dissertation committee members, Dr. Tao Lu and Dr.Martin Byung-Guk Jun, as well as the outside examiner Dr.Peter Pauzauskie, for providing valuable suggestions for improving my dissertation. In addition, I would like to thank Dr. Elaine Humphrey and Adam Schuetze for helping me in nanofabrication and imaging.

I thank to all my lab members for all the help, motivation and fun during my work as a PhD student. I also thank the ECE department administrative staff for the cooperation and assistance during the PhD. At last I would thank the University for providing me the University of Victoria Fellowship, The Graduate Award and other financial assistance.

Last but not the least; I dedicate this thesis to my parents who from my birth have constantly provided a spiritual energy in their blessings which has brought me to this stage.

Dedication

To …

Glossary

List of symbols:

α	Polarizability
E	Electric Field
n	Refractive Index
k_B	Boltzmann Constant
T	Temperature
U	Potential Energy
r	Radius
p	Dipole Moment
I	Intensity
λ	Wavelength
H	Magnetic Field
Z_o	Free Space Impedance
κ	Trap Stiffness
γ	Stokes' Drag Coefficient
$\zeta(t)$	White Noise
τ	Time Constant
h	Height
η	Viscosity
D	Diffusion Constant
l	Diffusion Length
ε	Permittivity
ω_r	Resonant frequency
β	Propagation Constant

Abbreviation

APD	Avalanche Photodiode
bp	Base pair
BSA	Bovine Serum Albumin
CCD	Charge Coupled Device
CYS	Cysteine
DNA	Deoxyribonucleic Acid
DNH	Double Nanohole
dsDNA	Double Strand DNA
FIB	Focussed Ion Beam
FL	Fiber Launcher
FPC	Fiber Polarization Controller

HWP	Half Wave Plate
mPEG	Methoxy Poly-ethylene Glycol
MST	Maxwell Stress Tensor
NA	Numerical Aperture
ODF	Optical Density Filter
OIMO	Oil Immersion Microscope Objective
OSA	Optical Spectrum Analyser
QPD	Quadrant Photodiode
RMS	Root Mean Squared
RNA	Ribonucleic Acid
SEM	Scanning Electron Microscope
SER	Serine
SERS	Surface Enhanced Raman Scattering
SIBA	Self-induced Back Action
SNR	Signal to Noise Ratio
SPR	Surface Plasmon Resonance
ssDNA	Single Strand DNA
TEC	Thermo-Electric Cooling
w/v %	Weight by Volume Percentage
WGM	Whispering Gallery Modes

Chapter 1. Introduction

1.1 Optical Tweezers

The fundamental unit of light called photon carries linear and angular momentum and therefore can exert force or torque on the interacting particles. This idea was first conceptualized by Maxwell known as the radiation pressure of light and electromagnetic waves [1, 2]. The forces originating from the light were very small as compared to the physical forces of friction and gravitation and could not find practical application in real world. However, it was in 1969, when Arthur Ashkin realized that though the forces are small, they are enough to move very small particles [3]. This idea was put into practise by Ashkin to guide and levitate small particles [4, 5]. During these experiments he found that the radiation pressure consists of two basic force components acting on the particle. One is the longitudinal component known as scattering force acting in the direction of the beam and the other transverse component known as gradient force acting in the direction of the intensity gradient of the beam as shown in Figure 1.1a. The knowledge of the magnitude and the properties of these forces led to the realization of a stable three dimensional trap in 1986 [6]. In this seminal work, Ashkin used optical gradient force for trapping of dielectric particles using a single focussed laser beam. This technology was later termed as **Optical Tweezer**. The optical tweezer provides a non- invasive technique to hold and manipulate single particle of interest and study the particle as shown in Figure 1.1b. The work of this thesis falls into the broad category of Optical Tweezers.

The optical tweezer produces forces in the range extending from femtonewton (fN) to nanonewton (nN). Since most of the fundamental molecular processes occur at the spatiotemporal scales of angstrom (Å) to nanometres (nm) and milliseconds (ms) to seconds (s), these ranges of forces are ideal for holding, manipulating and measuring response of biological and macromolecular systems. The applications are mostly based on the application of calibrated forces on the system and accurate measurement of the forces and displacement associated with the dynamics of the system [7].

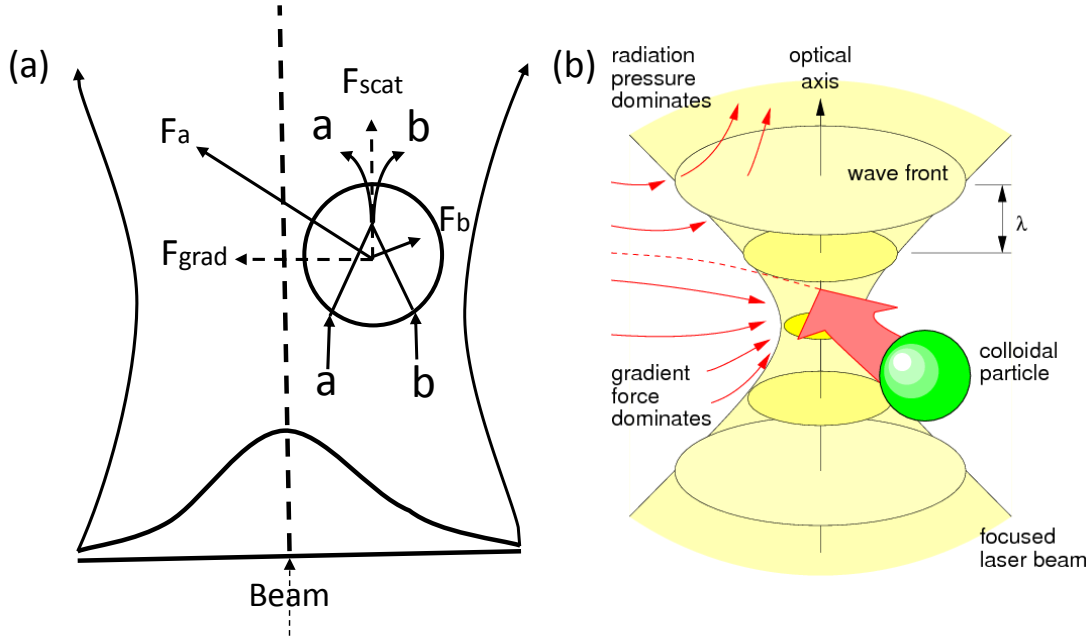

Figure 1.1 (a) The gradient and scattering force acting on a dielectric particle displaced from the axis of a Gaussian laser beam. The curved lines at the left and right represent the shape of the laser beam and the Gaussian curve represent the intensity profile of the beam. Two rays of light from the laser beam are shown as a and b. The refraction of light by the particle changes the momentum of the photons, which results in the forces F_a and F_b. (b) Conventional optical tweezer use strongly focussed beam of light to trap object such as the colloidal particles. The intensity gradient pulls the particle towards the focus, while the radiation pressure of the beam pushes the particle along the optical axis. Higher gradient forces in comparison to scattering

forces due to radiation pressure results in formation of a stable three dimension trap [8]. Figure reprinted with permission from Ref. [8].

1.2 Applications of Optical Tweezers

The applications of optical tweezer range from biophysics, chemistry to material science and various other related fields. Among most of the applications, the use of optical tweezers in the field of biophysics has been extensive and quite impressive [8]. Ashkin and his co-workers for the first time were able to trap biological particles like tobacco mosaic virus and bacteria [9]. This opened up a wide space for experiments on biomolecules and after that a lot of biological particles like RBC, cell organelles such as cytoplasm and others were trapped using single laser beam. In addition to trapping of these biological molecules, optical tweezers were used to investigate various biophysical and biochemical processes like mechanical properties of biological polymers and various organisms which form the internal dynamics of a cell. An example of such an experiment is the study of mechanical properties of DNA, along with its interactions with proteins using the force-extension measurements as shown in Figure 1.2a, 1.2b. It unravelled many mechanical properties of DNA, which were impossible to determine experimentally at the single molecule level. Optical tweezers have also showed the distortion of RBC and confinement of large number of cells in the trap [10]. Also the elastic properties of RBC membranes and shape recovery times of single RBC have been measured [11, 12]. The collision of two particles or cells under controlled biological conditions was also done using two tweezer systems. This helped in studying of the collision of influenza virus and the erythrocytes with controlled velocities and geometry

in the presence of inhibitors and showed the adhesion between them and in the process led to the realization of potential inhibitor of the process. The optical tweezer was also used to isolate individual bacteria from a mixed sample in a chamber [13]. One of the most important functions of the optical tweezer is the study of molecular motors, which interact with microtubules or actin filament in the cell to generate mechanical forces responsible for cell motility, cell locomotion and organelles locomotion inside a cell [14]. Optical tweezers were used in colloidal science to show the existence of attractive forces between similar charged particles and formation of metastable colloidal crystals [15, 16]. The applications also include microrheology, colloidal hydrodynamics, non-equilibrium thermodynamics.

Optical tweezers have been combined with different single molecule techniques to make hybrid systems used to manipulate complex biological systems and measure multiple attributes related to it. Fluorescence of biological molecules in association with optical tweezer is one of the most powerful tool for understanding the dynamics of large number of molecules such as polymer physics of DNA [17, 18], study of molecular motors such as helicase complex RecBCD [19, 20] as shown in Figure 1.2c. An important effect of this is the ability to demarcate different parts of larger molecule and measure the response of each part individually [21]. The combination of optical tweezers with Raman spectroscopy, commonly known as Raman tweezers has also developed as a diagnostic tool for single cell analysis with applications in cancer cell analysis [22].

Modifying the trapping laser beam shapes to higher order laser beams such as the Hermite-Gaussian, Laguerre-Gaussian, Bessel and optical vortices [23] has also resulted in some exotic functions of the optical tweezer like, actuators for micromachines, which find applications for lab on a chip devices used in medical diagnostic. The well-defined orbital angular momentum of these beams and hence the ability to produce torques in addition to force makes them different from simple Gaussian beam. This characteristic of the beam makes it possible not only to trap but also rotate particles without the need of external, mechanical or electrical steering [24, 25]. Many applications based on this, not mentioned here, can be found in the extensive review papers and encyclopaedia of optical tweezers [26, 27].

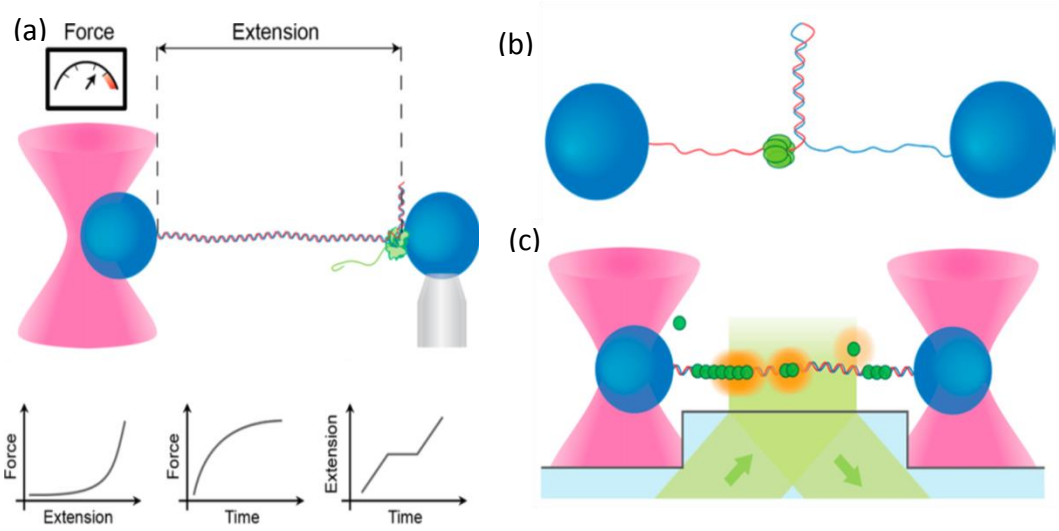

Figure 1.2 (a) Schematic of an experiment using optical tweezers for the measurement of the forces on an optically trapped sphere and the extension of the DNA-protein complex. The different curves show typical stretching curve of DNA [28], stalling of a protein filament assembly and force damping [29] and translocation and pausing by RNA polymerase [30]. (b) Unwinding of DNA hairpin by helicases using optical tweezers. (c) Optical tweezer with fluorescence microscopy of fluorescently labelled proteins for measurement of real time binding, unbinding on DNA [31, 32]. Figure reprinted with permission from Ref. [26].

1.3 Limitation of Conventional Optical Tweezers

In majority of the single molecule experiments performed using conventional optical tweezers, micron sized beads are used as handles to the biological molecules, which means that the biological molecule is biochemically linked to the bead. This is because the magnitudes of the forces are not sufficient to stably trap the biological molecule themselves. The magnitude of the gradient force scales as third power of the radius of the particle. Therefore it is difficult to use the conventional optical tweezers to trap particles in the nanoscale size regime, which includes biomolecules such as protein, DNA etc. and

structures such as quantum dots, graphene, nanotubes, and nanowires important for nanomaterial application. This can be explained as follows:

The high intensity focused laser spot in an optical tweezer creates a potential well to trap the particles. The stable trapping of the particle requires the potential depth to be sufficiently large to overcome the energy associated with the particle under Brownian motion due to the thermal energy [33]. In this case, the particle is unlikely to escape due to Brownian motion if,

$$U \gg k_B T$$

, where k_B is the Boltzmann constant, T is the temperature and U is the potential energy. The trap potential can be formulated based on the perturbative approximation, where the particle does not significantly change the surrounding electromagnetic field and can be treated as a point dipole. The electromagnetic field constituting the laser beam induces a dielectric polarization (p) in the particle, which depends on the field and the permittivity of the medium. This dipole moment p induced at the sphere by a uniform electric field E is given analytically as, [34]

$$p = 4\pi {n_m}^2 \varepsilon_o r^3 \left(\frac{m^2 - 1}{m^2 + 2}\right) E \qquad (1.1)$$

Where n_m is the refractive index of the surrounding medium, m is the relative refractive index of the particle, with $m = \frac{n_p}{n_m}$, n_p is the refractive index of the particle, r is the radius of the sphere. The overall trapping potential can be written as, [33]

$$U = -p.E = -\frac{2\pi n_m r^3}{c}\left(\frac{m^2-1}{m^2+2}\right)I \qquad (1.2)$$

The trapping potential is proportional to the third power of the radius of the particle (r^3) and the intensity $(I = \frac{1}{2}\varepsilon_o c E^2)$ at the trapping point. Hence the laser tweezer suffers from an inherent limitation when trapping particles in the Rayleigh regime. Also, the Stokes' drag force in a homogeneous liquid environment scales linearly with particle diameter, giving an additional dependence on the size. (This does not change the trapping potential, but does rescale the time unit, so stable trapping is achieved for less time). Therefore, stable trapping of Rayleigh sized particles using conventional approach requires higher power, which can have damaging effects on the particle. This is a major issue especially when dealing with biological specimens. Tethering of these small particles to larger micron sized beads is used as an alternative, which is not always favourable as it sometimes restricts the free motion of the particle while adding complexity to the process [35].

1.4 Nano-Optical Tweezers (Enhanced gradient force based plasmonic tweezers)

Nano-Optical tweezers use especially designed nanostructures for trapping small particles in the Rayleigh domain. With proper design and engineering of the nanostructures, it is

possible to overcome the diffraction limit and concentrate light into highly localized and intense fields known as hot spots. The nanostructure efficiently couples propagating field to evanescent field which unlike propagating field can be concentrated well below the diffraction limit due to plasmonic resonances. Plasmonic resonances overcome the diffraction limit because the field is induced by the resonance of electric carriers at the metal surface instead of propagating electromagnetic waves [36]. This results in increased gradient forces for small incident laser power making it possible to trap Rayleigh particles without damaging them. Among some of the earliest nanostructure proposed for using evanescent waves for optical trapping involved sharp metallic tips [37], nanoaperture in opaque metallic film [38] and channelled waveguides and probes. Most of these work involved theoretical calculation of gradient forces and proposed to trap particles down to few nanometres. However the first experimental use of nanoplasmonic structure for optical trapping was done using micrometre sized gold disk [39]. The gold disk were used to trap 4.8 μm polystyrene spheres with an incident laser intensity of 10^7 Wm^{-2} which was about two orders of magnitude less than required by conventional optical tweezer. The proposed structure was further extended for parallel trapping of yeast cells using microfluidic arrangement [40]. The simple disk nanostructure was able to trap spheres of sizes down to 1 μm but failed for sizes in the nanometre range. This is due to limited intensity and symmetry of the optical near field due to change in the nature of surface plasmons. Plasmonic antennas made it possible to extend trapping to nanometre scale. The plasmonic antenna consist of two identical metallic particles (plasmonic dimers) separated by nanoscale dielectric gap. A linearly polarized incident light along the vector connecting the particle produces a confined and

intense light spot inside the nanogap [41]. This leads to strong light matter interactions making them suitable to trap objects of nanoscale sizes. The first plasmonic antennas used for optical trapping consisted of two gold cylinders which trapped 200 nm polystyrene nanospheres with increment in the stiffness [42]. The plasmonic antennas of different configurations like nanobars, nanopillars [43] and bowtie [44] have been used as chip based nano-optical traps for optical immobilization and controlled orientation and manipulation. Multiple antennas on a chip were also used to achieve parallel trapping and demonstrated trapping of biological samples. Thus plasmonic antennas along with its high trapping efficiency provided flexibility and integration ability by formation of chip based optical traps. Some of the non plasmonic structure such as whispering-gallery-mode (WGM) optical resonator has also been used to trap 280 nm particles with low incident power [45]. Silicon waveguide also focuses light within a 100 nm gap and has been used to trap a 75 nm polystyrene sphere and DNA strands [46]. Trapping and rotation of particles was also demonstrated by using a plasmonic Archimedes spiral structure excited using a circularly polarized light [47]. Comprehensive lists of the nanostructures which have been used as optical tweezer have been summarized in Figure 1.3.

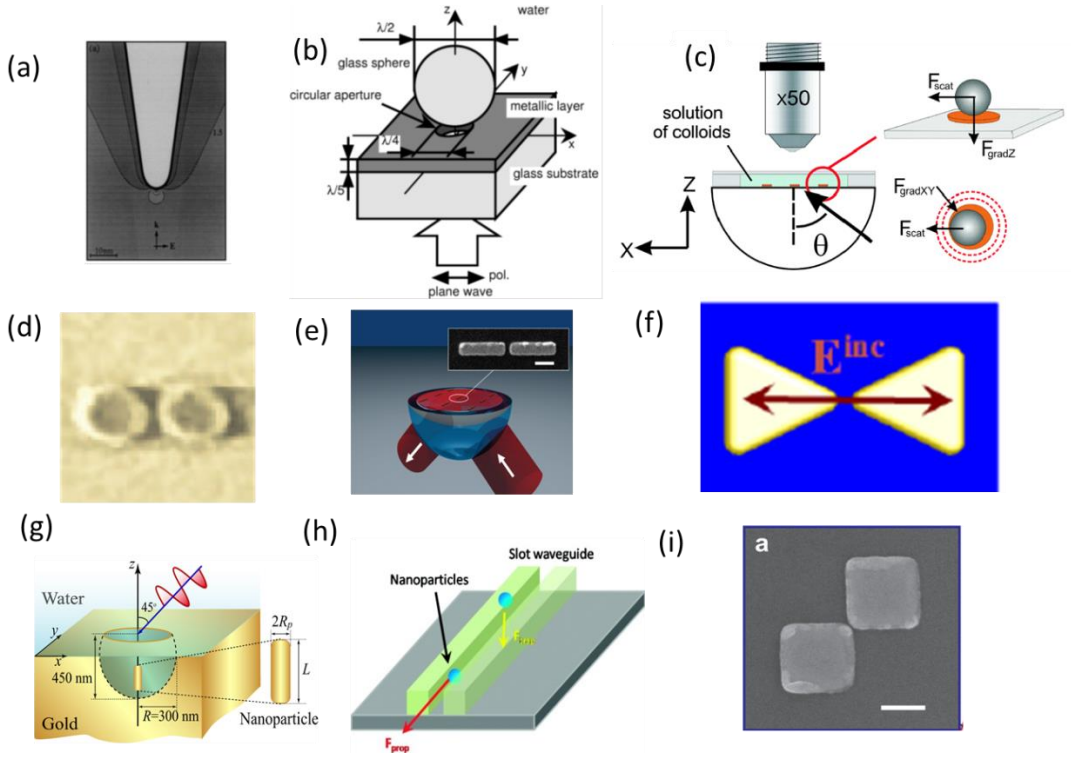

Figure 1.3 Nanostructures used for optical trapping (a) sharp metallic tip*(1997) [36] (b) nanoaperture in opaque metal film* (1999) [38] (c) gold disks# (2007) [39] (d) nanopillars #(2008) [43] (e) nanobars #(2009) (f) bowtie# (2012) [44] (g) tunable microcavities* (2008) [48] (h) slot waveguide# (2009) [11] (i) plasmonic nanoblock pair# (2013) [49] . * Theoretical, # Experimental. Figure reprinted with permission from corresponding References.

1.5 Limitations of Enhanced Gradient Force based Plasmonic Nano-optical Tweezers

Particles in the range of 1-100 nm are of primary interest in nanotechnology and optical trapping. But trapping in this range using plasmonic tweezers faces challenges. The plasmonic nanoantenna or tip configurations offer large optical field gradients; necessary for trapping of such small particles, but has large optical local field intensity within the trap of magnitude larger than 1×10^{12} Wm^{-2}. This high field intensity can result in the

damage of the trapped specimen and the nanostructure itself such as the metallic tips [50]. Also as most of the trapping operates in the liquid surrounding, the high absorption within the metal may results in heat-induced fluid dynamics resulting in convection and thermophoresis [51] or bubble formation [52] which could affect the trapping. Plasmonic nanostructures are also faced with the problem of heating and might require a heat sink integrated with the optical structure to reduce heat in the plasmonic trap [53]. These factors can largely affect the trapping of such small particles and therefore the use of plasmonic tweezer as optical trap cannot be directly scaled for this limit. The approach used in this thesis reduces the need for large local field intensities by making apertures in metal film, which provides the capability to overcome the challenges faced by plasmonic tweezers and scale the trapping approach to trap particles in the range of 1-100 nm using intensities as low as 1×10^{9} Wm^{-2}. The intensities are much smaller (nearly 1000 times as shown later) than would be required by conventional tweezers to trap particles of similar sizes and is compatible with heat sensitive biological specimen and nanoparticles used in different work during the thesis. The high laser intensities in the trap ($>1 \times 10^{10}$ Wm^{-2}) can cause optical damage to the biological molecules of interest. The photodamage can be caused by mechanism like two photon absorption, local heating or photochemical reactions creating reactive chemical species harmful for the biological molecules. For example, the polystyrene particles of 100 nm size were found to be damaged in 25 seconds using few $MWcm^{-2}$ power densities in an optical tweezer [6]. Also laser power intensity of 200 $MWcm^{-2}$ were shown to cause a temperature change of 130°C, which is beyond the denaturation temperatures of proteins [54].

1.6 Motivation and Contribution of Thesis

The research based on nano-optical tweezers has mostly been focussed on the development of novel nanostructures, with a focus to trap smaller and smaller particles efficiently. Different configurations of the nanostructure design, material, and instruments were developed to make trapping of small Rayleigh particles in the 1-100 nm range stable and efficient. But the use of these nano-optical tweezers for study and manipulation of small biomolecules and nanoparticles is lacking and not looked at. The idea to develop techniques, which can be applied to these tweezers for different applications in nanoparticle analysis and biomolecular studies, is the prime motivation behind this work. The aim is to use the aperture tweezer beyond the regular trapping by developing techniques, which can extract more information about particle dynamics, bio molecular processes for all possible applications. Therefore this thesis is an endeavor to find novel techniques which can develop into different possible applications of the nano-aperture tweezer and also open up various possibilities associated with it. The major contribution of the thesis is the development of DNH tweezer as a tool for single molecule analysis. It also makes a comparison with the conventional tweezer which is necessary for its evaluation as a tool of the future.

The outline of the thesis is as follows:

Chapter 1 gives an introduction on optical tweezers. The working principle of optical trapping and manipulation are discussed along with their applicability in different fields.

The limitations of conventional tweezers to trap with reduction in the size of the particle are discussed. Plasmonic tweezers with increased gradient forces is also presented, showing the ability to trap Rayleigh particles efficiently with small incident powers, but limited to particles in the range of hundreds of nm.

Chapter 2 discusses the aperture based traps in general using the Bethe's theory. The underlying physics of the aperture based traps is examined. The double nanohole aperture tweezer experimental set up is discussed in detail along with the fabrication of DNH and the chip assembly, which are used in general throughout the experiments done in the thesis. Some added advantages brought by the DNH tweezer in comparison to the conventional optical tweezer are also highlighted which form the basis of the study of the future chapters.

Chapter 3 shows an optical trapping experiment to quantify the trapping efficiency and stiffness of the DNH optical trap. The techniques based on the autocorrelation of the Brownian-induced intensity fluctuations and the trapping transient are used to calculate the stiffness of the aperture trap. A comparison of the trap stiffness is made with other nano-optical tweezers and conventional optical tweezers.

Chapter 4 shows the capability of the DNH tweezer to be used as a sensor. The statistical analysis of the time-to-trap parameter during the trapping experiment is used to determine the concentration and size of the nanoparticle of the trapping solution. Also the transient

change in transmission signal at trapping instant is used to determine the refractive index of the particles.

Chapter 5 studies the dynamics of hairpin DNA and its interactions with transcription protein p53. The DNH tweezer is used to show the unzipping of the hairpin DNA molecule. The interaction of the hairpin DNA with both the normal and mutant form of p53 is studied. The unzipping time is used to quantify the energy related to the interaction between the wild-type and the DNA molecule. The experiment presents the DNH tweezer as a label-free and solution-free single molecule probe from biomolecular studies.

Chapter 6 discusses the extraordinary acoustic Raman (EAR) technique using the DNH optical tweezer and its application for studying the vibrational dynamics of the ssDNA molecule in the GHz range. A modified DNH optical tweezer setup to excite and detect the resonant vibrational modes is shown. The dependence of the resonant vibrational modes on the length and the sequence of ssDNA molecule are also discussed. It opens up avenues for studying the biomolecules in real time and at single molecule level in terms of the vibrational dynamics for a wide range of frequencies and high resolution.

Chapter 7 concludes the dissertation along with some possible future research directions.

Appendix A shows the alternative approach of template stripping used for the fabrication of the DNH on gold.

Appendix B shows the procedure for making the microfluidic chip which has been used in the experiment described in chapter 4 of the thesis and can be used in some future applications.

Publications:

1. **A. Kotnala**, D. DePaoli, R. Gordon, "Sensing Nanoparticles Using a Double Nanohole Optical Trap," *Lab Chip* , 13, 4142-4146 (2013).
2. **A. Kotnala**, R. Gordon, "Quantification of High-Efficiency Trapping of Nanoparticles in a Double Nanohole Optical Tweezer," *Nano Letters,* 14 (2), 853-856 (2014).
3. **A. Kotnala**, R. Gordon, "Double nanohole optical tweezers visualize protein p53 suppressing unzipping of single DNA-hairpins," *Biomedical Optics Express,* 5(6), 1886-1894 (2014).
4. **A. Kotnala**, S. Wheaton, R. Gordon, "Playing the notes of DNA with light: extremely high frequency nanomechanical oscillations," *Nanoscale,* 7, 2295-2300 (2015).
5. **A. Kotnala** and R. Gordon, "Laser Tweezers Using Nanoapertures in Metal Films," Encyclopedia of Nanotechnology, *Springer Netherlands*, 1-12 (2015).
6. Al Balushi, **A. Kotnala**, S. Wheaton, R. M. Gelfand, Y. Rajashekara, R. Gordon, "Label-free free-solution nanoaperture optical tweezers for single molecule protein studies," *Analyst,*140, 4760 - 4778 (2015) (Invited Paper)

7. Y. Chen, **A. Kotnala**, L. Yu, J. Zhang, and R. Gordon, “Wedge and conventional plasmonic resonances in double nanoholes. (Submitted).
8. **A. Kotnala**, A. Al-Balushi, R. Gordon. “Optical tweezers for free-solution label-free single bio-molecule studies”. Proc. SPIE 9164, Optical Trapping and Optical Micromanipulation XI, 916418 (September 16, 2014); doi:10.1117/12.2062051.
9. **A. Kotnala** and R. Gordon, "Mapping low frequency vibrational spectra of ssDNA using DNH optical trap," in *Optics in the Life Sciences*, OSA Technical Digest (online) (Optical Society of America, 2015), paper OtT2E2**.**
10. R. Gordon, A. Al-Balushi, **A. Kotnala**, R.F. Gelfand, S. Wheaton, S. Chen, S. Jin, “New physics and applications of apertures in thin metal films”. Proc. SPIE 9172, Nanostructured Thin Films VII, 91720A (August 27, 2014); doi:10.1117/12.2062919.
11. S. Wheaton, **A. Kotnala**, A. Al-Balushi, R.M. Gelfand, A. Zehtabi-Oskuie, Y. Rajashekara, R. Gordon. “Trapping, unfolding, identifying, and binding single proteins using the double-nanohole optical trap”. Proc. SPIE 9126, Nanophotonics V, 91260O (May 2, 2014); doi:10.1117/12.2049045.

Chapter 2. Nanoaperture Tweezers

2.1 Introduction

This chapter explains the general principle, design, fabrication and experimental set-up of aperture tweezers, in particular the DNH aperture tweezer, which forms the basis for trapping of nanoparticles and biomolecules in different experiments in this thesis. Nanoaperture refers to an aperture in a metal film of size much smaller than the wavelength of light. The nanoapertures are used for optical trapping and manipulation of Rayleigh particles; that is particles that are significantly smaller than the wavelength of light, typically in the 1-100 nm range. Bethe's aperture theory of the optical transmission through a subwavelength aperture is discussed and used to explain the trapping phenomenon in subwavelength apertures. The self-induced back action (SIBA) effect associated with the aperture based trap is also illustrated. The double nanohole (DNH) aperture tweezer experimental set up is described in detail along with the chip assembly. Some of the important characteristics of the DNH tweezer in comparison to the conventional optical tweezers are also mentioned.

2.2 Stable Trapping of Rayleigh Particles

Rayleigh particles have always been challenging to trap directly by conventional optical tweezer due to the requirement of very high incident laser power intensity, which results in damaging the particle [6]. This problem was solved by nanostructure based optical

tweezers, such as the plasmonic optical tweezers which showed the trapping of Rayleigh particles in the range of few hundreds of nm as mentioned in Section 1.4. Nanostructures concentrate light into highly localized and intense fields below the diffraction limit. This result in the increased gradient forces with smaller incident laser power, and therefore makes trapping of Rayleigh particles possible. The increased gradient forces are a necessary but not sufficient condition for stable trapping of the particle [6].The average kinetic energy of the particle in the trap is k_BT but the instantaneous velocity follows a Maxwell–Boltzmann distribution [55] and therefore the energy of the particle occasionally exceeds the average kinetic energy. To account for these high energy events the potential depth of at least 10 k_BT is recommended for trapping small Rayleigh particles [6].

For particles sizes of less than 100 nm, the plasmonic nanostructures fail to fulfil the potential energy requirement to compensate for high energy events and result in unstable trapping. Since the potential energy is a function of the electric field intensity at the trapping point, it can only be increased by increasing the incident laser power. Even though high intensities might not damage the trapped specimen, the thermal effects arising from high intensities might play a dominant role in particle dynamics and dominate over the optical forces. In both the conventional optical tweezer and plasmonic based optical tweezer, the potential well of the optical trap is static and does not change during the experiment and is usually optimized for a given particle and does not account for the stochastic Brownian motion of the particles. A dynamic trap in which the potential

well is dynamically configured to account for the high energy events is a suitable approach to bring down the average potential depth required to stably trap the particles. The approach requires the use of an external feedback system which is applied to the conventional optical tweezer to correct the trapping potential by changing the trap position [56] or laser intensity [57].This makes the optical tweezer system complex and sometimes unstable.

A possible solution to the problem is using the dynamic feedback from the particle in the trap to optimize the trapping potential to account for the high energy events and provide the desired potential energy for stable trapping of small Rayleigh particles. Keeping this in mind, nanoapertures not only provide the strong gradient force necessary for optical trapping but also provide a solution to work beyond the perturbative regime where the particle itself plays a major role in trapping. In this case, a small particle can induce a significant change to the electromagnetic field, and play a positive role in the trapping process known as self-induced back action (SIBA) trapping. The presence of the particle in the aperture increases the local electromagnetic field intensity, which increases the potential well depth required for stable trapping, without the need of increased laser power. Figure 2.1 shows the comparison of the trapping potential energy for the conventional tweezer, gradient based nano-optical tweezer and the SIBA based aperture traps respectively.

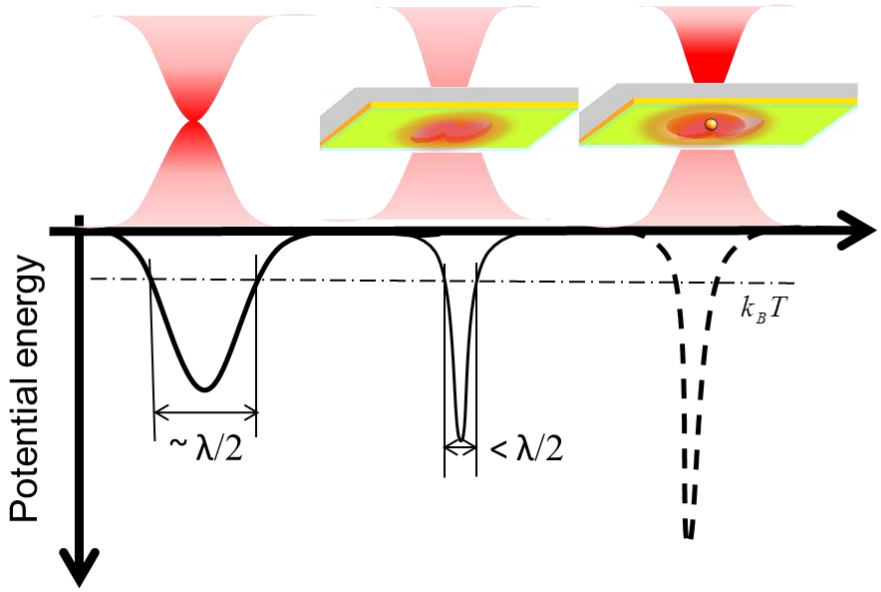

Figure 2.1 Schematic illustration of conventional tweezer, nano-optical tweezer and aperture tweezer showing the SIBA effect along with their corresponding potential energy profile. Conventional tweezers trap nanoparticles at the focal point of the laser beam and form a Gaussian trapping potential well with trapping space of nearly equal to the diffraction limit of light. The plasmonic tweezer trap particle in the confined active nanospace which in the present case is the area between the cusps of the DNH. The potential energy profile depends on the shape of the structure and is much smaller than the diffraction limit of light. The SIBA based trap provide a dynamic potential energy change by the presence of the particle in the active area by increasing the potential depth as the particle tries to escape from the active trapping area.

2.3 Bethe's Theory

Nanoaperture refers to an aperture in a metal film of size much smaller than the wavelength of light. The small dimension of the aperture compared to the wavelength of light cuts off the propagation of light. This is due to the inability of the propagating wave to satisfy the boundary conditions. Thus the light is diffracted at the edges of the subwavelength aperture. Hans Bethe first studied the transmission of light through a

subwavelength hole in a metal screen, where the light transmitted through the circular aperture is approximated by the emission of magnetic dipole [58]. The transmission through such an aperture is approximated as,

$$T = \frac{1}{2}\left(\frac{4Z_o\pi^3}{3{\lambda_o}^4}\right)\left(\frac{8r^3}{3}H_o\right)^2 \propto \frac{r^6}{\lambda^4} \qquad (2.1)$$

where Z_o is the free-space impedance, $\lambda_o$is the wavelength in free-space, r is the hole radius, and H_o is the magnetic field of the incident wave. Normalizing with respect to the area of the circular aperture, according to Bethe's theory the transmittance through a subwavelength circular aperture is inversely proportional to fourth power of the wavelength $T \propto \frac{r^4}{\lambda^4}$ as shown in Figure 2.2. If the aperture is surrounded by a dielectric medium with a refractive index n, the wavelength in the medium is scaled as $\lambda = \frac{\lambda_o}{n}$. Therefore, a larger optical transmission is expected for the same aperture size as shown in Figure 2.2b:

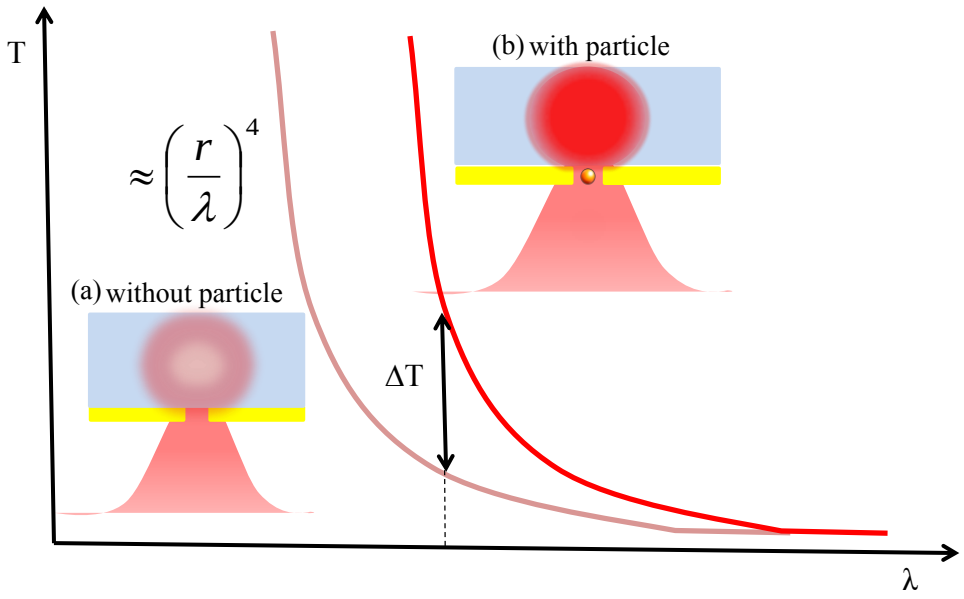

Figure 2.2 Optical transmission through a single subwavelength hole: (a) without particle; (b) transmission enhanced with a dielectric particle in the hole (dielectric loading). The presence of the dielectric particle makes the hole optically larger through dielectric loading, red-shifting the transmission curve and giving the change ΔT in transmission.

Here we consider metal films of finite thickness in real conductors that can have plasmonic effects. Nevertheless, it has been demonstrated that the transmission through the aperture in finite conductivity films drops off past the cut-off wavelength in a way that resembles the scaling of Bethe's theory [58]. Since the optical transmission through a subwavelength aperture is very sensitive to the aperture size (scales with the fourth power of the size), any change, including a dielectric loading by a particle effectively makes the hole "appear" larger to light (the wavelength of light shrinks in inversely with increase in the refractive index), inside the aperture. This gives a significant change to the optical transmission. The trapping phenomenon is monitored by this increase in transmission signal due to the local increment of the refractive index induced by the presence of the particle in the aperture. Thus the nanoaperture shows the characteristics of working

beyond the perturbative regime by having a strong scaling with the local dielectric environment and therefore is used as a tweezer for small particles in the range of few nanometres.

2.4 Nanoaperture Tweezers: Principle, Design and Detection

2.4.1 Principle: Self-Induced Back Action (SIBA) Trapping

The idea is to exploit the particle-nanostructure interaction, in order to achieve an automatic feedback control, which does not require external monitoring or correction system. This requires the optimization of the trapping efficiency by suitable engineering of the nanostructure such that the local intensity within the trap is maximized in the presence of the particle. As a result, the momentum of the photons interacting with the particle experiences significant changes as the trapped particle moves in and out of the trap. Due to momentum conservation, these changes create an additional dynamical force field that is by definition automatically synchronized with the object's dynamics. The force automatically increases the potential well depth during high energy events to maintain the particle in the equilibrium position. The approach is quite different from the existing previous techniques using the external feedback mechanism [59-61].

The nanoaperture trap works on the principle of self-induced back action, where the presence of the particle in the trap significantly alters the electromagnetic environment (i.e., light transmission) to favour trapping. The trapped particle provides a dynamic feedback by increasing the magnitude of the trapping potential in order to compensate the

high energy events associated with the trapped particle, which results in stable trapping [62]. It is based on the high sensitivity of the nanoaperture to the local environment as shown by Bethe's aperture theory. The presence of a small particle in the aperture significantly increases the electric field intensity which gives a decreased potential energy (increased magnitude) and thus provides a deeper potential well. The deep potential results in strong and efficient trapping of the nanoparticle using much less optical power. Thus the nanoaperture tweezer provides an inherent feedback mechanism with simple geometry without requiring any outside feedback mechanism [62].

An early work noted increased optical forces inside an aperture in a metal film but it was limited to particles, much greater than 100 nm [38]. The force calculation for nanoaperture traps using perturbative optical force formulation does not provide a good approximation. This is because the dielectric particle produces a strong change to the ambient field. The rigorous Maxwell stress Tensor (MST) analysis is therefore used to calculate forces produced by the nanoaperture tweezers. This has been done for a subwavelength circular aperture which shows much larger optical forces than calculated using the perturbative approach as shown in Figure 2.3 [62]. SIBA being a more general phenomenon can be implemented with different nanoaperture designs [6, 8-11] and photonic crystals [63]. These geometries have made it possible to trap objects in the range of few nanometres using very small laser powers.

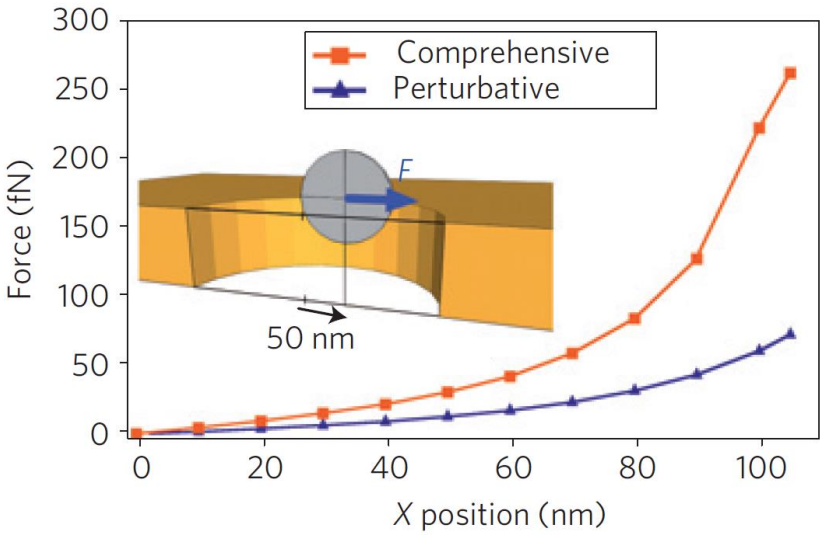

Figure 2.3 The numerically computed optical force in the circular nanohole optical trap based on FDTD simulations, while trapping 100 nm polystyrene spheres. Two physical formulations are compared: the comprehensive MST analysis and the perturbative gradient force approximation. It is found that the perturbative gradient force approximation is no longer a good approximation for computing optical forces in a circular aperture trap, and the MST analysis predicts a much larger optical force than the gradient approximation does [62]. Figure reprinted with permission from Ref. [62].

2.4.2 Design

Several nanoaperture structures have been designed with the idea of trapping smaller and smaller particles. Some of the geometries such as circular aperture [62], rectangular aperture [64], double nanohole aperture [65], bowtie aperture [66] and coaxial aperture [67] are shown in Figure 2.4. Some of these nanoapertures have shown the ability to trap particles down to size 20 nm or greater, but our design of DNH structure has shown the ability to trap particles down to the size of 1 nm including the trapping of single proteins

[68], DNA strands of few base pair (bp) [65], quantum dots [69] and so on. The coaxial nanoaperture also provides forces enough to trap particles of size about 2 nm but has been predicted only theoretically, without any experimental demonstration of trapping so far. A comparison of the DNH structure with other designs will be presented in the next Chapter. Also the planar and small size of nanoaperture makes them suitable candidates for dense optical integration and use in planar microfluidic environment. It also makes it possible to integrate it with other optical techniques like fluorescence microscopy and Raman spectroscopy.

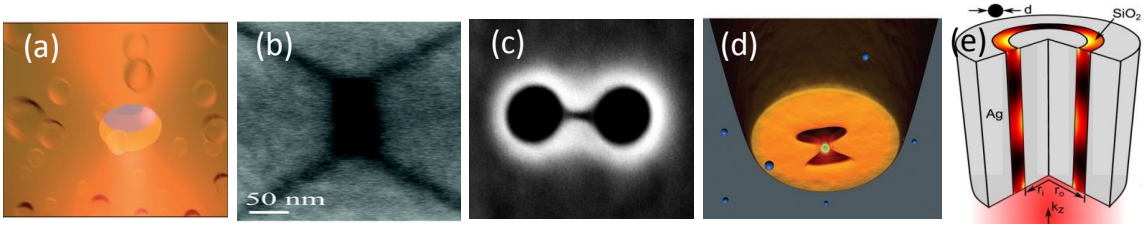

Figure 2.4 Nanoaperture designs (a) Circular aperture [61] (b) Rectangular plasmonic nanocavity [64] (c) Double nanohole aperture [65] (d) Bowtie nanoaperture (BNA) at the fiber tip [66] (e) Coaxial nanoaperture [67]. Figures reprinted with permission from corresponding References.

2.4.3 Detection

The detection of the trapped particle in the aperture is usually based on the change in the transmission signal through the nanoaperture. The normal optical transmission through a nanoaperture is mainly through diffraction and low but when a particle of size smaller than the aperture and larger refractive index than the surrounding medium is trapped, the aperture becomes optically larger than the physical size due to dielectric loading. This

leads to an increase in transmission indicative of the particle being trapped in the nanoaperture [62]. An example of trapping based on the detection of change in transmission through a DNH aperture will be shown in the next chapter. The trapping of single particle using a bowtie nanoaperture (BNA) has also been confirmed using 20 nm fluorescent polystyrene particles by observing an increase in fluorescence signal in addition to the increased transmission signal as shown in Figure 2.5 [66].

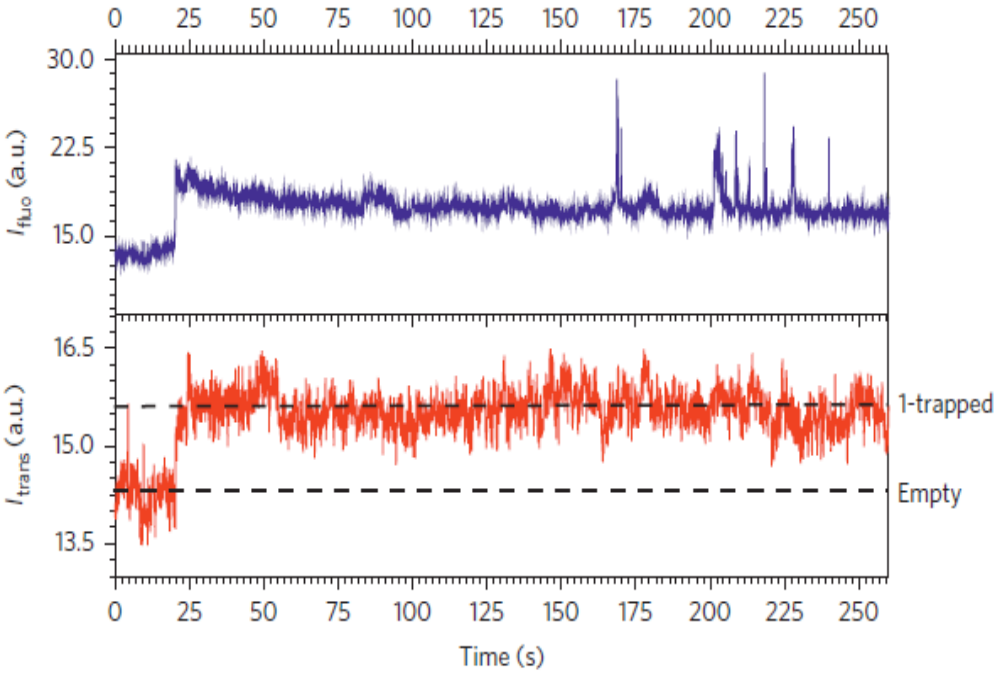

Figure 2.5 The fluorescence and transmission signal through the bowtie nanoaperture (BNA) as a function of time. The step change in the fluorescence signal (blue) and the transmission signal (red) at around t=23 sec corresponds to the trapping of the single 20 nm polystyrene nanosphere in the BNA. Figure reprinted with permission from Ref. [66].

2.5 DNH Optical Tweezer Experimental Set-up

The general DNH tweezer system used in most of the experiments in the thesis is a modified Thorlabs optical tweezer kit (OTKB) based on a simple inverted microscope configuration as shown in Figure 2.6. The quadrant photo detector (QPD) of the original tweezer kit is replaced by a silicon-based avalanche photodiode with bandwidth of 50 MHz (Thorlabs APD110A) for the detection of the transmitted signal. A trapping beam laser of 820 nm (SacherLasertechnik Group, Model TEC 120) is collimated, beam expanded and focussed using a 100× oil immersion microscope objective (Numerical aperture NA=1.25) to the DNH having a laser spot of 1.1 μm. The 820 nm laser wavelength provides high detection efficiency for the APD. The 820 nm wavelength also has a lower absorption in water. An optical density filter (OD1) is used to limit the power of the laser to few mW at the output of the objective. The optical transmission through the DNH is collected using a 10× condenser microscope objective (NA 0.25) and measured using the silicon based APD. The chip containing the double nanohole structure (DNH) is mounted between the oil immersion microscope objective and condenser objective on a piezoelectric controlled xyz sample stage as shown in Figure 2.6. The laser spot is aligned to the double nanohole using the xyz controls having a precision of 20 nm. It may be noted that a half wave plate is also used to align the polarization of the trapping beam along the axis of the cusps of the double nanohole (along x axis for the present case). The polarization alignment provides large local field enhancement between the tips creating a large trapping potential for trapping. The output of the APD is recorded using a data acquisition card (DAQ) (Measurement Computing (MCC) High Speed DAQ Board). The rate of acquisition is selected depending on the

specific requirements of the experiment and noise considerations. The DNH system provides the ability to acquire data up to a rate of 1 MHz. The lower limit of the temporal resolution is based on the relaxation time of the DNH tweezer system. This is dependent on the size of the trapped molecule and the stiffness of the trap. For the DNH tweezer used to trap Rayleigh particles, it is in order of few milliseconds as will be discussed in the next chapter. The upper limit of the data acquisition is limited by the time scales of the processes associated with the trapped molecule. In the present setup, the sampling rate of the trapping signal recorded by the DNH tweezer is limited by the maximum acquisition rate of the DAQ card. The sampled transmission signal is ultimately limited by the temporal response of the photodetector and the electronic circuitry. APD has a bandwidth of 50 MHz and therefore does not limit the temporal resolution for the timescales involved in all the experiments performed in the thesis.

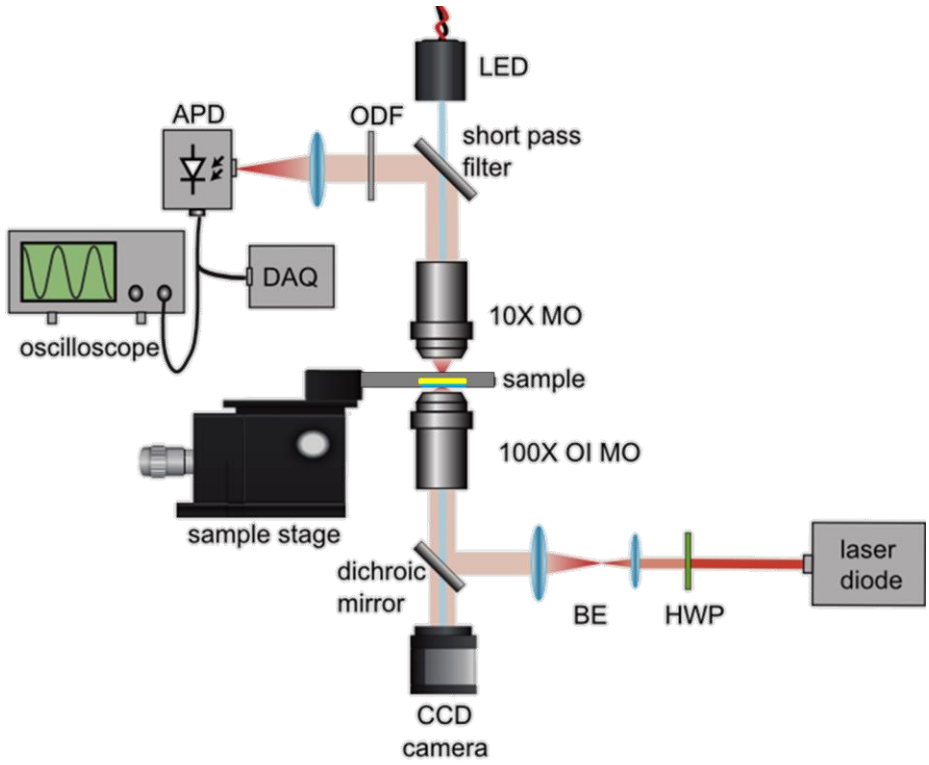

Figure 2.6 Schematic of optical trapping experiment. Abbreviations used: ODF: optical density filter; HWP: half wave plate; BE: beam expander; MR: mirror; OIMO: oil immersion microscope objective; APD: avalanche photodiode; DAQ: data acquisition card.

2.6 Fabrication of DNH

The DNH apertures used in all the experiments were fabricated using Hitachi FB-2100 Focused Ion Beam system. The DNH are fabricated on commercially available gold test slides (EMF Corp.) with a 5 nm Ti adhesion layer followed by 100 nm gold layer on a glass substrate. A focused gallium (Ga) ion beam with an acceleration voltage of 40kV and beam current of 0.003-0.01 nA was used to mill the gold to form the required DNH apertures. These beam parameters provide the requirements for fabrication of very small features with great precision.

The other fabrication parameters such as dwell time, number of passes and magnification can be optimized to get the desired aperture dimension. It may be noted that the small gap with sharp cusps especially of sizes of few nm requires good beam alignment and optimized milling parameter.The DNH's were fabricated at a magnification of 70K or 80K. The milling time (dwell time × number of passes) can be optimized to get the desired DNH structure. The dwell time mostly used in the present DNH fabrication ranges from 1-5 μs and the number of passes, N = 30-40. Figure 2.7 shows the impact of the milling time on the DNH structure.

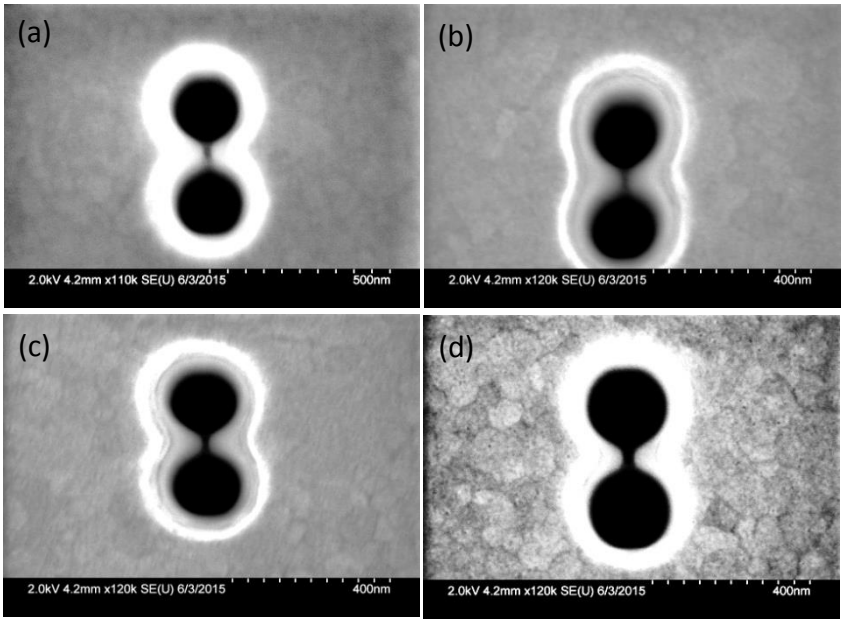

Figure 2.7 Scanning electron microscope (SEM) images of DNH showing the impact of the milling time (milling time=dwell time × number of passes) on the DNH structure. The dwell time was fixed to 5μs and the numbers of passes were varied. (a) 20 pass (b) 30 pass (c) 40 pass (d) 50 pass. The gap is not milled completely for less than 40 passes, while increasing above 40 passes might increase the cusps gap width beyond the desired size.

The dwell time was kept constant to 5µs, while the numbers of passes were varied from 20 to 50. For number of passes less than 40, the gold in the nanometric gap between the cusps is not completely removed as shown in Figure 2.7a & b. We need to optimize the number of passes such that it removes all the gold in the gap. Also increasing the number of passes would rather increase the gap width more than that required for the trapping experiment as shown in Figure 2.7d. A number of passes of approximately 40 gives us the smallest possible gap between the cusps which is nearly 28 nm, as shown in Figure 2.7c.

The diameter of the circular apertures forming the DNH structure lies in the range of 160-180 nm. Figure 2.8a & b shows the bitmap image and the SEM image of a typical DNH structure. It consists of two circles separated by a distance. The spacing between the circles can be adjusted to get the desired spacing between the cusps of the DNH which plays a crucial role in getting a good trapping efficiency and detection. In an ideal case the spacing between the cusps should be slightly larger than the size of the desired trapping specimen for good trapping efficiency as will be demonstrated experimentally in the later chapters. The small gaps create strongly confined nanoscopic volume of strong electric field intensity for trapping of the desired nanoparticle or biomolecule. A ring is also milled encircling the nanohole as a marker large enough to see in the DNH tweezer system which helps in the alignment of the laser on the DNH during the trapping experiment as shown in Figure 2.8c. The size of the rings (diameter = 50 µm) is much larger than the wavelength of the incident laser beam and therefore has no effect on the DNH aperture at the centre due to plasmon coupling or scattering effects.

An alternative approach of template stripping [70] was also used for fabrication of DNH. This method makes the fabrication of DNH cheap with high throughput as compared to the FIB. A detailed discussion on this is presented in the appendix A.

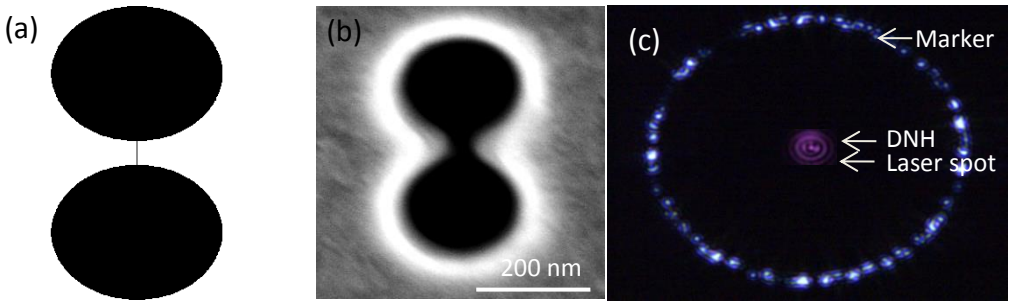

Figure 2.8 (a) Bitmap image used to make DNH using FIB. (b) Typical SEM image of the DNH. (c) CCD image of the DNH encircled by ring used as marker on the gold sample. The red spot at the center shows the laser spot focused on the DNH.

2.7 Chip Assembly

The chip used in the DNH tweezer system is constituted of the DNH on gold, imaging spacers, rectangular glass cover slip and the colloidal solution of the particles to be trapped. Figure 2.9a shows the 3-D perspective view of the chip used for trapping of the nanoparticles. The imaging spacer (Secure Seal imaging spacer, Grace Bio-labs) has a thickness of 90-100 μm with a small circular hole of 9 mm diameter. The imaging spacer is attached to a glass coverslip (Ted Pella, Inc.) of thickness about 100-120 μm to form a well. The well is subsequently filled with the solution containing the particles to be trapped. The gold sample is than put on the double sided tape with gold surface in contact

with the solution so that the double nanoholes can come in contact with the nanoparticles to be trapped. Figure 2.9b shows the schematic of the front view of the trapping chip placed between the microscope and the condenser objective lenses. The chip is placed on the piezoelectric controlled xyz sample stage with the gold side facing downward so that the small contribution from gravity pulls the nanospheres away from the Au film, and the optical force works against gravity. Immersion oil with refractive index of 1.51 was used in between the oil immersion objective and the coverslip.

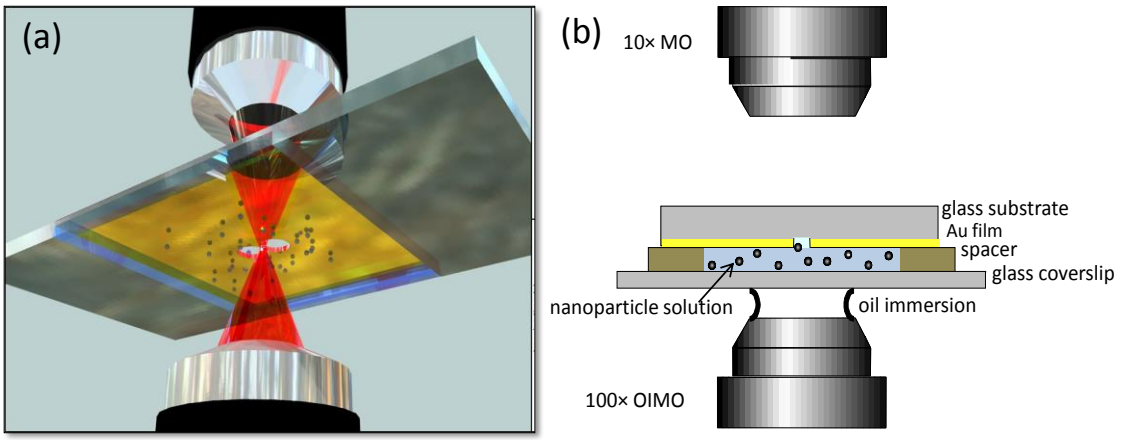

Figure 2.9 (a) 3-D perspective of the chip containing the nanoparticles. It shows the gold sample with DNH and the chamber with nanoparticles suspended in water. (b) Front view schematic of the chip placed between the oil immersion objective and the condenser lens.

2.8 Characteristics of Nanoaperture Tweezers

The DNH structure has high transmission and large collection efficiency along with strong local mode confinement which makes it a good candidate for SIBA trapping.The nanoaperture tweezers provide some additional features compared to the regular laser

tweezers, which makes it an important tool for detection, sensing and studying of very small nanoparticles and biological molecules.

2.8.1 Single Molecule Trapping

Many approaches used in the study of nanoparticles and biomolecules such as proteins, DNA etc. look at ensembles, which lead to many issues. For example, the real time dynamics are obscured without synchronization and it is not possible to measure distinct features of a heterogeneous sample. Also, kinetics is studied away from equilibrium (approaching equilibrium) in the ensemble case, whereas with single molecule sensitivity, on-off kinetics can be observed even at equilibrium. The DNH aperture trap works at the single molecule level where the real-time dynamics and heterogeneity can be observed, and kinetics can be established close to (or even at) equilibrium. It does not require synchronized operation as the observation are made on single molecule, avoiding the population average of the transient phenomenon. The small mode volume allows the trapping of only a single molecule at any instant of time. The probability of occurrence of trapping of more than one particle at certain instant of time is substantially low. The trapping events showing trapping of multiple molecules can be recognized by doing some statistical analysis on the transmission signal. An example of such an event is shown in the Figure 2.10. It shows an extra increase in transmission change after some time and also changed dynamics of the intensity fluctuation of the transmission signal. This is a rare event and therefore can be discarded. Additionally, the shape of the nanostructure also provides physical hindrance for the entry of other molecules. Thus the DNH tweezer provides single molecule trapping and allows the interaction to be monitored in real time.

However the correct interpretation of data at single molecule level, require enough statistics, which can sometimes be time consuming. For example, the single molecule confocal fluorescence measurement, used for studying protein conformational dynamics. It uses a laser point source to illuminate the diffraction limited volume of the single molecule, which is then imaged on a single photon counting APD. This enables detection of single photon arrival times including measurement of single molecule fluorescence lifetimes, which contain the information for each event and enables advanced statistical treatment of the data. Since the data is collected by only one molecule at a time, collection of complete data set can take days. This is because most of the trajectories are discarded during analysis. This is due to the experimental issues like presence of multiple molecules in the illumination volume, or due to protein's that do not contain active FRET (fluorescence resonance energy transfer) donor and acceptor pair. Also trajectories containing significant blinking or other uncorrelated changes in intensity are also removed. Large data sets also help to reduce the inherent noise and stochasticity associated with single molecule events.

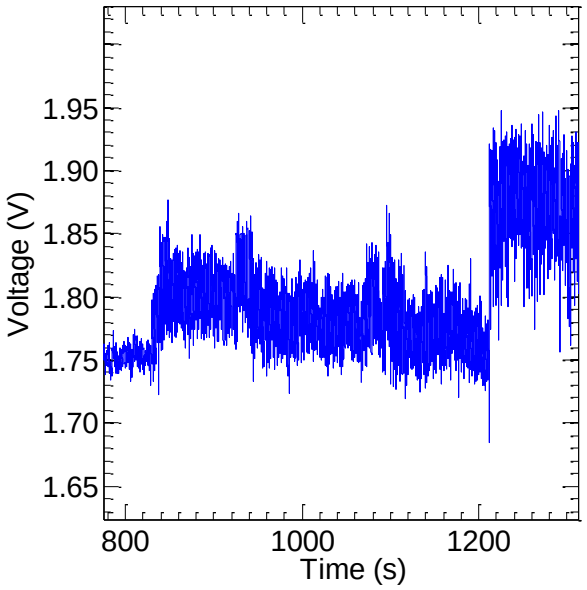

Figure 2.10 Optical trapping event showing trapping of more than one particle at the DNH trap site after some interval of time. This is random and a rare event as has been seen throughout the work and can be discarded while doing statistical analysis of the data.

2.8.2 Free-solution and Label-free

The study of biological molecules and nanoparticles in the 1-100 nm range using conventional tweezers requires tethering i.e. attaching the molecule of interest to a micron sized sphere or a micropipette. This tethering requires a tether (e.g., a functional group) that modifies the intrinsic state of the molecule. It also prevents free motion and can hinder some binding sites if they are near the tether/surface [26]. Our approach uses light to directly and efficiently hold onto the biomolecules and nanoparticles, but otherwise it is free to rotate, translate, unfold, and bind etc. as if free in solution. This allows the particle to have uninhibited natural motion in a given biological environment.

Many past works also use fluorescence or other markers to label their proteins and/or DNA for studying the dynamics of the specimen. For example, the fluorescence microscopy was combined with dual- trap optical tweezer to visualize a single λ DNA molecule and study the mechanically induced transitions of a DNA hairpin in the presence of a single Cy3- labeled oligonucleotide. The changes in the fluorescence signal due to binding and unbinding of the oligonucleotide were directly correlated with the pauses in the extension hopping of the hairpin DNA [31, 32]. This is costly, complex and it modifies the intrinsic properties of the molecule of interest. Due to the high sensitivity of the transmission signal to the physical attributes and motion of the trapped specimen in the trap, it makes it effective to detect trapping and interaction dynamics, without the need of fluorescent labelling.This approach uses the intrinsic light scattering of the biomolecules to measure the interaction, so it is label-free and does not require any resonances that can change behavior, heat the molecule, or suffer from photobleaching. Thus nanoaperture tweezers provide a label-free study of the dynamics of the trapped particle.

2.8.3 Temperature

The nanoaperture in gold metal film efficiently removes heat due to the high conductivity of the gold layer. The metal film acts as a heat sink which is crucial to prevent damage of biological particles due to heat. The laser power intensity used in all the work is of the order of 1×10^{9} Wm^{-2} .The laser intensity is quite small to cause any damage to the nanoparticles and biomolecules of interest. This has also been shown by experiments which show very small rise in temperature for an aperture in metal films,

several orders of magnitude smaller than metal nanoparticles [71]. Figure 2.11 shows the temperature distribution of a crescent shaped nanoaperture made in aluminum layer of thickness 200 nm. The temperature distribution corresponds to the state of thermodynamic equilibrium of nanostructures with an incident laser beam of radiation intensity 5×10^{15} Wm^{-2}. It can be seen from the figure that temperature of the SHR nanostructure is very close to room temperature (~ 300 K), with almost a 0.1 K increase in temperature due to the incident laser intensity. For a nanorod of size 50 nm × 570 nm, the temperature increases to 1100 K for similar incident laser intensity. A point to be noted is that the laser intensity used in this case is about 10^6 times of that used in our work. Also using plasmonic nanoparticles like gold in liquid show a 10 degree rise in temperature, when excited by a focused laser beam of 1mW at the plasmonic wavelength [72]. Thus we find that the DNH aperture provides an inherent heat sink capability which is usually externally required in case of plasmonic tweezers. [54].

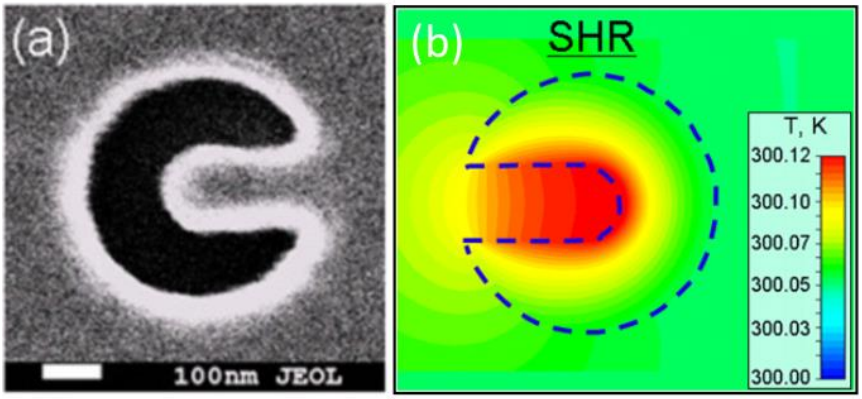

Figure 2.11 (a) SEM image of the split hole resonator (SHR) nanoaperture (b) Temperature distribution on the surface of the SHR nanostructure not exceeding 300 K, much below the destruction threshold of the metal [71]. Figure reprinted with permission from Ref. [71]

2.8.4 High SNR

The DNH nanoaperture tweezers provides a high signal-to-noise ratio due to the background free operation from the aperture. The scattering from other particles and sources do not become a part of the background signal reducing the noise in the detection signal.

2.8.5 Easy to Integrate

The DNH structure can be easily integrated into existing laser tweezer microscopy systems, tip of the fiber, and microfluidic environment. This gives it the extra flexibility to develop into a full-fledged tool for wide range of applications.

2.8.6 Other

An important aspect for practical applications (but often overlooked at the research level) is the scalability and cost of a technology. The DNH aperture tweezer is low-cost, scalable, straight-forward, high-speed real time system. It may be scaled up to well-plate format with either serial or parallel detection. Others have already demonstrated that laser tweezers can be formed in massively parallel arrays with powers far exceeding what we require. The DNH optical tweezer can be implemented by using an optical fiber approach. This is done by fabricating the DNH at the tip of a cleaved fiber. Some initial work has been done in this regard and mentioned in the future work section of Chapter 7 of the thesis. The optical fiber DNH tweezer can therefore provide the route for scaling the DNH tweezer for parallel detection, where multiple fibers can be used on a single platform at the same time. Our approach is also low cost – not only in the instrumentation

and the biochip, but also because it doesn't use fluorescence (which typically requires several filter sets, isolated lasers and photon counting capability etc.).

Chapter 3. Quantification of DNH Stiffness

3.1 Introduction[1]

An optical trap applies a restoring force on the trapped particle as the particle tries to move away or escape from the trap center or the equilibrium position. A force constant or trap stiffness (κ) is defined to describe this force field, analogous to the spring constant of a Hookean spring as shown in Figure 3.1. Therefore, the force constant or trap stiffness (κ) of an optical tweezer is defined as,

$$F = -\kappa x \qquad (3.1)$$

The values of κ depend on many parameters, e.g., the particle size, shape, refractive index, DNH geometry, laser power etc. In practice, however, the trap stiffness is conveniently adjusted by changing the laser power which can be tuned for an experiment. Therefore the trap stiffness is often calibrated against the laser power.

[1] The following chapter is adapted from: **Quantification of High Efficiency Trapping of Nanoparticles in a Double Nanohole Optical Tweezer**. Abhay Kotnala and Reuven Gordon. Accepted for publication by the Nano Letters in 2014. Copyright Permission Accepted.

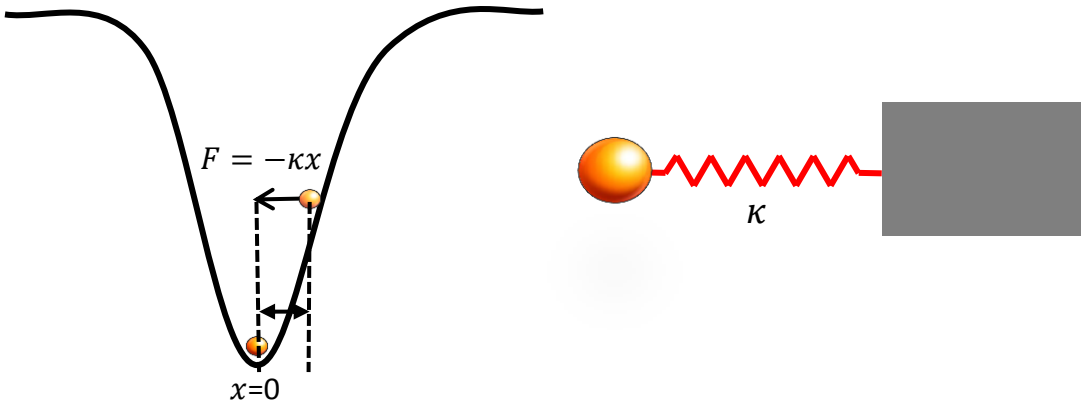

Figure 3.1 Restoring force acting on the particle, when the particle is displaced by x from the center of the potential well at $x = \mathbf{0}$. Analogous illustration showing the particle connected to a stationary block by a Hookean spring. When the particle is displaced from the center position, a restoring force acts on the particle which is defined in terms of the spring constant κ of the spring.

The double nanohole tweezers have previously trapped Rayleigh particles of sizes in the range of few nm stably and for long durations. This shows high trap efficiency of the DNH trap as compared to conventional optical tweezers for small Rayleigh particles. Therefore, it is important to quantify the stiffness of the DNH tweezer used mostly in the thesis. The experimental techniques to determine the stiffness of the aperture based traps, used to trap nanometer sized particles is also lacking in the literature and has been mostly predicted using simulations or numerical approaches. Therefore the work in this chapter provides the experimental techniques to quantify the trap stiffness of the DNH tweezer, which could also be extended to other aperture based traps. It would also enable us to compare different aperture based traps and also with other nano-optical tweezers in terms of trap stiffness. In order to determine the stiffness of the DNH tweezers two techniques: autocorrelation of Brownian-induced intensity fluctuations and trapping transient analysis

were used. The DNH tweezer trap stiffness was also compared with other nano-optical tweezers and the conventional single beam tweezers present in the literature.

3.2 Theory

There are several methods used for calculating the trap stiffness associated with the restoring forces of an optical trap. These techniques include the power spectrum method, the equipartition method, optical potential analysis, the drag force method and the direct measurement of the optical force [73]. Most of these techniques require precise measurement of the position fluctuation of the particle in the optical trap for calculation of trap stiffness. This is done experimentally by measuring the intensity fluctuations in the back focal plane of the condenser by means of position sensitive detector or through video microscopy. These detection procedures are usually limited by the precision, temporal resolution and bandwidth especially for particles in the range of few nm. Therefore these techniques used for calculating the stiffness have been mostly limited to conventional optical tweezers and large particle sizes. Although, the position sensitive detection technique has been used to determine the stiffness of a plasmonics tweezer for trapping of 200 nm particles, which was found to be 13 fN/nm with 150 mW of incident laser power [43]. We use the following two techniques to determine the trap stiffness of the DNH tweezer without using a position sensitive detector.

3.2.1 Autocorrelation of Brownian-Induced Intensity Fluctuations

For nanoapertures, the optical transmission through the aperture is related to the position of the particle in the aperture, and therefore the Brownian motion induced fluctuations of

the transmission signal can be used to determine the trap stiffness. Direct observation of the intensity reveals little information, as changes at the millisecond time scale are buried in noise. We show that the autocorrelation of the trapped signal can be used to measure the characteristic time constant (τ_a) and hence the trapping stiffness (κ).

3.2.2 Trapping Transient Analysis

Step response method is one of the widely used techniques to determine the stiffness of the conventional optical trap [56]. The stiffness of the trap is calculated by using the response of the particle to the trap movement. In this method the laser focus or the trap is displaced by a small fixed displacement and the subsequent trajectory of the particle is recorded using a quadrant photodiode. Due to the displacement of the laser focus, the trapped particle is acted upon by a restoring force which restores its position to the center of the trap. The trapped particle returns to its equilibrium position in an exponentially damped manner with a time constant $\frac{\gamma}{\kappa}$. The trajectory of the particle can be written as

$$x(t) = A_o(1 - \exp\left(-\frac{\kappa}{\gamma}t\right) \qquad (3.2)$$

where A_o is a constant, κ is the trap stiffness and γ is the Stokes' drag.

The time constant of the data obtained from the trajectory of the particle described in Equation 3.2 is used to determine the stiffness of the trap. The trapping transient technique used to determine the stiffness of the DNH tweezer is analogous to the step response method related to the drag force of the fluid as compared to the autocorrelation

analysis which is based on thermal vibrations. Like the conventional step response method which measures the time constant (τ) of the particle to return to the trap centre due to trapping forces as opposed to the viscous drag , we here measure the time constant (τ_t) of the particle to fall into the potential well as opposed to viscous drag. This is measured by the transient jump from the untrapped to the trapped state during the trapping instant of the particle.

3.2.3 Trap Stiffness Calculation

The strong field intensity in the DNH produces a potential well which has approximately a harmonic potential around the centre of the trap, due to conservative nature of the optical forces. The time constant obtained through the trapping transient,τ_t, and autocorrelation, τ_a, are used to evaluate the trap stiffness κ.

The motion of a particle in an optical trap under the influence of thermal fluctuation and drag force can be modelled by an over-damped modified Langevin's equation as [67, 74]

$$m\frac{d^2x(t)}{dt^2} = F(t) \qquad (3.3)$$

where m is the mass of the particle, $x(t)$ is the instantaneous position of the particle and F(t) is the total instantaneous force acting on the particle at any instant of time t. The total instantaneous force consist of

1. The **frictional force** due to viscous surrounding medium,$-\gamma v(t)$ propotional to the velocity of the particle under the Brownian motion. The friction coefficient is given by Stokes' law for a spherical particle as

$$\gamma = 6\pi\eta r \qquad (3.4)$$

where η is the dynamic viscosity of the medium. For the present case, the surrounding medium is water with dynamic viscosity given by $\eta = 1 \times 10^{-3}$ Ns/m^2 at room temperature.

2. The **restoring force** of the optical trap -$\kappa x(t)$, where κ is the force constant or the trap stiffness of the optical trap.
3. A **random force** $\zeta(t)$, due to random density fluctuations in the fluid. The random force $\zeta(t)$, is a stochastic Gaussian process giving the effect of background noise due to the fluid on the Brownian particle. The random force satisfy the following condition for a purely viscous medium:

$\langle\zeta(t)\rangle$=0;

Thus the final equation can be written as

$$m\frac{d^2x(t)}{dt^2} + \gamma\frac{dx(t)}{dt} + \kappa x(t) = \zeta(t) \qquad (3.5)$$

The characteristic time for loss of kinetic energy through friction, $t_{inert} = \frac{m}{\gamma}$ is 1000-10000 times shorter than the typical experimental time resolution and therefore the inertial term can easily be neglected. Thus the equation can be simplified to

$$\frac{dx(t)}{dt} = \frac{\kappa}{\gamma}x(t) + \left(\frac{2K_BT}{\gamma}\right)^{\frac{1}{2}}\zeta(t) \qquad (3.6)$$

Using this equation, $\tau_a = \tau_t = \tau$, is related to the trap stiffness, κ, as [75]

$$\tau = \frac{\gamma}{\kappa} \qquad (3.7)$$

For the nanospheres trapped at the aperture of the DNH additional drag force arise due to the wall effects from the nanohole structure. The presence of the flat wall complicates the flow field surrounding the particle due to which the force experienced by the particle is quite different from the three dimensional hydrodynamic drag force, known as Stokes' drag. When a colloidal particle is moving near a flat wall, the motion of the particle is influenced a lot by the presence of the wall [73]. As the distance between the centre of particle and the wall is decreased, the drag force acting on it increasingly deviates from the well-known Stokes' drag force that occurs when the particle is located far from the wall. The increased deviation from the Stokes' drag force is attributed to the hydrodynamics interaction between the particle and the fluid generated by the boundary condition imposed by the flat wall. Taking boundary effects into consideration the Stokes' drag coefficient is estimated using Faxén's law as [76]

$$\gamma = \frac{6\pi\eta r}{\left[1 - \frac{9}{16}\left(\frac{r}{h}\right) + \frac{1}{8}\left(\frac{r}{h}\right)^3 - \frac{45}{256}\left(\frac{r}{h}\right)^4 - \frac{1}{16}\left(\frac{r}{h}\right)^5\right]} \qquad (3.8)$$

where η is the viscosity of the medium, r the radius of the spherical particle and h is the distance from the centre of the polystyrene nanosphere to the wall. We assume h to be 15 nm, giving 5 nm average separations from the wall. This increases the Stokes' drag by 1.61; however, a maximum increase of 3.02 is expected when the particle is touching the wall.

3.3 Experiment and Results

The DNH tweezer set up used in this work is the same as that mentioned in Chapter 2. Polystyrene nanospheres of diameter 20 nm were used for trapping using the DNH tweezers. The DNH with cusp separation of around 28 nm is fabricated which is found to be optimal for trapping 20 nm nanosphere as shown in Figure 3.2 [77]. Figure 3.2 shows the typical trapping event of 20 nm polystyrene nanosphere in the DNH optical trap.

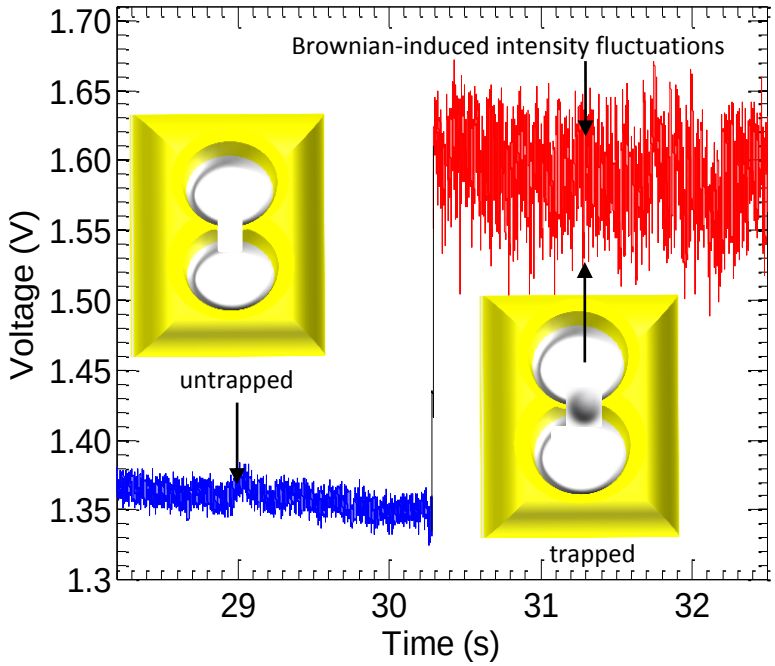

Figure 3.2 Typical time trace of a trapping event of 20 nm polystyrene nanosphere using DNH. The DNH has a gap nearly 28 nm. The transmission signals through the DNH for t< 30.28 s (black) shows the untrapped signal with no particle. At nearly t=30.28s there is a step change in the transmission corresponding to the trapping transient of the particle. For t > 30.3s the particle is trapped in the DNH aperture with large Brownian-induced intensity fluctuation as shown in the transmission signal (red). The transmission signal is down sampled to 1 KHz.

The transmission signal through the DNH aperture is measured by avalanche photodiode (APD). The voltage signal (blue) shows the untrapped state when the particle is not trapped in the DNH structure and the signal (red) shows the trapped part of the signal. The trapped state shown in red shows an increase in the intensity fluctuation of the transmitted signal caused by the Brownian motion of the nanosphere in the DNH optical trap. This signal can be used to determine the autocorrelation function in order to determine the time constant τ_a, which can then be used to evaluate the stiffness of the

trap. Figure 3.3 shows the autocorrelation curve of the trapped and the untrapped state shown in Figure 3.2

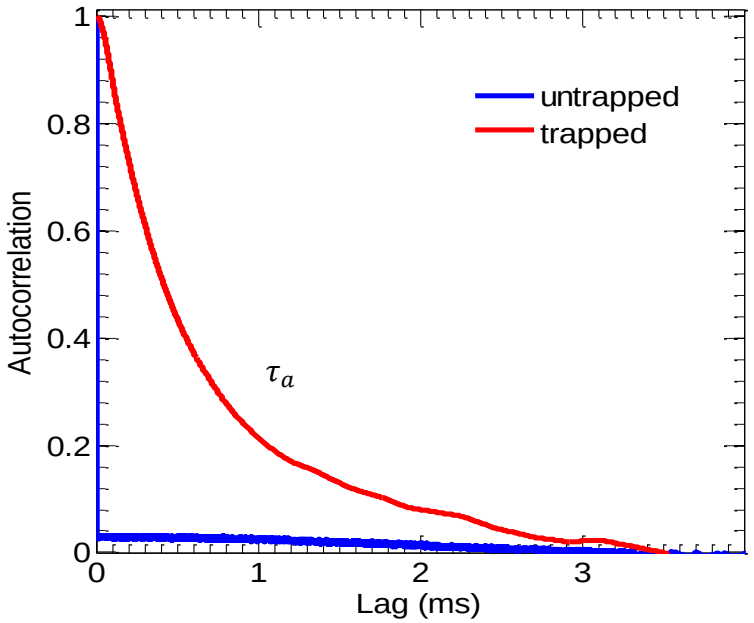

Figure 3.3 Autocorrelation function of the transmission signal in the untrapped (blue) and trapped (red) state. The autocorrelation is taken for a section of the transmission signal through the DNH aperture of length 2-3 s to accurately determine the autocorrelation function.

The autocorrelation curve for the trapped state shows an exponential decay with time constant τ_a, which has been seen in some other previous works too [78]. Since the autocorrelation is directly related to the power spectrum through the Fourier transform, so the results of this approach are equivalent to the power spectrum analysis, which is often used to determine the stiffness of conventional optical tweezers.

The second approach uses the trapping transient method to obtain the time constant τ_t . The transient increase in the transmission signal through the nanoaperture occurs at the instant when the particle enters the aperture. Figure 3.4 shows the zoom version of the transient of the transmission signal during trapping as the signal goes from the untrapped to the trapped state. An exponential fit to the transient shown in red is used to determine the time constant (τ_t) used for calculating the trap stiffness. The trap transient (blue) occurs as the particle is pulled inside the trap into the potential well due to strong optical forces present in the DNH tweezer overcoming the viscous drag as illustrated in Figure 3.4.

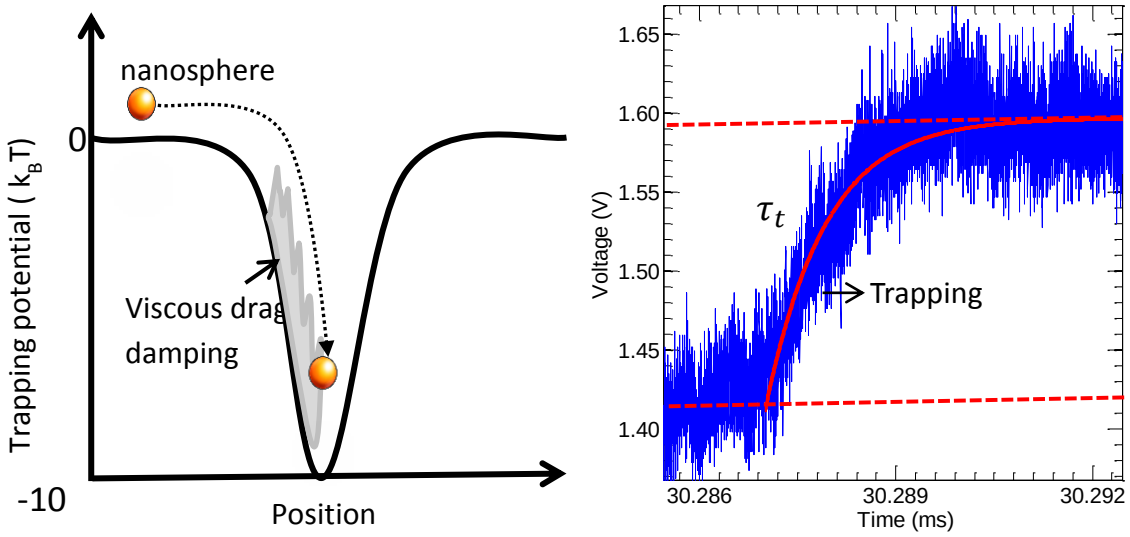

Figure 3.4 (left) Potential energy diagram showing the particle being sucked into the potential well against the viscous drag due to the surrounding medium. (Right) Trapping transient (blue) showing the change in transmission signal through the DNH aperture from untrapped to trapped state as the particle enters the trapping region. The signal is the zoomed version of the transient signal (blue) as shown in Figure 3.2, with an exponential fit (red) to determine the transient time(τ_t).

The characteristic time constant τ_a and τ_t obtained from the large sample space of trapping events (N >10) using both techniques is used to calculate the trap stiffness κ for different incident trap laser powers. The experiment was performed at four different incident laser powers. The DNH trap stiffness shows a linear dependence with the laser power using both approaches. This is expected due to the increase in the strength of the trapping potential with the laser power. The linear relationship of trap stiffness with laser power has also been shown for conventional tweezers [79]. Figure 3.5 shows the values of the time constant and the corresponding trap stiffness as obtained using the autocorrelation of Brownian-induced intensity fluctuations and the trapping transient techniques.

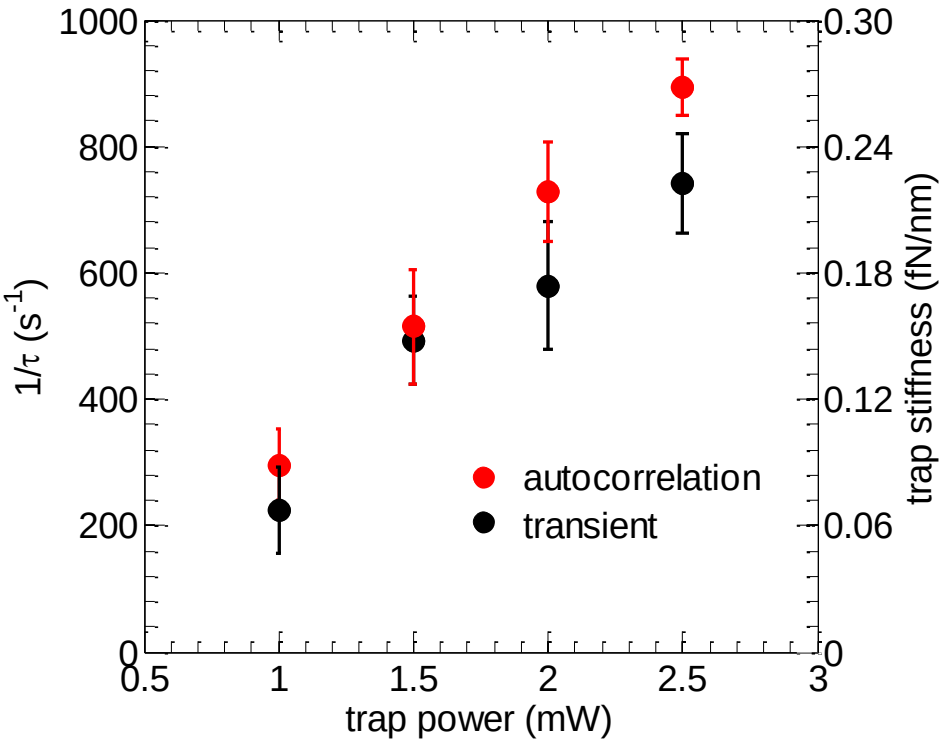

Figure 3.5 Mean characteristic time constants (left axis) and trap stiffness (right axis) calculated using the autocorrelation of Brownian-induced intensity fluctuations (red) and trapping transient (black) methods for different incident laser power obtained from multiple trapping events at each power value (N > 10).

3.4 Discussion

The DNH tweezers trap stiffness was calculated to be around ~ 0.2 fN/nm for 2 mW of incident laser power using both the techniques of autocorrelation and trapping transient. The trapping efficiency was found to be approximately 0.1 fN/nm·mW. For an accurate measurement (10% precision) of the characteristic time constant τ_a from the autocorrelation function, the measurement time used is more than ~1000 τ_a. This is important for the precise calculation of the stiffness value obtained from the autocorrelation function due to the Brownian-induced intensity fluctuations [80, 81]. The

trap stiffness of the DNH tweezer is comparable to the conventional optical tweezers for a ten times larger dielectric particle and laser power of 10 mW [78]. Considering the scaling due to Rayleigh scattering and difference in wavelength, the DNH tweezers is 3000× more efficient. In comparison to other nano-optical tweezer found in the literature the DNH stiffness is comparable to that calculated numerically for coaxial aperture used for trapping of 10 nm polystyrene particles. Table 3.1 shows a comparison of the trap stiffness of different nano-optical tweezer using different nanostructures found in the literature. For comparison with our experiment we have scaled the values for 10 nm polystyrene particles as shown in column 4 of Table 3.1 in lieu of the present work.

Table 3.1Comparison of trap stiffness for different optical traps scaled for 10 nm dielectric sphere. a Exp.: Experimental, Sim.: Simulation, b Scaled by Clausius-Mossotti factor to account for increased refractive index contrast used in calculations.

Structure	Method [a]	Stiffness fN/nm·mW	Scaled Stiffness $(\times \left(\frac{10\ nm}{r}\right)^3$ fN/nm·mW
nano pillar [43]	Exp.	0.013	0.013×10^{-3}
slot waveguide [47]	Sim.	0.200	0.001
plasmonic nano cavity [64]	Sim.	0.018	0.018
plasmonic nano block pair [50]	Exp.	4.000	0.030
double nanohole*	Exp.	0.100	0.100
slot waveguide [82]	Sim.	0.131	0.131
cylindrical aperture [62]	Sim.	6.600	0.400
coaxial plasmonic aperture [67]	Sim.	0.190	1.56 (0.36^b)
Conventional single beam [78]	Sim.	0.030	0.3×10^{-4}

The current techniques used to calculate the trap stiffness can be used for evaluation and calibration of traps, especially when working with Rayleigh particles of the given range. Our approach can be used to quantitatively determine the efficiency of different aperture trapping systems and thereby assess their usefulness for applications including the analysis of protein folding, binding and studying individual viruses.

Chapter 4. DNH Optical Tweezers for Sensing

4.1 Introduction[2]

Optical tweezers in the past have been used to study properties of particles in the solution like electrostatic and molecular interactions, Brownian motion, and hydrodynamic fluctuations [83-87]. In this chapter, the DNH optical tweezer is used as a sensor for sensing the concentration and size of nanoparticles in addition to trapping. The DNH tweezer is also used to determine the refractive index of the particle by observing the percentage change in the transmission signal intensity at the trapping instant. With the integration of particle sensing ability of the DNH optical tweezer with the chemical analysis technique of Raman spectroscopy, it is possible to determine the concentration, size and composition of the nanoparticles on a single platform.

4.2 Theory

The idea is derived from diffusion theory based on simple microfluidic conditions. The diffusion time (τ) of the nanoparticles in the trapping solution inside a microfluidic chip is directly proportional to the time-to-trap (t_t). Time-to-trap is the time taken by the optical tweezer to trap the nanoparticle after the laser beam is turned on and a statistical analysis of the time to trap (t_t) can be used to determine the concentration and size of the nanoparticles in the solution. Furthermore the percentage change in the transmission

[2] The following chapter is adapted from: **Sensing nanoparticles using a double nanohole optical trap**. Abhay Kotnala, et al. Accepted for publication by the Lab on a Chip in 2013. Copyright Permission Accepted.

intensity at the trapping instant scales according to the Clausius–Mossotti factor, and therefore can be used to determine the refractive index (n) of the particle.

4.2.1 Time-to-trap as a Function of Size of Nanoparticles

It is expected that the mean trapping time depends linearly on the size of the particle by the considering the Stokes'-Einstein equation [88]:

$$D = \frac{k_B T}{6\pi\eta a} \qquad (4.1)$$

Where k_B is the Boltzmann constant, T is the temperature, η is the viscosity and a is the radius of the spherical particle. The diffusion coefficient is defined as:

$$D = \frac{l^2}{\tau} \qquad (4.2)$$

l is a characteristic diffusion length, τ is a characteristic diffusion time. Since we expect that the time-to-trap (t_t), scales linearly with the diffusion time τ (i.e., faster diffusion makes trapping occur faster since the nanoparticle visits the trapping region more quickly), this gives:

$$t_t \propto a$$

Therefore, we expect a linear dependence of time-to-trap with the size of the polystyrene nanospheres.

4.2.2 Time-to-trap as a Function of Concentration of Nanoparticles

A simple theory would predict a -2/3 power dependence of time-to-trap on the concentration of nanoparticle. The average diffusion length, l to the trap is related to the concentration,c, as:

$$l \propto c^{\frac{-1}{3}}$$

Therefore, using the equation for the diffusion constant gives:

$$t_t \propto c^{\frac{-2}{3}}$$

Hence, we expect a -0.667 power dependence of time-to-trap with the concentration of the nanoparticles.

4.3 Experiment and Results

The experimental set up used for the experiment was similar to that used in Chapter 3 except the chip containing the trapping solution. For this particular experiment we use a microfluidic chip and a syringe pump for delivery of the desired nanoparticles solution. The idea of using a microfluidic chip is to maintain identical microfluidics conditions for

trapping different concentration and sizes of nanoparticles. The change in the microfluidics environment set up every time while performing trapping of different concentration and sizes of nanoparticles might influence the relative accuracy of time-to-trap (τ_t) parameter used for sensing. Figure 4.1 shows the DNH tweezer system with a microfluidic chip and syringe pump connected to the chip for injecting the desired concentration and size of the nanoparticle solution. The microfluidic chip consists of DNH structures with different cusp separations for efficient trapping of the desired size of nanoparticles. The specific cusp separations were chosen to provide size selective efficient trapping of nanoparticles as will be discussed later. The separation between the cusps are 28 nm, 50 nm, 68 nm, which are nearly optimal for trapping of different sizes of nanoparticles (20 nm, 40, nm and 60 nm), shown in Figure 4.2a, b, c. Nanoparticle solutions consisting of 20 nm polystyrene sphere (Thermo-Scientific n=1.57) of different concentrations of 1, 0.3, 0.1, 0.05, 0.01% w/v and size of 40 nm and 60 nm were made for doing the experiment. The nanosphere suspensions were ultrasonicated to ensure that there is no aggregation of the polystyrene nanospheres.

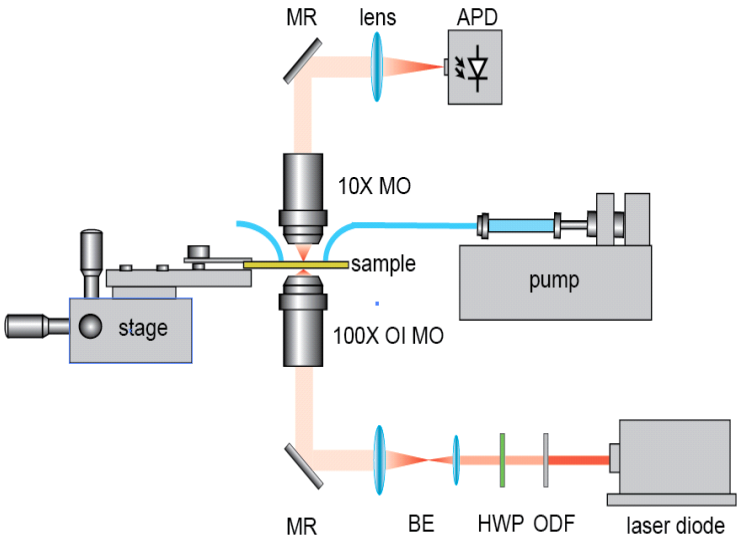

Figure 4.1 Experimental setup of the DNH tweezer for use as a sensor. A microfluidic chip is used for optical trapping and the solution is flowed into the channel using a syringe pump. A detailed view and fabrication details of the microfluidic chip is presented in Appendix B.

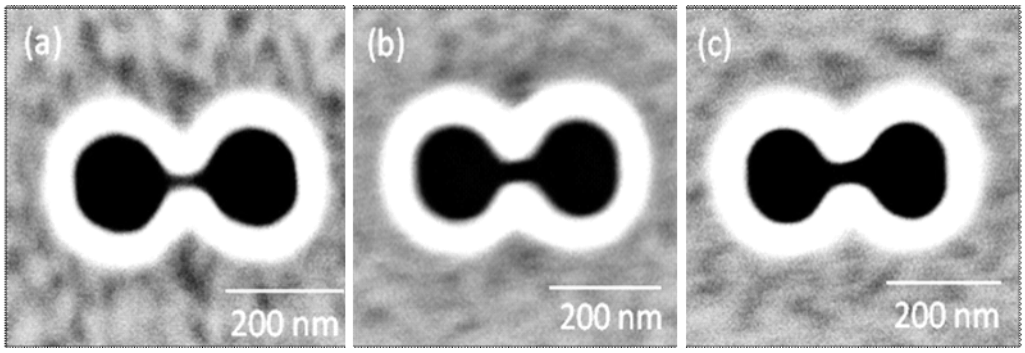

Figure 4.2 SEM images of DNH with different cusp gap size for efficient trapping of different size of nanoparticles (a) 28 nm (b) 50 nm (c) 68 nm

4.3.1 Procedure

Nanoparticle solution of desired concentration and size was flown using the syringe pump into the microfluidic channel. The laser focussed on the DNH structure is then turned on, and the transmission data through the DNH is recorded till the particle is trapped in the DNH. Figure 4.3a shows the typical trapping event of the 20 nm polystyrene sphere. The quantity of interest in this work is the time-to-trap (t_t) after the laser is switched on as shown in Figure 4.3a. The laser power was kept constant during the experiment.

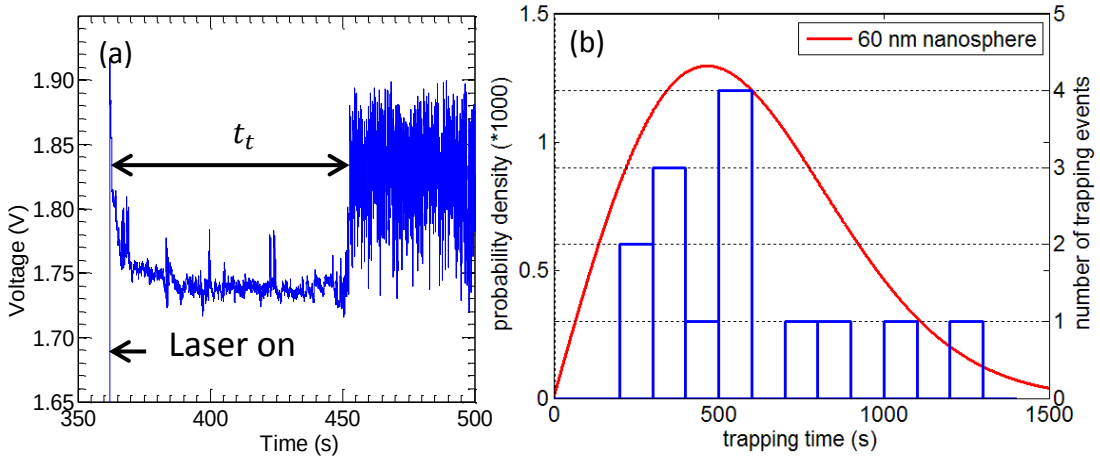

Figure 4.3 Typical trapping event for 0.1 w/v % concentration of 20 nm polystyrene particle. The laser was turned on at t=362.5 s and used as reference to measure the time to trap which occurs at approximately t=455 s. (b) Distribution of time-to-trap (t_t) for 60 nm polystyrene particles with Rayleigh fit.

Also the laser was closed for more than 60 s after the occurrence of trapping in order to release the particle and make accurate measurement of time- to-trap (t_t) variable, for the next consecutive trapping events as shown in Figure 4.4. A large sample space of the

trapping events (usually N >15) were recorded to measure the time to trap (t_t) for different concentration and size solutions mentioned in the previous section.

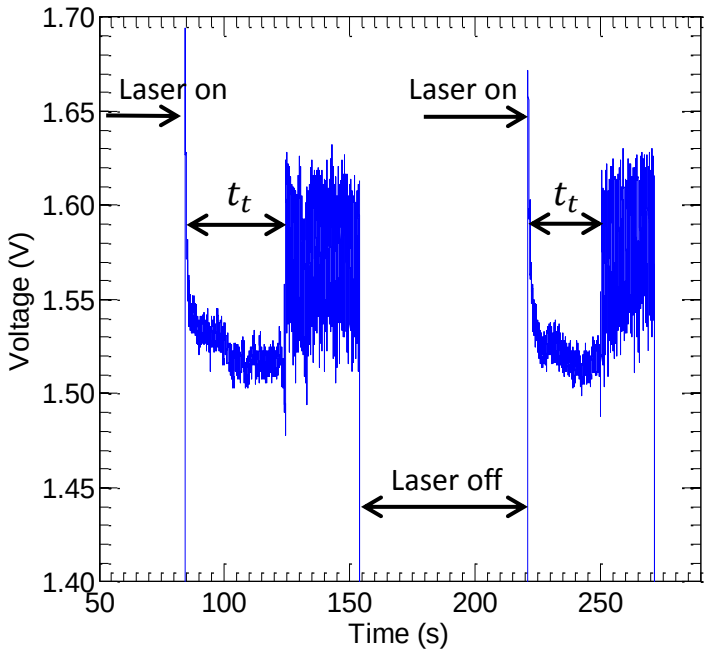

Rayleigh distribution can be used to model the time-to-trap of the particles to reach the trapping site through multiple random paths. This assumption is due to the random walk nature of the particles in the solution due to Brownian motion. This distribution describes the distance travelled in a random walk, so it is reasonable to expect that the distance travelled towards the aperture is a fraction of these random walks, since there is no preferred direction. A statistical analysis of the time-to-trap (t_t) shows a Rayleigh

distribution of the probability density of the time-to-trap data for 60 nm polystyrene nanospheres as shown in Figure 4.3b [89].The probability density function of the Rayleigh distribution is given as:

$$f(t_t;\sigma) = \frac{t_t}{\sigma^2} e^{-\frac{{t_t}^2}{2\sigma^2}}, \quad x \geq 0\ ; \qquad (4.3)$$

where σ is the scale parameter of the distribution.

The Rayleigh fit has a mean value of 586.2 s with the lower and upper confidence limit of 384.1 s and 601.5 s for 90% confidence interval of the time-to-trap parameter. Even for wider spread of the distribution of the events, the distribution appears to be converging to a specific mean time. The data is enough to fit a Rayleigh distribution and estimate the mean time-to-trap with large probability for a given size of nanoparticle solution. Therefore it is possible to sense the different sized nanoparticle solutions using the present data. The margin of error can still be decreased by increasing the number of events for a given nanoparticle solution in order to get a more accurate fit and hence a better estimation of the time-to-trap parameter, especially when dealing with nanoparticle solutions with small difference in their sizes. The appearance of some random events far away from the mean value could be due to the drift or other environmental effects, which may be affecting the experiment.

4.3.2 Nanoparticle Size Sensing

Figure 4.5 shows the mean time-to-trap for different particle sizes (20 nm, 40 nm and 60 nm diameter) of polystyrene nanospheres as a function of their diameter. For efficient trapping of polystyrene nanoparticles of different sizes, DNHs having optimal cusp

separation (s) for respective size of nanoparticles were used. It is clear that the straight line, linear fit shows very good agreement with the mean time-to-trap variation with particle size. This is in agreement to the theoretical consideration of time-to-trap obtained using simple microfluidic theory mentioned in section 4.2.

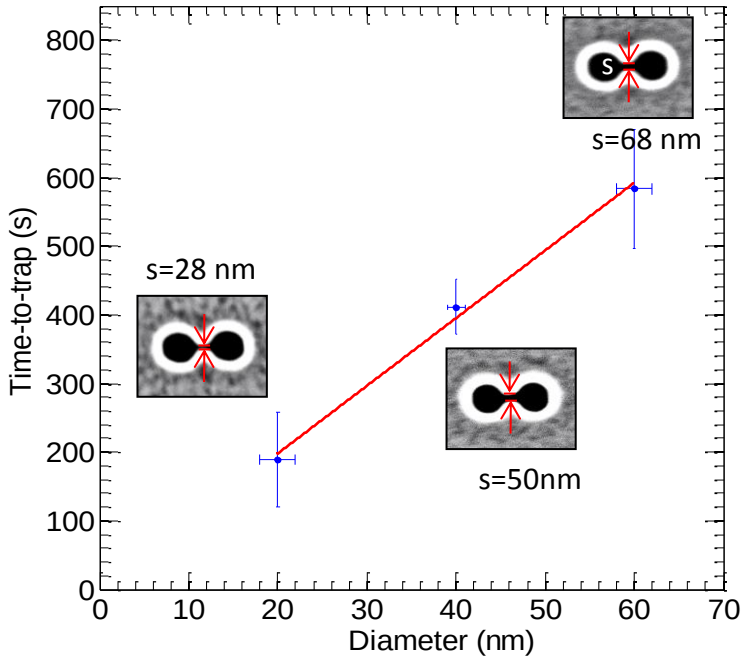

Figure 4.5 Mean time-to-trap for different polystyrene spheres of diameters 20 nm, 40 nm and 60 nm. The horizontal and vertical error bars are standard deviation (manufacturer specified) and standard error of nanosphere size and trapping time respectively. The straight line represents linear fit to the data.

4.3.3 Nanoparticle Concentration Sensing

Figure 4.6 shows the average time-to-trap as a function of concentration for 20 nm polystyrene spheres. We find -0.655 power dependence, which is in good agreement with the formulation presented in section 4.2.2.

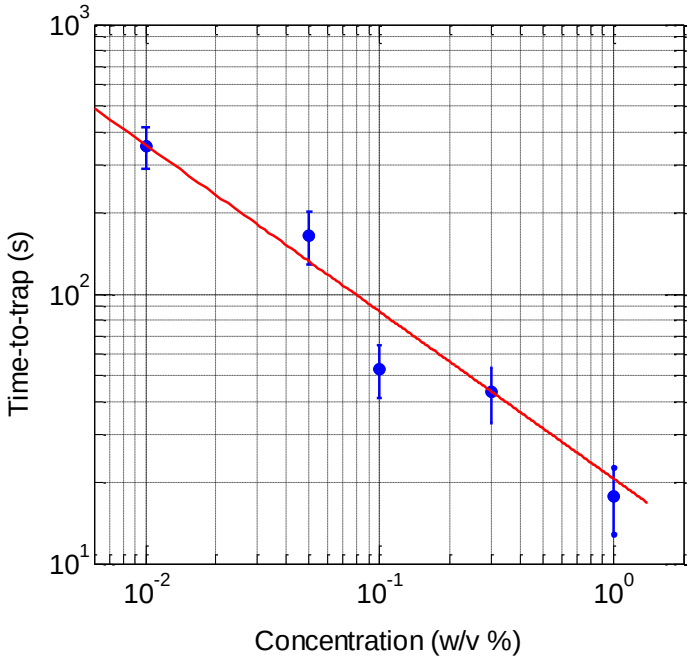

Figure 4.6 Average time-to-trap for varying concentrations of 20 nm polystyrene nanospheres in aqueous solution on a log-log scale. The dot represents the mean trapping time over multiple events (typically 10-20) for each concentration. The bar represents the standard error of the data. The straight line represents the power fit to the data.

4.3.4 Nanoparticle Refractive Index Sensing

The refractive index of the particle can also be determined using the DNH optical trap. This is based on the observation of the percentage step change in the transmission signal through the DNH aperture at the instant when the particle is trapped. This change in transmission is dependent on the refractive index contrast between the particle n_p and the surrounding medium n_m, since the scattering cross section of dielectric sphere vary as $\left({n_p}^2 - {n_m}^2\right)^2$ [90].Keeping the surrounding medium constant ε_m, the increase in the

particle refractive index would result in a corresponding increase in the transmission signal during trapping. We can quantitatively attribute this to the trapping efficiency for spheres which is expected to scale, at least to first order, as the Clausius–Mossotti factor given by:

$$K = \frac{\varepsilon_p - \varepsilon_m}{\varepsilon_p + 2\varepsilon_m} \qquad (4.4)$$

where ε_p is the dielectric constant of the nanoparticle and ε_m is the dielectric constant of the surrounding medium. The Clausius-Mossotti factor indicates the relative polarizability of the particle with respect to its surrounding medium.

The experiment for refractive index sensing was carried using 20 nm spherical particles of silica (SiO_2) and titanium dioxide (TiO_2) (Sigma-Aldrich) having refractive index of 1.46 and 2.44 at the wavelength of 820 nm. Figure 4.7 shows the percentage change in the transmission signal measured as voltage change for three different particles (Silica, Polystyrene and Titania). We found that the transmission change was smaller by a factor of 1.1 for silica particles and 3.3 times larger for the titania spheres as compared to the polystyrene nanospheres trapped earlier. This is due to the smaller refractive index of silica and larger refractive index for titania spheres in comparison to polystyrene spheres. Typical trapping events for all the three particles showing the comparison of the transmission signal at the trapping instant is shown in Figure 4.8. The Clausius–Mossotti factor is smaller by a factor of 1.8 for silica and 3.8 times larger for titania nanospheres in comparison to polystyrene nanospheres. The experimental transmission change obtained

for titania is smaller as compared to the Clausius–Mossotti factor but would still estimate the refractive index of the particle within 10 % error (n=2.24). However for the silica particles, there is a larger deviation in between the transmission change and the Clausius–Mossotti factor. The error might be attributed to the larger variation in the shape and size of the silica nanospheres, which would result in larger transmission change than expected. Therefore careful calibration of the size and shape of the different refractive index nanospheres is necessary for accurate measurement based on this technique.

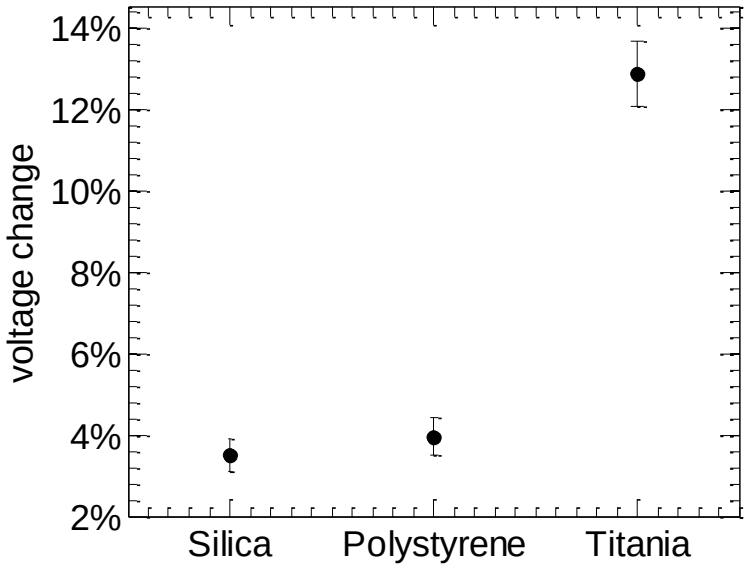

Figure 4.7 Percentage change in the transmission signal measured at the trapping instant when the particle goes from the untrapped to trapped state for different refractive index particles, silica (n=1.46), polystyrene (n=1.57) and Titania (n= 2.44). The dot represents the mean value of the percent voltage change for multiple trapping events (N >10) and the error bar the standard deviation in the data**.**

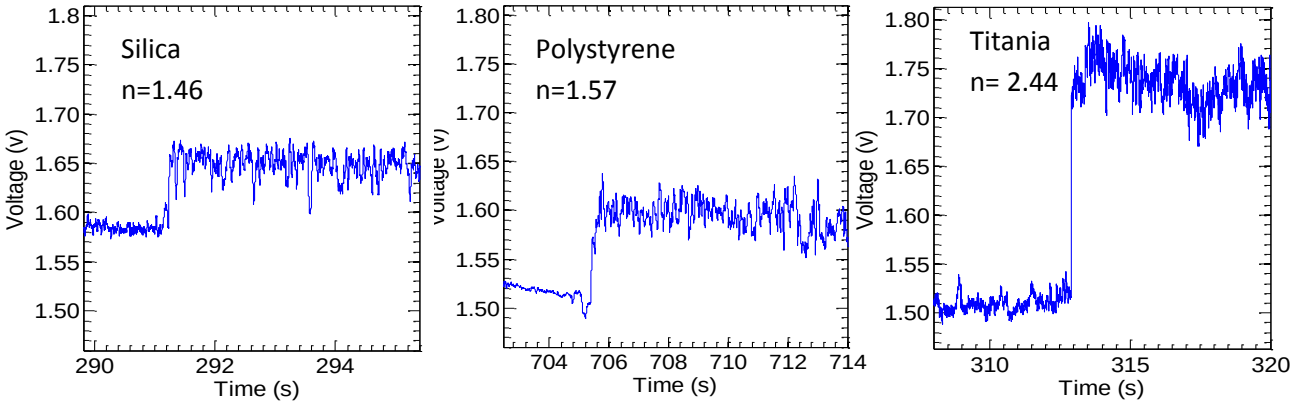

Figure 4.8 Typical trapping event of trapping of 20 nm silica, polystyrene and titania spheres. The percentage change in transmission is more for a higher refractive index particle.

Based on these results and with suitable calibrations, the particles refractive index can be determined by observing the relative transmission step size at the onset of trapping to a known sample. The calibration requires keeping the parameters such as trapping laser power, the DNH shape and size, and the optical setup same for all the measurements. This provides for accurate measurements of the relative percentage change, as these parameters also affect the percentage change in transmission for the trapping event.

4.3.5 Heterogeneous Populations

To confirm the size selectivity of DNH tweezer, DNH with 28 nm cusps gap separation was used to measure the trapping events, time-to-trap for the following mixtures: 0.1 w/v % 20 nm and 0.1 w/v % 40 nm, 0.1 w/v % 20 nm and 0.1 w/v % 60 nm, and 0.1 w/v % 40 nm and 0.1 w/v % 60 nm. We found that the mean trapping time for the prepared mixtures with the 20 nm particles present were consistent with the mean trapping time

recorded for the homogeneous 0.1 w/v% 20 nm solution. The trapping events of the 40 nm and 60 nm polystyrene nanospheres on the DNH with 28 nm spacing showed no clear step change in the transmission signal intensity.

The DNH with large cusps gap size of 68 nm used for trapping of 60 nm polystyrene spheres has weaker confinement of the mode. This results in the weaker interaction of the 20 nm trapped particle with the local field intensity in the DNH gap and therefore gives a small transmission change for identical incident power intensity as compared to the 60 nm particles. The transverse mode confinement increases for decreasing gap sizes. In agreement with earlier studies, the enhancement of the local electric field intensity at the center of the gap ranges from below 100 for the 30 nm gap to below 10 for the 85 nm gap [90].

4.4 Discussion

The DNH tweezer as a sensor is mainly limited by the acquisition time. This is because we require a large sample space of the trapping events to accurately determine the time-to-trap t_t , or percentage change in transmission values with maximum precision. This has also been a major challenge for low concentration sensors in general [91]. This limitation can be overcome by imaging multiple traps in a narrower channel, thereby parallelizing the process [92]. Some deviation from simple microfluidic theory are expected at higher concentrations or due to surface-hydrodynamic effects but the concentration ranges used in the experiment are far from the range where these factors come into play [91]. Some deviation from equation (1) is expected at higher

concentrations because of collective diffusion effects [93]; however, for the concentrations considered in this work the change in the diffusion constant due to collective effects is less than 1% [94]. Also, some deviation from simple microfluidic theory is expected from surface-hydrodynamic effects. These effects, however, typically turn on at a distance which is comparable to the particle diameter [43], which is much less than the typical diffusion lengths of this work, and therefore is expected to play a negligible role.

The present technique has a great potential for sensing applications as it allows size selectivity in heterogeneous samples, sensitivity down to the single particle level, handling of large dynamic range of concentrations, and isolation/analysis (e.g., spectroscopy) of particles once trapped. This could be useful is in the study of virus populations in biological samples, where the population levels vary of many orders of magnitude, there is great heterogeneity in the population, and it is interesting be able to isolate and study individual virons [95] .

Chapter 5. Single Molecule Protein-DNA Interactions using DNH Tweezer

[3]

5.1 Introduction

Optical tweezers have been widely used to study biomolecules such as proteins, DNA and their interactions, all at single molecule level, making it a very useful tool in the field of biophysics [26, 96-97]. Since the biomolecules of interest such as proteins and DNA strands are of sizes usually less than 100 nm, it is not possible to study these molecules by directly holding them with single beam laser tweezer, without using damaging laser powers as discussed in detail in Chapter 1. Therefore most of the past works on the study of biomolecules using the conventional tweezer use the techniques of tethering and fluorescent labeling of the biomolecules [26]. This involves attaching the molecule of interest to a micron sized bead, which can then be trapped using conventional tweezers without using damaging laser powers directly on the molecule of interest [98]. Also due to small scattering cross section of the molecules it is not possible to see their dynamic processes and interactions with other molecules. So, fluorescent labels are used to monitor dynamic processes, such as protein binding [32] and unzipping [99]. These techniques suffer from some inherent limitations such as modification of the natural state of protein/DNA [32], restriction of free motion, heating of the molecule, photo bleaching , poor signal to noise ratio, limited to long DNA strands , as well as increased cost and complexity. This chapter attempts to use the ability of the DNH tweezer to hold on to

[3] The following chapter is adapted from: **Double nanohole optical tweezer visualize protein p53 suppressing unzipping of single DNA hairpins**. Abhay Kotnala and Reuven Gordon. Accepted for publication by the Biomedical Optics Express in 2014. Copyright Permission Accepted.

very small molecules without requiring tethering and also the high sensitivity of the transmission signal to the trapped specimen, to provide an alternative method for studying protein-DNA interactions.

The chapter discusses the DNH optical tweezer as a free-solution, label-free single-molecule probe for protein–DNA interactions. The DNH tweezer was used to trap and unzip a 20 base hairpin DNA molecule. The interaction of the transcription protein p53 with the hairpin DNA provides resistance to the unzipping of the hairpin DNA due to the optical forces of the DNH tweezer system showing a strong binding with the DNA. We also show that the mutant p53 which has partial loss in binding activity has almost no effect on the unzipping behaviour and may be attributed to its inability to fight cancer in human cells. DNH tweezer provides ultra-sensitive detection and quantification of protein–DNA interactions which could revolutionize the fight against genetic diseases.

5.2 Experiment and Results

The optical tweezer setup used for the present study is the same as described in Chapter 2. The DNH were fabricated using FIB with a cusp spacing of around ~ 10 nm in order to efficiently trap the protein and DNA molecules which are of the order of few nm. The small cusp spacing provides for a smaller confinement of the field intensity, which improves the sensitivity of the transmission signal due to larger interaction of the biomolecule with the scattering field. Figure 5.1 shows the SEM image of the DNH used for trapping in the present work.

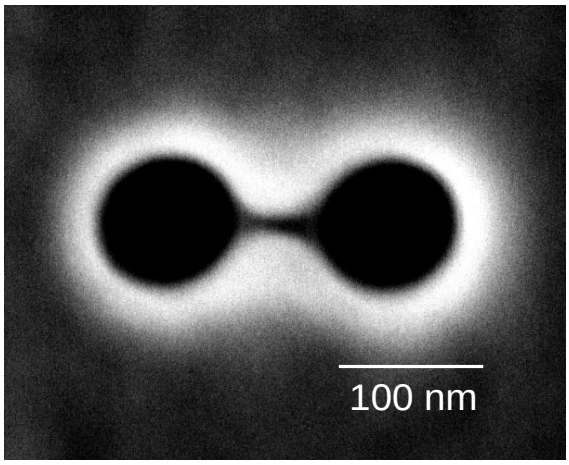

Figure 5.1 SEM image of the DNH with cusp separation of ~ 10 nm used for trapping the ssDNA and the protein**.**

5.2.1 Unzipping of 20 base Hairpin DNA (Stem-loop Configuration)

The DNH tweezer system was used to trap two different 20 base DNA strands, and observe their dynamics during trapping. The DNA sequences used were 5′-GGG CGG GGA GGG GGA AGG GA −3′ and 5′- AGG CAT GCC TAG GCA TGC CT −3′ (Integrated DNA Technologies). The presence of complementary bases in the same single strand of the second DNA sequence results in the folding of the DNA on itself to form a hairpin structure or the stem-loop configuration. The pairing of complementary bases results in gain of energy of several k_BT per pair. The hairpin structure consists of a common loop called a tetraloop with ATGC configuration and is particularly stable due to base stacking interaction of its component nucleotides.

The DNH tweezer traps and unzips's the 20 base hairpin DNA molecules due to the strong optical forces produced by the DNH tweezer. The unzipping force is usually in the

range of 10-20 pN [100]. The trapping transmission signal for the hairpin DNA shows an intermediate step of time (Δt). This was found consistently for different trapping events with a mean intermediate step time of approximately 100 ms. The initial change in the transmission signal intensity is due to the trapping of the hairpin DNA, while the second transition indicates the unzipping caused due to the increases in the polarizability of the ssDNA molecule as a result of elongation of DNA. The experiment was repeated for sequence 1, single strand DNA (ssDNA) with no hairpin structure which showed no such intermediate step as expected and shown in Figure 5.2a. This was found to be consistent for large number of trapping events. The trapping and unzipping behaviour can be explained by a simple energy reaction diagram shown in Figure 5.2c. The hairpin DNA is initially trapped with approximate potential energy of ~10 $k_B T$, as suggested by Ashkin for stable trapping [6] and followed by unzipping requiring approximately the same energy. This is evident from the similar change in the transmission intensity during trapping and unzipping. Since the optical trapping potential scales with the intensity, we can estimate that the change in transmission intensity is proportional to the change in energy potential from trapping.

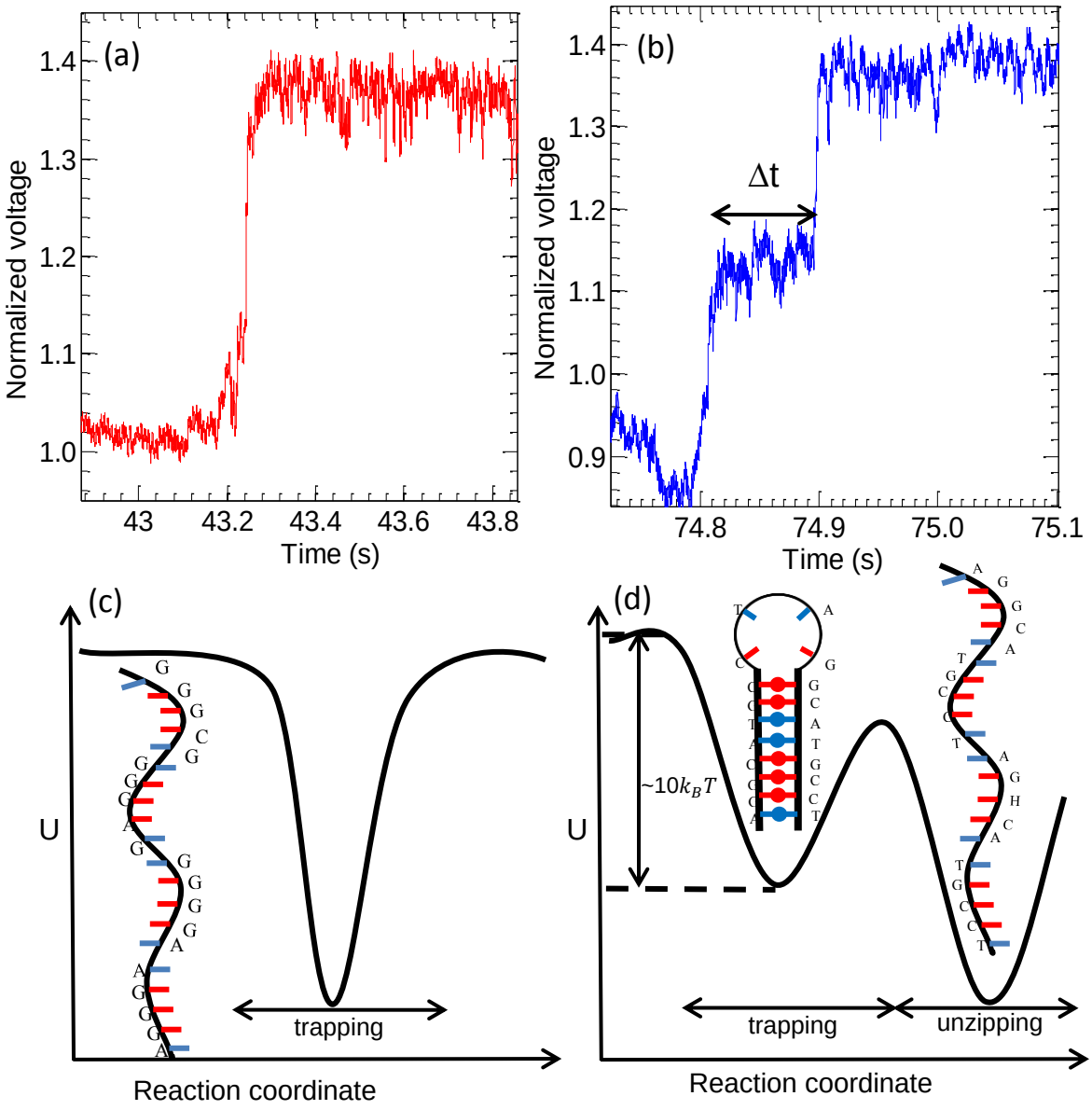

Figure 5.2 (a) Typical optical trapping event of a single strand DNA. (b) Typical trapping event of hairpin DNA showing the unzipping with an intermediate step of ~ 100 ms. (c) Energy reaction diagram of single strand DNA. (d) Energy reaction diagram showing the change in the potential energy diagram due to the energy barrier provided by the base pairing in the stem region. $\boldsymbol{k_B}$: Boltzmann constant, T: Temperature

5.2.2 Wild-type p53 Interaction with Hairpin DNA

In this section we show the effect of DNA binding tumor suppressor protein p53 on the hairpin DNA. p53 is an important tumor suppressor transcription protein, the mutation of which is responsible for nearly 70 % of the known cancer. The most common mutations are the single point mutations in the DNA binding domain of the protein, which binds to the specific DNA sequence for protein activation and performing its biological function.

p53 (Cedarlane Labs, CLPRO742) can bind specifically to the hairpin DNA sequence used in the experiment. The 20 base DNA fragment has a strong binding affinity for p53 DNA binding domain with a value of log $K_d = -7.38$ [100]. Due to the strong binding affinity K_{off} (unbinding coefficient) is very small and hence binding is almost irreversible. The DNA binding protein can stabilize or destabilize the DNA structure and hence affect the unzipping behavior of the hairpin DNA in the optical trap. The p53 protein-DNA complex was trapped using the DNH tweezer and the transmission signal through the DNH was recorded. The transmission signal was found to have similar characteristic as the transmission signal obtained from the trapping of the hairpin DNA molecule except, with an increase in the unzipping time (Δt) as shown in Figure 5.3a. The interaction of the wild-type p53 with the hairpin DNA results in the suppression of the unzipping phenomenon which is evident by increase in the unzipping time. This might be attributed to the strong binding strength of the p53 to the DNA molecule, critical for the biological activity of p53 as also shown by fluorescence anisotropy [100]. The

cumulative probability plot shown in Figure 5.4b shows the unzipping time Δt always greater than 1s for wild type p53–DNA complex as compared to that of DNA for a given probability range.The binding of the p53 to the DNA hairpin changes the energy reaction model by increasing the energy barrier (ΔU) between the trapped and unzipped state. It is this increase in the energy barrier, ΔU, that results in longer unzipping time (Δt) and is a measure of the unzipping suppression energy ΔU.

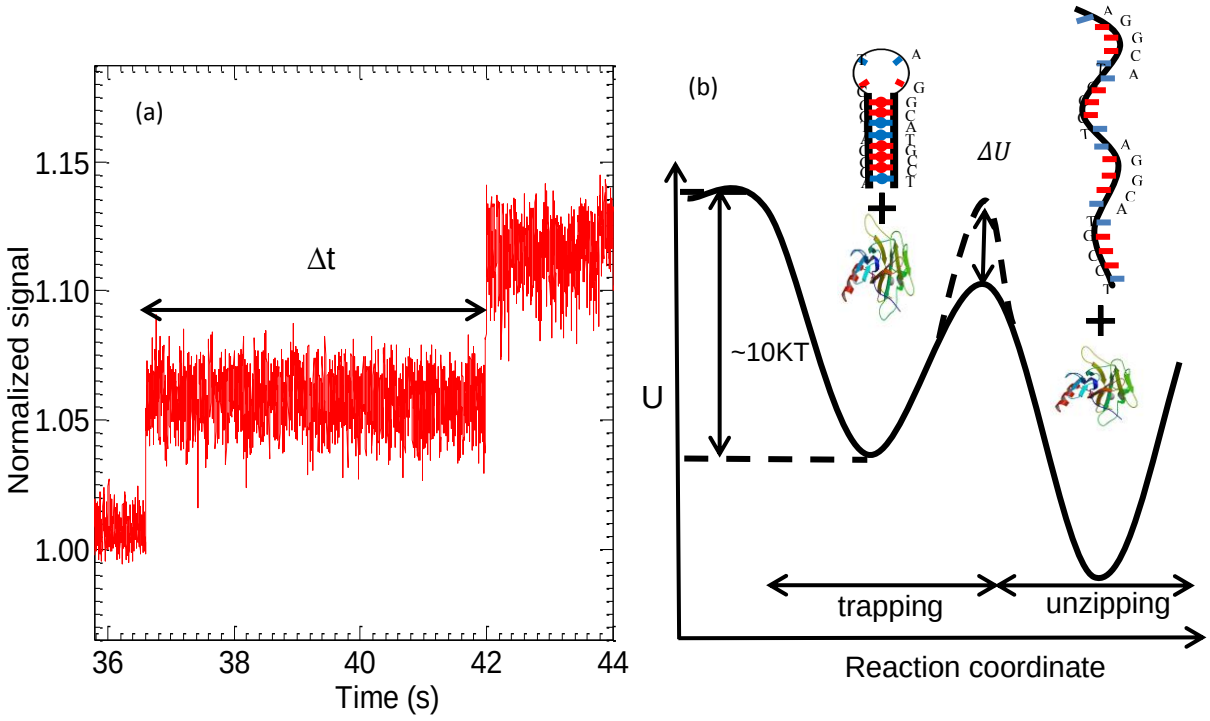

Figure 5.3 p53 interaction with DNA hairpin (a) Typical trapping event of p53 protein-DNA complex showing an increase in the intermediate step of ~ 5s (b) Energy reaction model showing the increase in the unzipping barrier by ΔU due to the binding of the p53 protein with the consensus hairpin DNA.

5.2.3 p53 Mutant (cys135ser) Interaction with Hairpin DNA

The mutant form of the p53 protein, cys135ser (Cedarlane Labs, CLPRO301) was also used to form p53 mutant-DNA complex. There are many mutant forms discovered for p53 molecule which results in its loss of activity in various manners. The mutant considered in this experiment consists of a single point mutation in the DNA binding domain of the p53 molecule. In this mutant the cysteine is replaced by serine which results in a partial loss in the binding activity of the p53 to the DNA molecule. The mutant p53-DNA complex is also trapped using DNH tweezers and the finding was found to be in complete contrast to wild-type p53. Though the mutant p53 results in partial loss in the binding activity [101], but completely loses its ability to suppress the unzipping of the DNA hairpin shown by Figure 5.4a with no appreciable change in the unzipping time (Δt). Figure 5.4b shows the almost overlapping cumulative probability distribution of the unzipping time (Δt) of DNA and mutant p53-DNA complex, calculated from a large sample space of the corresponding trapping events. The DNH tweezer helps to understand and distinguish between the interactive behavior of the wild-type and mutant p53 with the DNA showing the specificity required by a single molecule sensor.

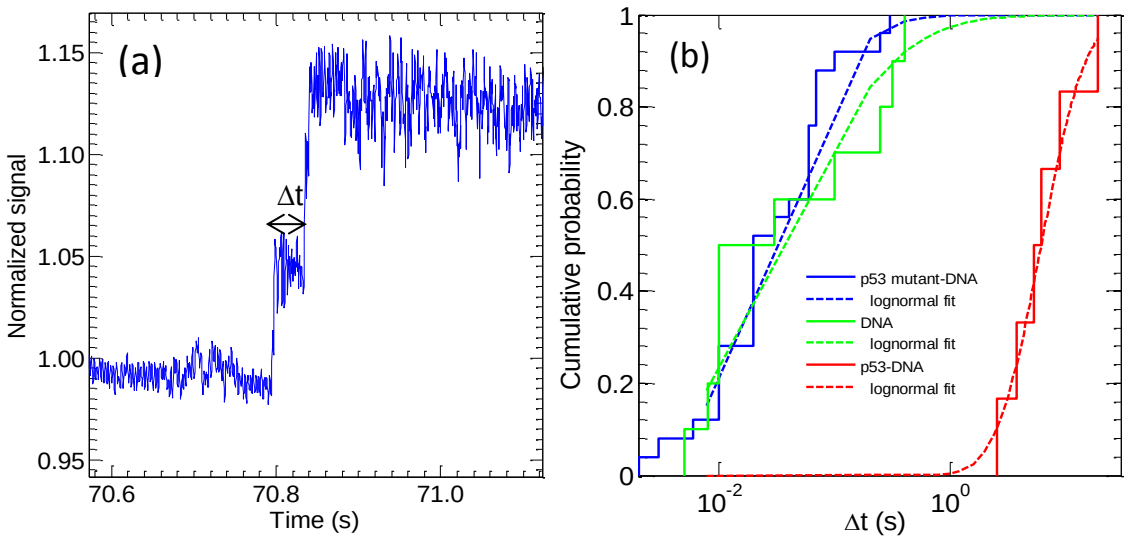

The strength of suppression of the unzipping of hairpin DNA by the p53 transcription protein can be quantified as unzipping suppression energy (ΔU), in terms of the average unzipping times (Δt). Using the Arrhenius behaviour ΔU is given by

$$\Delta U = -k_B T ln \frac{\Delta t_{p53}}{\Delta t_{DNA}} \qquad (5.1)$$

Where, $\Delta t_{p53}$and Δt_{DNA} are the mean unzipping time obtained from a log-normal distribution fit to unzipping time Δt of p53– DNA and DNA respectively. Using equation 5.1 energy barrier corresponding to the suppression energy was found to be approximately 2 ×10^{-20} J or ~ $5k_B$T. The suppression energy is found to be of the same order of magnitude as the calculated binding energy of p53 and DNA found using fluorescence anisotropy for the given hairpin DNA sequence [101].

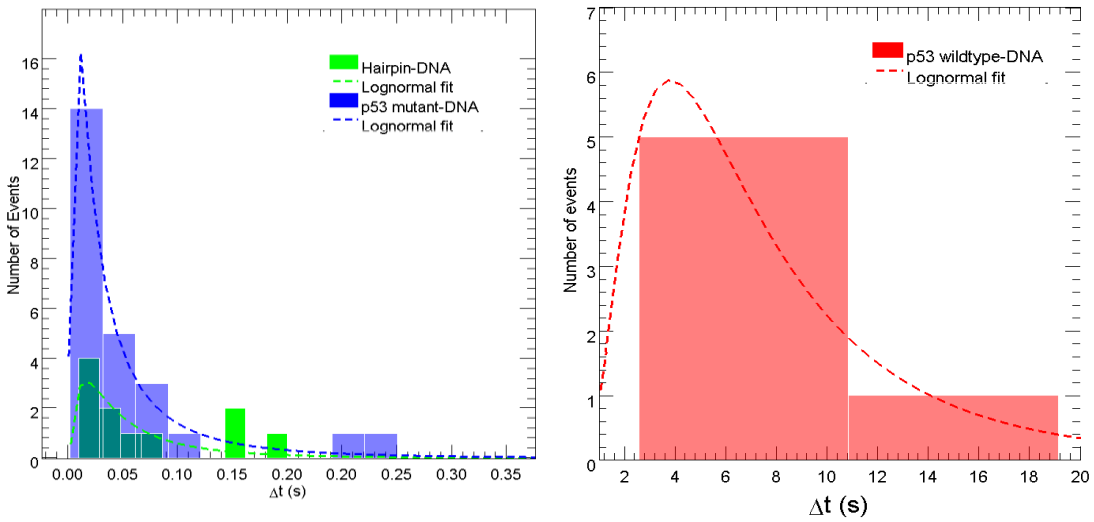

Figure 5.5 Distribution of the unzipping times Δt for hairpin DNA, wild-type p53-DNA and mutant p53–DNA complex for multiple events with a log-normal fit. The distribution of the hairpin and mutant-DNA overlap over similar range of unzipping times, showing minimum effect of the mutant in acting against the unzipping of the hairpin.

5.2.4 p53 Mutant and Wild-type Trapping

We also trapped the wild-type and mutant forms of the p53 protein individually to ensure that we were not trapping p53 alone in the above measurements. Figure 5.6 shows typical events are for both. Both the trapping events look almost identical with small optical scattering and slightly unstable behavior. The events have a smaller transmission change than from the protein – DNA complex and from the DNA alone due to lower scattering of the signal by the p53 molecule which has a spherical conformation with less polarizability compared to protein-DNA complex and DNA. Also, a lower refractive index of p53 molecule as compared to DNA may also cause a smaller change in

transmission signal. The nearly identical trapping behavior of the mutant and the wild-type is because of minimal structural difference between the two proteins as has been illustrated for single point mutant (cys135ser) numerically [102].

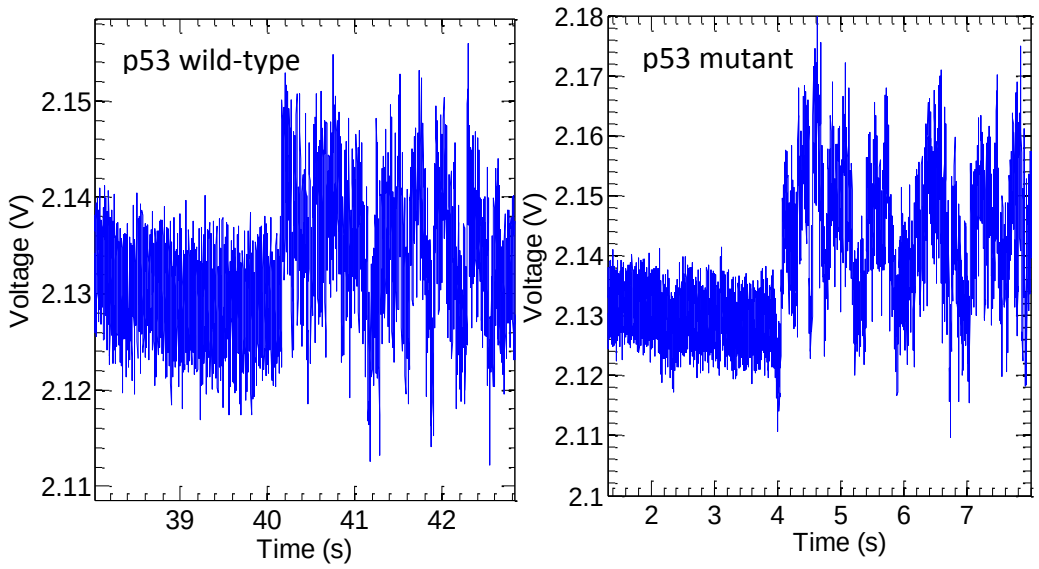

Figure 5.6 Typical optical trapping event of individual p53 protein for both wild-type and its mutant (Cys135Ser).

5.3 Discussion

The DNH tweezer shows the capability of being used as a research tool for better understanding of protein–DNA interactions (and other similarly sized molecules) in real time, at the single molecule level, in free-solution and in a label-free way. We have illustrated this in the present experiment, which shows the unzipping of DNA and also it's interaction with the transcription protein p53. DNH tweezers has the ability to understand the dynamics of small DNA fragments and distinguish the impact of a normal protein from its mutant on their behavior. This was shown as suppression of unzipping by

wild type p53 protein due to strong binding with the consensus hairpin DNA and we also evaluated the unzipping suppression energy based on Arrhenius behavior, which was found to be $\Delta U = 2 \times 10^{-20}$ J. The mutant (cys135ser) shows negligible impact on the unzipping of the DNA even though there is only partial loss in the binding activity, which may explain its ineffectiveness in suppression tumor development. This could provide aid to researchers in better understanding of the bio-molecular interactions useful in many drug discovery applications. For example, for the p53 case shown, the influence of small molecules that allow the mutant form to function normally would be of great interest.

Chapter 6. Mapping Low Frequency Vibrational Spectra of ssDNA

[4]

6.1 Introduction

DNA, the fundamental unit of life is one of the most interesting and widely studied biological molecules, in order to understand the basis of life. Most of these studies have explored the structural, mechanical and thermodynamic properties of DNA [103, 104] and can be broadly classified in terms of conformational flexibility and vibrational dynamics of the molecule. Optical tweezers have previously been used to determine the conformational flexibility of the DNA molecules at single molecules level using the force-extension principle or fluorescence resonance energy transfer (FRET) [105, 106]. Infrared spectroscopy [107], Raman spectroscopy [108,109], and absorption spectroscopy [110,111] have been used to establish vibrational dynamics of DNA for a wide range of frequencies ranging from the far infra-red to sub-millimeter. Absorption spectroscopy in the sub-millimeter range has been performed on dry DNA films to extract their vibrational resonances due to the high absorption of water that would swamp out the signal in the aqueous phase [111, 112]. However, these studies have been unable to show the lower frequency modes in the few tens of GHz range, in part due to the requirement of sufficiently thick films with large diameter and thus lack conclusive identification of

[4] The following chapter is adapted from: **Playing the notes of DNA with light: extremely high frequency nanomechanical oscillations**. Abhay Kotnala and Reuven Gordon. Accepted for publication by the Nanoscale in 2015. Copyright Permission Accepted.

the lower frequency modes [110]. Therefore the study of the very low frequency modes of DNA requires further investigation.

In this chapter, DNH optical tweezers were used to study the very low frequency modes of ssDNA in the sub-100 GHz range at the single molecule level. The low frequency vibrational spectrum was not measured directly as in absorption or scattering spectroscopy technique, but by special mapping of the intensity fluctuation caused due to the single molecule motion in the trap. The low frequency acoustic modes are the result of the collective motion of a large group of atoms in the ssDNA chain. These low frequency modes can provide information about the global dynamic properties of DNA such as the stretching rigidity [113]. The technique shown in this work also has the potential for use in DNA sequencing applications, if the resolution of the present system can be improved in order to detect changes in resonant frequency for a single base change, of a given DNA sequence. In addition, the technique is single molecule and label-free as compared to the existing methods used for DNA characterization like gel electrophoresis.

6.2 Theory

The dynamic behavior of the ssDNA is studied in terms of its collective vibrational modes in the tens of GHz range. Until present, this range of low frequency modes of ssDNA could not be observed in real systems due to the viscous effects of the medium. The existence of low frequency modes has been mentioned in the literature, but has lacked conclusive identification till present [114, 115]. Due to the high sensitivity of the

detected signal in the DNH tweezer system to the overall macromolecular motion, the DNH tweezer system makes it possible to observe these vibrational modes in a real system with aqueous media, at the single molecule level. The large amplitude of these low frequency vibrational modes which contribute to the overall motion of DNA is a key enabling feature of this work [116]. The vibrational resonance information is carried in the thermal fluctuations of the molecule in the trap and is associated with the local temperature of the molecule. The resonant vibrational mode is associated with larger overall motion of the DNA strand in the optical trap, which is detected by measuring the increase in the intensity fluctuations of the transmission signal through the aperture. This increase in the intensity fluctuations is observable as a peak in the root-mean squared (RMS) deviation of the optical transmission through the DNH when the excitation frequency matches the vibrational resonance frequency of the ssDNA, i.e. the increase in the noise amplitude of ssDNA motion due to resonant heating is measured. The low frequency vibrational modes closely relate to the dynamic properties such as bending and stretching rigidity of the DNA molecule [114].

6.2.1 Application of 1-D Lattice Vibration Theory to ssDNA

The resonant modes of ssDNA were calculated using simple one dimensional lattice vibration theory [117]. The theory considers the ssDNA as a linear chain of atoms with the atomic groups replaced by average mass, M, of the DNA base sequence that are connected by effective springs, with spring constant κ as shown in Figure 6.1. Since the

DNA sequences were approximately equally distributed among the bases, so using an average mass of the ssDNA for the bases is reasonable.

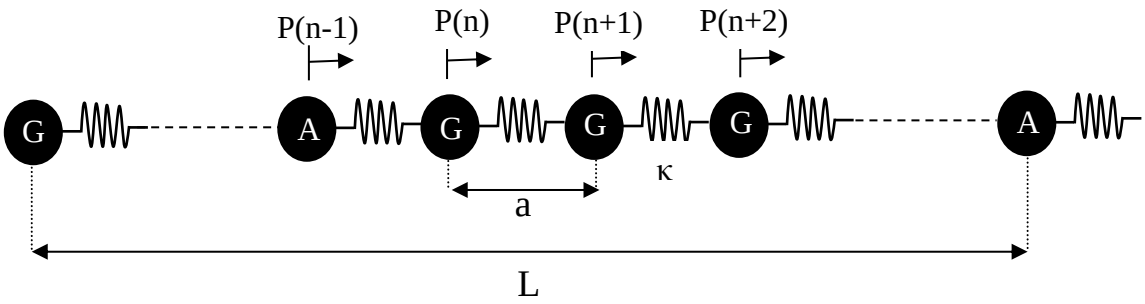

Figure 6.1 Model of ssDNA as a linear chain of atoms with mass M that are connected by effective springs with a spring constant κ. The mass is the average mass obtained from the total mass of ssDNA chain divided by the number of bases in the DNA strand. The distance between the bases is, a , and the length of the ssDNA is L.

For the case of low frequency modes, the approximation of small displacement of the bases in the direction parallel to the strand due to the electrostriction force is valid .The model defining the ssDNA in terms of mass and spring constant is necessary for harmonic approximation considering only nearest neighbour interaction.

The classical equation of motion of the ssDNA molecule (within the harmonic approximation) can be written as

$$M\ddot{P}_n = -\kappa(P_n - P_{n+1}) + \kappa(P_{n-1} - P_n) \qquad (6.1)$$

, where P_n is the displacement of the bases from the mean equilibrium position.

Assuming the displacement of the bases as a sinusoidally varying wave,

$$P_n = \frac{1}{\sqrt{M}} c e^{i(\beta a n - \omega t)} \qquad (6.2)$$

Equation 6.2 is the explicit solution for the displacement pattern in the linear DNA chain for any wave vector β.

Solving the equation of motion of ssDNA we get

$$\omega^2 M = \kappa(2 - e^{i\beta a} - e^{-i\beta a})$$

$$\omega = 2\sqrt{\frac{\kappa}{M}} \left| \sin\left(\frac{\beta a}{2}\right) \right| \qquad (6.3)$$

Different values of β correspond to independent vibrational modes of the ssDNA molecule.

For very small values of β, we can approximate $\sin\left(\frac{\beta a}{2}\right)$ in the equation 6.3 with the first term of the Taylor expansion ($\sin(x) = x$ for $x \to 0$) to:

$$\omega \approx \beta a \sqrt{\frac{\kappa}{M}} \qquad (6.4)$$

For very small values of β the phonons spread simply as vibration of the DNA molecule. For the resonance vibrational mode:

$$\beta = \frac{n\pi}{L}$$

Substituting the value of β in equation 6.4, we get the resonant vibrational frequency as:

$$\omega_r \approx \frac{\pi}{N_b}\sqrt{\frac{\kappa}{M}} \qquad (6.5)$$

where N_b is the number of bases in the ssDNA and κ is the spring constant or stretch modulus of the ssDNA molecule. The spring constant of the ssDNA is given as $\kappa = 123.5 k_B T/nm^2$, (where k_B is the Boltzmann constant and T is the temperature) which is the value of the stretch modulus of the sugar phosphate backbone of ssDNA molecule irrespective of the base sequence in the given approximation [117, 118]. This value of the stretch modulus was used to calculate the resonant frequency of the given ssDNA molecule. The value of the elastic stretch modulus is almost independent of the change in salt concentrations, which might be changed slightly during the experiment from their nominal value during resuspension in the buffer [119] and therefore should have little impact on the resonant frequency. The mass M is the average mass which is uniformly distributed along the ssDNA chain. It is obtained by dividing the total mass of the ssDNA (sum of mass of the individual bases A, T, G, and C in the specimen) by the total number of bases. It is reasonable to use an average, because the sequences were approximately equally distributed among the bases, using an average is reasonable. The numerical values of the average mass for all DNA sequences used in the experiments are given in section 6.3.

6.3 Experimental Set-up

The experimental set up used in this work was slightly modified compared to the previous ones. Since we want to excite the vibrational modes of the DNA molecule in addition to trapping, two lasers were used instead of a single laser used in the previous experimental set ups. The tweezer setup uses two slightly detuned lasers which are coupled together using a 50/50 coupler to form the trapping laser beam. The interference between the two slightly detuned laser beams produces an amplitude modulation of the electrostriction force due to the beating effect as shown in Figure 6.2. The laser beam with the beating effect is then launched into an inverted microscope system to trap and simultaneously excite the vibrational modes of the biomolecule as shown in Figure 6.3. The beat frequencies were measured using on optical spectrum analyzer (OSA) and were found to be stable within 0.4 GHz.

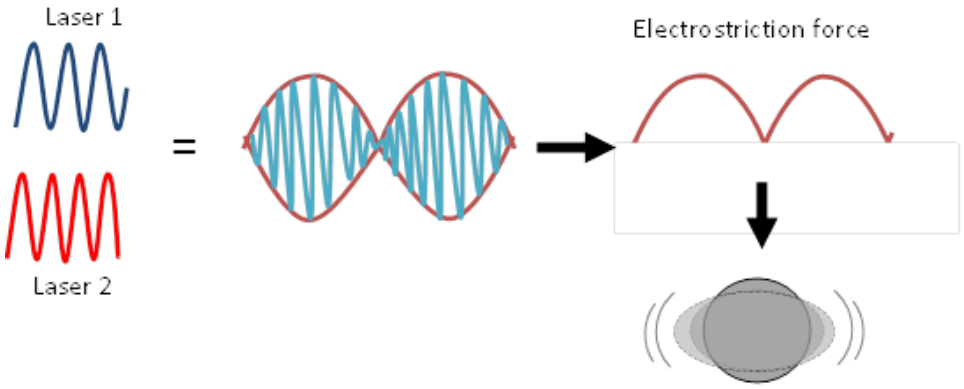

Figure 6.2 Slightly detuned lasers showing the beating laser signal leading to the modulation of the electrostriction force which excites the vibrational modes of the particle.

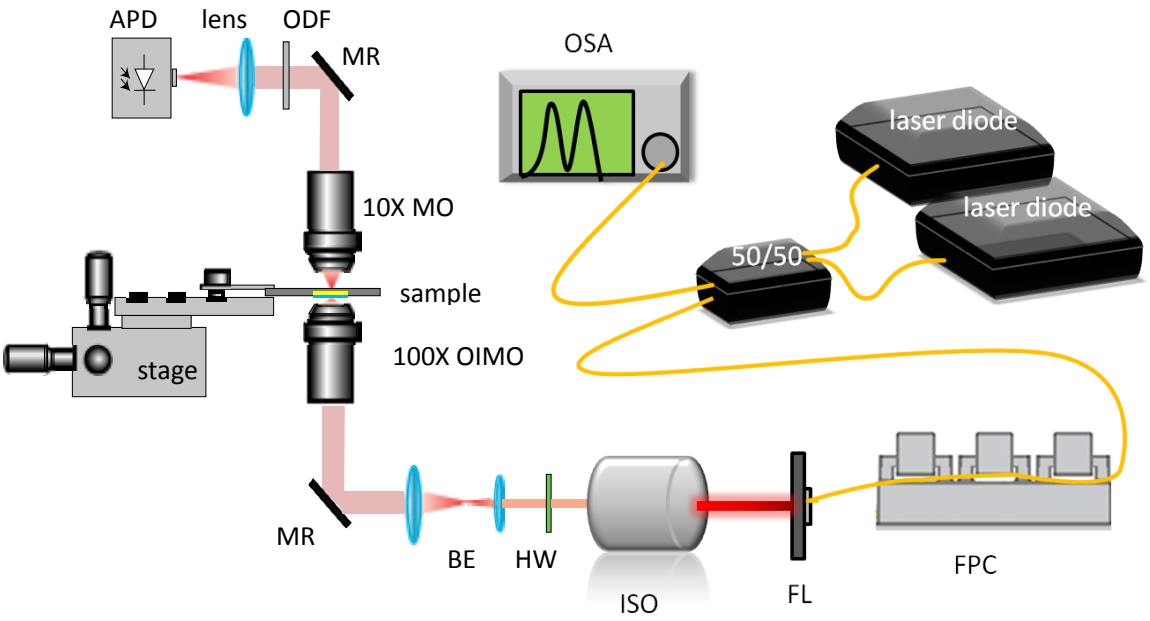

Figure 6.3 Double nanohole dual-laser optical tweezer setup. Abbreviations: optical spectrum analyzer (OSA), fiber coupler (50/50), fiber polarization controller (FPC), fiber launcher (FL), optical isolator (ISO), half wave plate (HWP), 45 degree mirror (MIR), dichroic reflector (DI), optical density filter (ODF), avalanche photodiode (APD), charged coupled device camera (CCD).

The trapping laser beam not only traps and holds the single ssDNA molecule but also excites the low frequency vibrational modes due to the beating effect. The change in the beating frequency results in the modulation of the electrostriction force. Electrostriction is a property of the dielectric material of particles by which they change their shape under the application of an electric field. It is caused by the slight displacement of ions in the DNA molecule under the application of an external electric field. Due to the high electronegativity of the DNA molecule, there is a slight displacement of positive ions in

the direction of the electric field and of negative ions opposite to the field. This displacement within the DNA molecule results in the overall elongation of the DNA strand. The resulting electrostriction force excites the low frequency vibrational modes in the ssDNA molecule. Electrostriction force is proportional to the optical trapping force in the DNH tweezer system. The low frequency vibrational modes appear as collective motions of the DNA strand resulting in an accordion-like motion or stretching of the ssDNA.

Once the ssDNA molecule is trapped, which can be observed as a step change in the APD voltage signal on an oscilloscope, the transmission signal data is acquired for different beat frequencies. The change in the beat frequencies can be obtained by keeping the wavelength of one laser fixed, while changing the wavelength of the other laser. This can be achieved either by using a tunable laser or temperature tuning. Temperature tuning was used in this experiment to generate beat frequencies in the range of 10-100 GHz, which was the range of interest for ssDNA modes. The acquired transmission signal was then used to calculate the normalized RMS deviation as a function of beat frequency. The beat frequency corresponding to the maximum value of RMS deviation of transmission signal corresponds to the resonant vibrational frequency of the ssDNA.

The resonant excitation of the vibrational modes results in an increase in the localized temperature of the DNA molecule, which causes increased thermal fluctuations of the DNA molecule in the trap. This is observed as an increase in the transmission signal intensity fluctuation through the DNH aperture, which is highly sensitive to the motion of the molecule in the trap. Thus the vibrational resonance contained in the increased

thermal fluctuation is mapped to the transmission signal, which can then be examined by observing the RMS deviation of the signal as a function of the scanned beat frequencies during the experiment to obtain the low frequency vibration spectrum of the trapped particle.

6.4 Experiment and Results

A 20 base ssDNA sequence, 5-AGG CATGCC TAG GCA TGC CT-3, was trapped using a modified DNH tweezer set up. The trapping of ssDNA is seen as a step change in the transmission signal through the DNH aperture as has been shown in the previous chapters [7]. The increase in fluctuations of the transmission signal is due to the thermal motion of the particle in the trap. After the ssDNA is trapped the transmission signal is recorded for different beat frequencies in the frequency range of interest i.e. 10-100 GHz with step size of 0.4 GHz. The transmission signal was recorded for 10 seconds for each beat frequency at a rate of 1 KHz. Figure 6.4a shows the trapped transmission signal for two different ranges of beat frequencies, 13-15 GHz (blue, non –resonant) and 38.5-40.5 GHz (red, resonant). The histogram on the right of Figure 6.4a shows the corresponding transmission signal with a Gaussian fit. We observe that there is an increase in the fluctuation of the transmission signal at resonance, which is also evident from a 46.6 % increase in the width of the Gaussian fit at resonant beat frequency compared to non-resonant beat frequencies. The width of the Gaussian signal is equivalent to the RMS deviation of the transmission signal, which is further plotted as function of different beat frequencies to give the vibrational spectrum of the trapped molecule. Figure 6.4b shows

the normalized RMSD spectrum of the 20 base ssDNA molecules in the range of 10-60 GHz. The peak in the RMSD at around 40 GHz corresponds to the resonant vibrational mode of the 20 base ssDNA. The resonant peak in the spectrum was observed for multiple trapping events, with variation of 1 GHz around the mean value. The higher frequency modes were also observed by extending the range of the beat frequencies in the experiment. Second-order harmonic resonances of ssDNA were observed for 20 base and 30 base ssDNA as shown in Figure 6.5. We see the presence of second harmonic vibrational mode at approximately twice the fundamental resonant frequency of the DNA strand. The second harmonic resonant mode occurs at around f=57.6 GHz for 30 base ssDNA and f= 73GHz as shown in Figure 6.5.

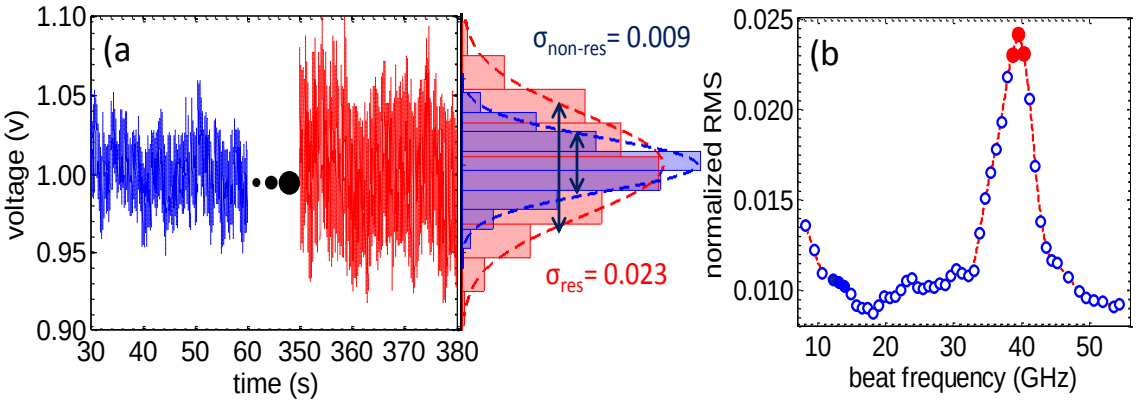

Figure 6.4 (a) Intensity fluctuations and corresponding Gaussian fit of the transmission signal through the DNH aperture for a trapped 20 base ssDNA. The transmission signal 30-60 sec (blue) corresponds to the non–resonant beat frequency points in the frequency range, f=13-15 GHz (solid, blue) and the transmission signal 350-380 sec (red) correspond to the near–resonant beat frequency points from 38.5-40.5 GHz as shown in figure 6.4b (solid, red) (b) Normalized RMSD as a function of scanned beat frequencies showing resonance at 40 GHz.

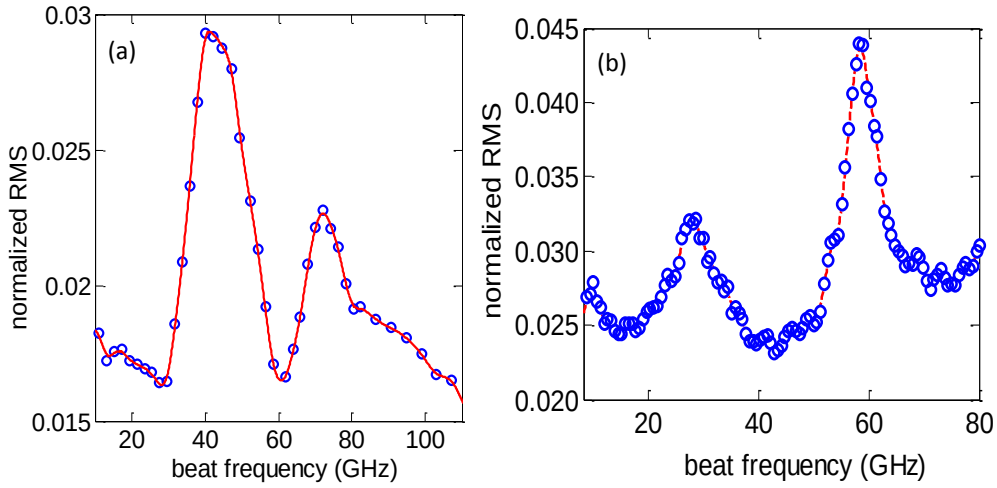

Figure 6.5 Normalized root mean squared (RMS) deviation of the scattered transmission signal for (a) 20 base ssDNA showing the fundamental resonant frequency at f=39 GHz and a second order harmonic at f=73 GHz. (b) 30 base ssDNA showing the fundamental resonant frequency at f=28.3 GHz and a second order harmonic at f=58GHz.

6.5 Impact of Size and Sequence of ssDNA on the Vibrational Spectrum

The impact of the physical parameters; length (number of bases) and sequence (mass of DNA) on the vibrational spectrum of the ssDNA molecule were also studied. The measurements were repeated for different length of ssDNA ranging from 20 to 40 bases. We observe a decrease in the resonant vibrational frequency with the change in number of bases from 20 to 40 as shown in Figure 6.6. This was found to be in good agreement with the resonant frequency calculated using the 1-D lattice vibration theory as discussed in Section 6.2.1. Table 6.1 shows the different length DNA sequences used in the above experiment.

Table 6.1 Different length sequences of ssDNA used for trapping and measurement of the corresponding vibrational spectrum. The total mass (m) of the ssDNA is the sum of mass of individual bases A, T, G, C in the specimen and M is the average mass obtained by dividing the total mass (m) by the total number of bases (N_b) for the given ssDNA.

S.No.	Sequence	Average mass (M) (in Da)
1	5′-AGG CAT GCC TAG GCA TGC CT-3′	129.93
2	5′-GGG CGG GGA GGG GGA AGG GAG AGG G-3′	145.34
3	5′-GGG CGG GGA GGG GGA AGG GAG AGG GAA GAG-3′	144.54
4	5′-GGG CGG GGA GGG GGA AGG GAG AGG GAA GAG AGG GA-3′	144.43
5	5′-GGG CGG GGA GGG GGA AGG GAG AGG GAA GAG AGG GAG GGG G-3′	145.14

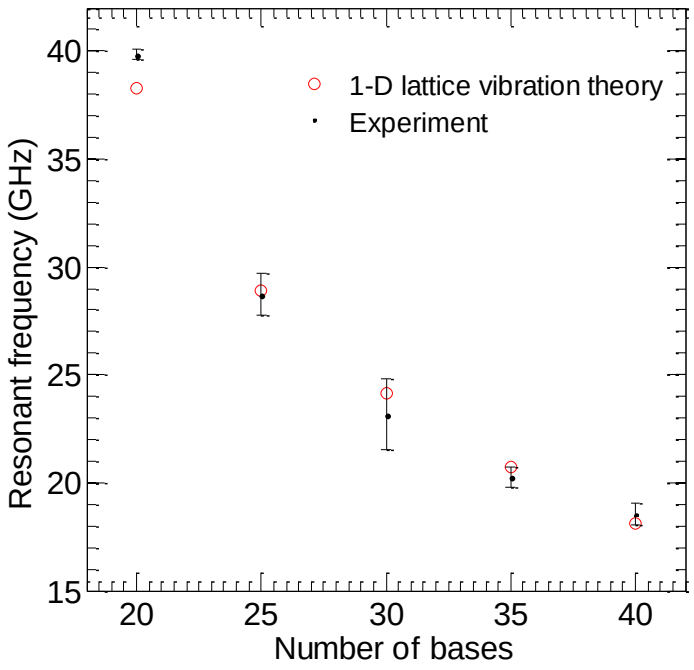

Figure 6.6 Resonant mode frequency as a function of number of bases of ssDNA molecule. The line (black) shows the mean resonant frequency along with the standard deviation found

experimentally. The circles (red) are the resonant frequency calculated by modelling ssDNA using 1-D lattice vibration theory.

This shows the ability of the experiment to characterize DNA of different length with resolution down to small number of bases. The experiment was also repeated for different sequences of ssDNA of the same length of 30 bases. Table 6.2 shows three different sequences of 30 base ssDNA used in the experiments.

Table 6.2 Different sequences of 30 base ssDNA used for trapping and measurement of the corresponding vibrational spectrum. The total mass (m) of the ssDNA is the sum of mass of individual bases A, T, G, C in the specimen and M is the average mass obtained by dividing total mass with number of bases for a single strand of DNA.

S.No.	Sequence	Total mass	Average mass (M) (in Da)
1	5′-GGGCGGGGAGGGGGAAGGGAGAGGGAAGA-3′	4336.2 Da	144.54
2	5′-CAGCACACACACGGAAGGGAGACACAACAC-3′	3895.9 Da	129.86
3	5′-CCCGCCCCTCCCCCTTCCCTCTCCCTTCTC-3′	3463.4 Da	115.44

The change in sequence corresponds to a change in the total mass of the DNA molecule and therefore results in a change in the resonant vibrational frequency of the molecule as shown in Figure 6.7. Due to the limitation in resolution of the present system, we could demonstrate the change in the resonance frequency for different sequences with a mass difference of hundreds of Daltons, but with improvement in accuracy and sensitivity of the setup; it might be possible to sense a single base change in the ssDNA molecule of similar lengths. The resonant mode frequencies calculated for all the ssDNA sequences

by modelling the ssDNA using a 1-D lattice vibration theory were found to be consistent with the experimental results as shown in Figure 6.7.

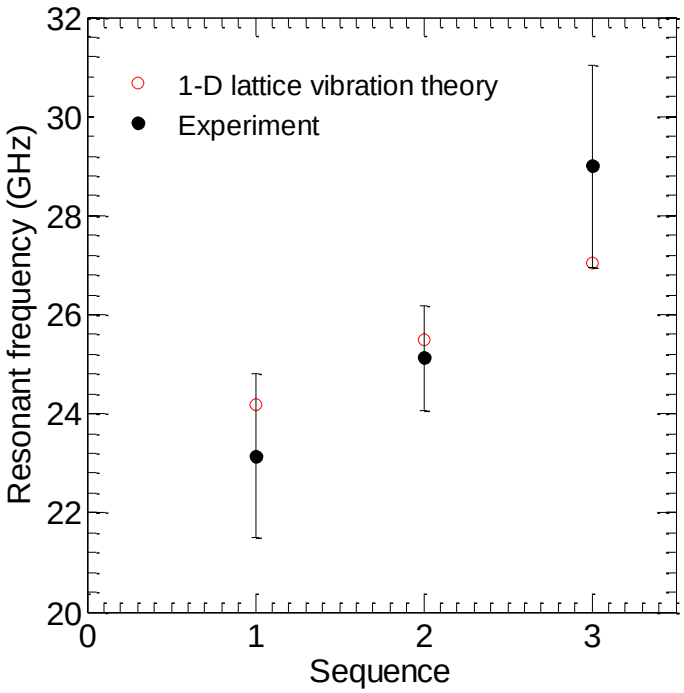

Figure 6.7 Resonant frequencies of three different sequences of 30 base ssDNA molecules (Seq. 1: MW 4336.2 Da, Seq. 2: MW 3895.9 Da, Seq. 3: MW 3463.4 Da). The solid circles (black) shows the mean resonant frequency along with the standard deviation found experimentally. The circles (red) are the resonant frequency calculated by modelling ssDNA using the 1-D lattice vibration theory.

6.6 Discussion

The DNH tweezer with a beating laser system shows the capability as a single molecule tool, to trap ssDNA molecule and obtain its vibrational spectrum in the sub-100 GHz range. Further experiments based on this approach could be done to study the influence

of other external factors and small molecule on the vibration dynamics of the ssDNA and are proposed as future work The technique could also be used in applications related to biosensing and characterization of DNA molecules by further improving the sensitivity of the technique to detect single base change. It would also be interesting to extend the experiments to higher frequencies so as to excite and detect the localized modes between individual bases. Also the study of intercalation of the drugs in the DNA which is an important phenomenon for making anti-cancer drugs can be studied using this technique [120]. The intercalation of drugs in the DNA might significantly changes the vibrational dynamics of the DNA molecule and hence can be used as a tool to investigate the intercalation process.

Chapter 7. Conclusion and Outlook

7.1 Conclusion of Thesis

In this thesis, I have developed new techniques using the DNH optical tweezers, with the aim of better understanding the DNH tweezers and exploring its capabilities for applications in nanoparticle and single molecule analysis. The first major step in this regard was the calculation of trapping efficiency and stiffness (κ) of the DNH tweezers for small Rayleigh nanoparticles in the range of 1-100 nm. Two approaches: autocorrelation of the Brownian-induced intensity fluctuations and the time response method were used to determine the stiffness which gave a quantitative insight of the large trap stiffness of the DNH tweezer as compared to the conventional tweezers for Rayleigh particles in this range. This technique for calculating the trap stiffness was for the first time applied to particles in the Rayleigh domain and calculated from the experimental data as opposed to the theoretical and numerical calculations found in the literature. The ability of the DNH tweezers to act as a sensor to determine the concentration, size and refractive index of the trapped particles was also explored. This was based on the statistical analysis of the time-to-trap (t_t) parameter for different nanoparticle solution. The time-to-trap shows a linear dependence with nanosphere size and a -2/3 power dependence with nanosphere concentration, which was found to be in agreement with simple diffusion theory based on simple microfluidic conditions. By repeating the trapping measurements on spherical particles of same sizes but different refractive

indexes, it was also found that the percentage change in the optical transmission signal at the trapping instant scales with the refractive index of the particle in accordance with the Clausius–Mossotti factor. The large trap stiffness of DNH tweezer along with high temporal resolution made it possible to trap nanoparticles freely without attaching them to larger spherical particles and also in a label free manner. These features provide an opportunity to study biomolecules like proteins, DNA and their interaction in a free-solution and label-free way rather than using tethers and labels. Using this technique, we were able to show the unzipping of the hairpin DNA structure using strong optical forces due to the strongly polarized field at the DNH aperture. In addition, the interaction of the DNA with a transcription protein p53 was also studied using DNH tweezer which showed the binding of the p53 protein to the DNA which suppresses the unzipping phenomenon. The mutant form of the protein could not show this characteristic. Thus DNH tweezers showed the ability to understand the dynamics of small DNA fragments and the capability to distinguish the impact of a normal protein from its mutant on their behaviour. In order to further explore the dynamics of the small DNA molecules using DNH tweezers, we also excited and detected the low frequency vibrational modes of ssDNA. The importance of this technique is to identify the Raman-active low frequency acoustic modes of biomolecules at a single molecule level, which have been difficult to study using conventional spectroscopy techniques available from the past.

7.2 Future Work

The research contributions made in this thesis opens up new directions for furthering the applications of DNH tweezer in diverse fields and also makes it a full-fledged tool for single molecule analysis. There are many experiments that can be performed which would establish the versatility of the DNH tweezer system as a single molecule analysis tool. In this section, I discuss some of these experiments that can be performed and taken forward as future research in the field of nanoaperture tweezers.

7.2.1 Intercalation of DNA

Intercalation is the insertion of small molecules between the bases of DNA. The process of intercalation occurs when molecules also known as ligands, of certain specific size and chemical nature interact with DNA, such that they fit in between the base pair of DNA. They are mostly polycyclic, aromatic and planar such as berberine, ethidium bromide and other. The DNA intercalators are used in chemotherapeutic treatment to inhibit the replication process of DNA in growing cancerous cell. Since the ligands used for the intercalation process change the structure and add mass to the DNA strand, it would be interesting to see the change in the vibrational modes of the DNA as they are dependent on the size and mass of the DNA. This would be effective in measuring the effectiveness of the ligand as the intercalator and also quantify the intercalation process.

7.2.2 Conformational Dynamics using Intensity Modulation of Trapping Laser

We believe that DNH tweezer can also be used to understand the conformational behaviour and macroscopic dynamics of different biomolecules like proteins in various biological environments and also the impact of ligands, binding agents on their structural configuration and biological properties. This can be done using intensity modulated laser beam for trapping, so that it is in resonance with the specific conformational modes of the biomolecule and can be distinguished by a statistical analysis of the transmission signal during resonances. This would give further insight into the structural configuration of protein structure and its modification by the binding agents which could be useful in drug discovery applications.

7.2.3 Compact Lab-on-chip Tweezer

The DNH tweezer system in its current form is a bulky and not a hand-held device. One of the future works could be to downscale the system such that it can be hand-held and integrated with microfluidic environment for easy to use. The integration of DNH tweezer into a chip will make it useful for many clinical applications. This can be done by using the fiber optics based technology where the nanoaperture could be fabricated at the facet of the optical fiber and combined with a microfluidic chip consisting of the flow channels. The device would be compact and the user would just need to attach the laser and detector and insert the desire testing solution for using the device. Therefore it could be used easily without alignments and transportation problems. Fiber optic is robust, compact, modular and inexpensive, operates at a wide variety of different wavelengths, and can withstand high temperature and humidity. The fibre based approach would also

open up many new opportunities for in situ biological sensing within cells and 3-D manipulation of the trapped particle. One of the experiments would be to use the DNH aperture to isolate a single virus molecule from a solution and translate it to a new sample to infect a single cell. This would enable the study of virus infection at the single particle level. Some initial work has already been done on this, where the DNH was fabricated at the tip of the cleaved fiber. A gold layer of 100 nm thickness was evaporated on the tip of the fiber and thereafter milled using FIB to make the DNH structure. 20 nm polystyrene nanoparticles were trapped using this configuration as shown in Figure 7.1.

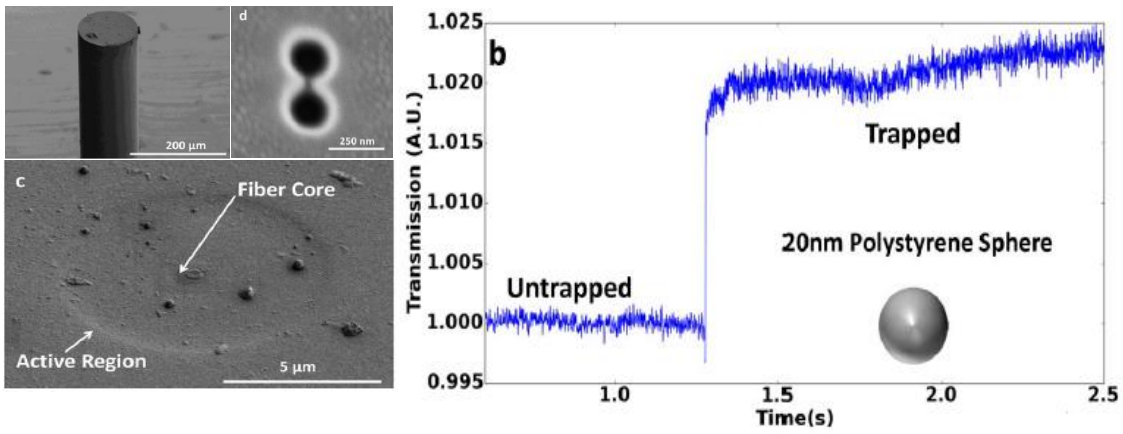

Figure 7.1 (Left) Tilted SEM image of the optical fiber with gold on the tip of the cleaved end and the SEM image of the DNH milled into the active region of the fiber. (Right) Trapping event for a 20 nm polystyrene sphere in a DNH on the cleaved end of a fiber.

7.2.4 Integration with Other Single Molecule Techniques

The DNH tweezer in this work uses only the transmission signal scattered by the presence of the particle to determine the dynamics and other properties of the trapped

molecule. The DNH tweezer also can be extended to do fluorescent measurements and measurement of Raman scattering from the molecules. This would allow the DNH tweezer to trap, identify and understand dynamics using different approaches on a single platform. It would be applicable in the field of particle sorting or particle identification in heterogeneous solutions. This would also allow the DNH tweezer to extend the range of applications in the field of biophysics and biochemistry, which require these additional single molecule techniques to provide more information about various processes.

Bibliography

1. J. C. Maxwell. A dynamical theory of the electromagnetic field. *Philosophical Transactions of the Royal Society of London,* 155, 459–512, 1865.
2. J. C. Maxwell. A treatise on electricity and magnetism (in two volumes). *Clarendon Press*, Oxford, 1873.
3. A. Ashkin. Acceleration and trapping of particles by radiation pressure. *Physics Review Letters*, 24, 156–159, 1970.
4. A. Ashkin and J. M. Dziedzic. Optical levitation by radiation pressure. *Applied Physics Letters*, 19, 283–285, 1971.
5. A. Ashkin and J. M. Dziedzic. Optical levitation of liquid drops by radiation pressure, *Science*, 187, 1073–1075, 1975.
6. A. Ashkin, J. M. Dziedzic, J. E. Bjorkholm, and S.Chu. Observation of a single-beam gradient force optical trap for dielectric particles. *Optics Letters*, 11, 288–290, 1986.
7. K. C. Neuman and S. M. Block. Optical trapping. *Review of Scientific Instruments*, 75**,** 2787-2809, 2004.
8. D. G. Grier. A revolution in optical manipulation. *Nature,* 424, 810-816, 2003.
9. A. Ashkin and J. M. Dziedzic. Optical trapping and manipulation of viruses and bacteria. *Science,* **235**, 1517–1520, 1987.
10. A. Ashkin, J. M. Dziedzic, and T. Yamane. Optical trapping and Manipulation of Single Cells Using Infrared Laser Beams. *Nature,* 330, p. 769, 1987.

11. K. Svoboda, C. F. Schmidt, D. Branton, and S. M. Block. Conformation and elasticity of the isolated red blood cell membrane skeleton. *Biophysical Journal*, 63, p. 784, 1992.

12. P. J. H. Bronkhorst, G. J. Streekstra, J. Grimbergen, E. J. Nijhof, J. J. Sixma, and G. J. Brakenhoff. A new method to study shape recovery of red blood cells using multiple optical trapping. *Biophysical Journal*, 69, p. 1666-1673, 1995.

13. R. Huber, S. Burggraf, T. Mayer, S. M. Barns, P. Rossnagel, and K. O. Stetter. Isolation of a hyperthermophilic archaeum predicted by in situ RNA analysis. *Nature*, 376, p. 57, 1995.

14. K. Svoboda, P. P. Mitra and S. M. Block. Fluctuation analysis of motor protein movement and single enzyme-kinetics. *Proceedings of the National Academy of Sciences,* 91**,** 11782–11786, 1994.

15. J. C. Crocker and D. G. Grier. When like charges attract: the effects of geometrical confinement on long-range colloidal interactions. *Physics Review Letters*, 77, pp-1897, 1996.

16. C. A. Murray. When like charges attract. *Nature*, 385, p. 203, 1997.

17. C. Bustamante, S. B. Smith, J. Liphardt and D. Smith. Single-molecule studies of DNA mechanics. *Current Opinion in Structural Biology*, 10**,** 279–285, 2000.

18. T.T. Perkins, S.R. Quake, D.E. Smith, S. Chu. Relaxation of a Single DNA Molecule Observed by Optical Microscopy. Science, 264, 822–26, 1994.

19. N. Handa, P.R. Bianco, R.J. Baskin and S.C. Kowalczykowski. Direct visualization of RecBCD movement reveals cotranslocation of the RecD motor after chi recognition. *Molecular Cell*, 17, 745–50, 2005.

20. P.R. Bianco, L.R. Brewer, M. Corzett, R. Balhorn, Y. Yeh, et al. *Nature*, 409, 374–78, 2001.

21. J. Mameren, M. Modesti, R. Kanaar, C. Wyman, G.J Wuite, E.J. Peterman. Dissecting elastic heterogeneity along DNA molecules coated partly with Rad51 using concurrent fluorescence microscopy and optical tweezers. *Biophysical Journal*, 91, 78–80, 2006.

22. R. D. Snook, T.J. Harvey, E.C. Faria and P. Gardner. Raman Tweezer and their application to the study of single trapped eukaryotic cells. Integrative Biology, 1, 43-52, 2009.

23. T. A. Nieminen, S. Parkin, T. Asavei, V. L. Y. Loke, N. R. Heckenberg, and H. Rubinsztein-Dunlop. Chapter 8 - Optical Vortex Trapping and the Dynamics of Particle Rotation in *Structured Light and Its Applications*, D. L. Andrews, ed. *Academic Press*, 195-236, 2008 .

24. G. Nienhuis. Chapter 2 - Angular Momentum and Vortices in Optics in *Structured Light and Its Applications*, D. L. Andrews, ed. *Academic Press*, 19-62, 2008.

25. M. Padgett and J. Leach. Chapter 9 - Rotation of Particles in Optical Tweezers in *Structured Light and Its Applications*. D. L. Andrews, ed. *Academic Press*, 237-248, 2008.

26. I. Heller, T. P. Hoekstra, G. A. King, E. J. G. Peterman, and G. J. L. Wuite. Optical tweezers analysis of DNA-Protein Complexes. *Chemical Review*, 2014.

27. M. Hegner, D. Bruggemann, and D. Skoko. Optical Tweezers in B. Bhushan, ed. *Springer Netherlands*, 1981-1991, 2012.

28. S. B. Smith, Y. Cui, C. Bustamante. Overstretching B-DNA: The elastic response of individual double-stranded and single-stranded DNA molecules. *Science*, 271, 795-799, 1996.

29. J. Van Mameren, M. Modesti, R. Kanaar, C. Wyman, E. J. G. Peterman, G. J. L. Wuite. Counting RAD51 proteins disassembling from nucleoprotein filaments under tension. *Nature*, 457, 745-748, 2009.

30. M. D. Wang, M. J. Schnitzer, H. Yin, R. Landick, J. Gelles, S. M. Block. Force and velocity measured for single molecules of RNA polymerase. *Science*, 282, 902-907, 1998.

31. G. Sirinakis, Y. Ren, Y. Gao, Z. Xi, Y. Zhang. Combined versatile high-resolution optical tweezers and single-molecule fluorescence microscopy. *Review of Scientific Instruments*, 83, 093708, 2012.

32. I. Heller, G. Sitters, O. D. Broekmans, G. Farge, C. Menges, W. Wende, S. W. Hell, E. J. G. Peterman, G. J. L. Wuite. STED nanoscopy combined with optical tweezers reveals protein dynamics on densely covered DNA. *Nature Methods*, 10, 910-916, 2013.

33. T. A. Nieminen, G. Knöner, N. R. Heckenberg, H. Rubinsztein Dunlop. Physics of Optical Tweezers. *Laser manipulation of cells and tissues*, 82, 207-236, 2007.

34. J. E. Molloy and M. J. Padgett. Lights, action: Optical tweezers. *Contemporary Physics*, 43, 241-258, 2002.

35. Bryant, Z., et al. Structural transitions and elasticity from torque measurements on DNA. *Nature*, 424, 338-341, 2003.

36. J. M. Vigoureux and D. Courjon. Detection of nonradiative fields in the light of the Heisenberg uncertainty. *Applied Optics*, 31,3170-77, 1992.

37. L. Novotny, R. X. Bian, & X. S. Xie. Theory of nanometric optical tweezers. *Physical Review Letters*, 79, 645–648, 1997.

38. K. Okamoto and S. Kawata. Radiation force exerted on subwavelength particles near a nanoaperture. *Physical Review Letters*, 83, 4534–4537,1999.

39. M. Righini, G. Volpe, C. Girard, D. Petrov and R. Quidant. Surface plasmon optical tweezers: tunable optical manipulation in the femtonewton range. *Physical Review Letters*, 100, 183604, 2008.

40. M. Righini, A. S. Zelenina, C. Girard and R. Quidant. Parallel and selective trapping in a patterned plasmonic landscape. *Nature Physics*, 3, 477–480, 2007.

41. P. Mühlschlegel, H. J. Eisler, O. J. F. Martin, B. Hecht and D. W. Pohl. Resonant optical antennas. *Science*, 308, 1607–1609, 2006.

42. A. N. Grigorenko, N. W. Roberts, M. R. Dickinson and Y. Zhang. Nanometric optical tweezers based on nanostructured substrates. *Nature Photonics*, 2, 365–370, 2008.

43. A. E. Cetin, C. Yilmaz, A. A. Yanik, S. Somu, A. Busnaina, and H. Altug. Optical trapping and manipulation with plasmonic nanopillar antennas for enhanced biosensing. *Frontiers in Optics 2011/Laser Science XXVII, OSA Technical Digest*, paper FTuS4, 2011.

44. B. J. Roxworthy, K. D. Ko, A. Kumar, K. H. Fung, E. K. C. Chow, G. L. Liu, N. X. Fang, and K. C. Toussaint. Application of plasmonic bowtie nanoantenna arrays for optical trapping, stacking, and sorting. *Nano Letters*, 12**,** 796-801, 2012.

45. S. Lin, E. Schonbrun, and K. Crozier. Optical manipulation with planar silicon microring resonators. *Nano Letters*, 10, 2408–2411, 2010.

46. A. H. J. Yang, S. D.Moore, B. S. Schmidt, M. Klug, M. Lipson, and D. Erickson. Optical manipulation of nanoparticles and biomolecules in sub-wavelength slot waveguides. *Nature*, 457, 71–75, 2009.

47. W. Tsai, J. Huang, and C. Huang. Selective trapping or rotation of isotropic dielectric microparticles by optical near field in a plasmonic Archimedes spiral. *Nano Letters*, 14**,** 547-552, 2014.

48. M. Righini, G. Volpe, C. Girard, D. Petrov and R. Quidant. Surface plasmon optical tweezers: tunable optical manipulation in the femtonewton range. *Physical Review Letters*, 100**,** 183604, 2008.

49. Y. Tanaka, S. Kaneda, and K. Sasaki. Nanostructured potential of optical trapping using a plasmonic nanoblock pair. *Nano Letters*, 13**,** 2146-2150, 2013.

50. H. Xin, R. Xu and B. Li. Optical trapping, driving, and arrangement of particles using a tapered fibre probe. *Scientific Reports*, 2, 818, 2012.

51. T. Shoji and Y. Tsuboi. Plasmonic optical tweezers toward molecular manipulation: Tailoring plasmonic nanostructure, light source, and resonant trapping. *Journal of Physical Chemistry Letters*, 5**,** 2957-2967, 2014.

52. Fang, Z. et al. Evolution of light-induced vapor generation at a liquid immersed metallic nanoparticle. *Nano Letters*, 13, 1736–1742, 2013.

53. K. Wang, E. Schonbrun, P. Steinvurzel, and K. B. Crozier. Trapping and rotating nanoparticles using a plasmonic nano-tweezer with an integrated heat sink. *Nature Communications*, 2**,** 469, 2011.

54. D.G. Jay. Selective destruction of protein function by chromophore-assisted laser inactivation. *Proceedings of the National Academy of Sciences*.85.15,5454-5458, 1988.

55. T. Li, S. Kheifets, D. Medellin and M. G. Raizen. Measurement of the instantaneous velocity of a Brownian particle. *Science,* 324**,** 1673–1675, 2010.

56. R. M. Simmons, J. T. Finer, S. Chu and J. A. Spudich. Quantitative measurements of force and displacement using an optical trap. *Biophysical Journal*, 70**,** 1813–1822, 1996.

57. A. Ashkin and J. M. Dziedzic. Feedback stabilization of optically levitated particles. *Applied Physics Letters,* 30**,** 202–204, 1977.

58. J. D. Jackson. Classical Electrodynamics. *Wiley,* New York, 1998.

59. Kwak, E. S. *et al.* Optical trapping with integrated near-field apertures. *Journal of Physical Chemistry B,* 108, 13607–13612, 2004.

60. A. Baev, E.P. Furlani, P.N. Prasad, A.N. Grigorenko and N.W. Roberts. Laser nanotrapping and manipulation of nanoscale objects using subwavelength apertured plasmonic media. *Journal of Applied Physics*, 103**,** 084316, 2008.

61. L. A. Blanco and M. Nieto-Vesperinas. Optical forces near subwavelength apertures in metal discs. *Journal of Optics A*, 9**,** 235–8, 2007.

62. M. L. Juan, R. Gordon, Y. Pang, F. Eftekhari, and R. Quidant. Self-induced back-action optical trapping of dielectric nanoparticles. *Nature Physics*, 5**,** 915-919, 2009.

63. S. H. Mirsadeghi and J. F. Young. Ultrasensitive diagnostic analysis of au nanoparticles optically trapped in silicon photonic circuits at sub-milliwatt powers. *Nano Letters*, 14, 5004-5009, 2014.

64. C. Chen, M. L. Juan, Y. Li, G. Maes, G. Borghs, P. Van Dorpe, and R. Quidant. Enhanced optical trapping and arrangement of nano-objects in a plasmonic nanocavity. *Nano Letters*, 12**,** 125-132, 2012.

65. A. Kotnala and R. Gordon. Double nanohole optical tweezers visualize protein p53 suppressing unzipping of single DNA-hairpins. *Biomedical Optics Express*, 5**,** 1886-1894 2014.

66. J. Berthelot, S. S. Acimovic, M. L. Juan, M. P. Kreuzer, J. Renger, and R. Quidant. Three-dimensional manipulation with scanning near-field optical nanotweezers. *Nature Nanotechnology*, 9**,** 295-299, 2014.

67. A. A. E. Saleh and J. A. Dionne. Toward efficient optical trapping of sub-10-nm particles with coaxial plasmonic apertures. *Nano Letters*, 12**,** 5581-5586, 2012.

68. Y. Pang and R. Gordon. Optical Trapping of a Single Protein. *Nano Letters*, 12**,** 402-406 2012.

69. A. Zehtabi-Oskuie, H. Jiang, B. R. Cyr, D. W. Rennehan, A. Al-Balushi, and R. Gordon. Double nanohole optical trapping: dynamics and protein-antibody co-trapping. *Lab on a Chip*, 13**,** 2563-2568, 2013.

70. N. Vogel, J. Zieleniecki, and I. Koper. As flat as it gets: ultrasmooth surfaces from template-stripping procedures. *Nanoscale*, 4**,** 3820-3832, 2012.

71. P. N. Melentiev, A. E. Afanasiev, A. A. Kuzin, A. S. Baturin, V. I. Balykin. *Optics Express*, 21, 13896−13905, 2013.

72. M. Honda, Y. Saito, N. I. Smith, K. Fujita, and S. Kawata. Nanoscale heating of laser irradiated single gold nanoparticles in liquid, *Optics Express*, 19, 12375-12383, 2011.

73. K. Neuman and S. Block. Optical trapping. *Review of Scientific Instruments*, 75, 2787–2809, 2004.

74. W. Brenig. Brownian motion: Langevin equation. *Springer Berlin Heidelberg*, pp. 69-72, 1989.

75. F. Reif. Fundamentals of statistical and thermal physics. *McGraw-Hill: New York*, 1965.

76. J. Happel and H. Brenner. Low reynolds number hydrodynamics. *Prentice-Hall Inc., New Jersey*, 1965.

77. Y. Pang and R. Gordon. Optical trapping of 12 nm dielectric spheres using double-nanoholes in a gold film. *Nano Letters*, 11**,** 3763-3767, 2011.

78. A. Rohrbach. *Physical Review Letters*, 95, 168102, 2005.

79. M. Shindel, J. Swan, and E. Furst. Calibration of an optical tweezer microrheometer by sequential impulse response. *Rheologica Acta*, 52**,** 455-465, 2013.

80. H.Kress. Cell mechanics during phagocytosis studied by optical tweezers-based microscopy. *Cuvillier Verlag: Göttingen*, 2006.

81. G. E. P. Box, G. M. Jenkins. Time Series Analysis: Forecasting and Control. *Holden-Day: San Francisco*, 1976.

82. A.H.J. Yang, T. Lerdsuchatawanich and D. Erickson, *Nano Letters*, 9, 1182−1188, 2009.

83. J. C. Crocker and D. G. Grier. Microscopic measurement of the pair interaction potential of charge-stabilized colloid. *Physical Review Letters*, 73, 352–355, 1994.

84. D.G. Grier. Optical tweezers in colloid and interface science. *Current Opinion in Colloid & Interface Science*, 2, 264, 1997.

85. J. C. Crocker and D. G. Grier. When like charges attract: The effects of geometrical confinement on long-range colloidal interactions. *Physical Review Letters*, 77, 1897–1900, 1996.

86. G. Volpe and G. Volpe. Simulation of a Brownian particle in an optical trap. *Americal Journal of Physics*, 81, 224-230, 2013.

87. G. M. Wang, E. M. Sevick, E. Mittag, D. J. Searles and D. J. Evans. Experimental demonstration of violations of the second law of thermodynamics for small systems and short time scales. *Physical Review Letters*, 89, 050601, 2002.

88. G. K. Batchelor, An introduction to fluid dynamics. *Cambridge U. P.*, 1973.

89. K. Pearson. The Problem of the random walk. *Nature*, 72, 318–342, 1905.

90. , H. C. Van de Hulst. Light scattering by small particles. *Wiley: NewYork*, 1957.

91. T. M. Squires, R. J. Messinger and S. R. Manalis. Making it stick: convection, reaction and diffusion in surface-based biosensors. *Nature Biotechnology*, 26, 417–426, 2008.

92. E. Jaquay, L. J. Martı´nez, C. A. Mejia and M. L. Povinelli. Light-assisted, templated self-assembly using a photonic-crystal slab. *Nano Letters*, 13, 2290–2294, 2013.

93. M. J. Nuevo, J. J. Morales and D. M. Heyes. Self-diffusion coefficients and shear viscosity of model nanocolloidal dispersions by molecular-dynamics simulation. *Physical Review E*, 58, 5845-5854, 1998.

94. M. M. Kops-Werkhoven, C. Pathmamanoharan, A. Vrij and H. M. Fijnaut. Concentration dependence of the self-diffusion coefficient of hard, spherical particles measured with photon correlation spectroscopy. *Journal of Chemical Physics*, 77, 5913–5922, 1982.

95. S. Guha, L. F. Pease III, K. A. Brorson, M. J. Tarlov and M. R. Zachariah. Evaluation of electrospray differential mobility analysis for virus particle analysis: potential applications for biomanufacturing. *Journal of Virological Methods*, 178, 201–208, 2011.

96. J. R. Moffitt, Y. R. Chemla, S. B. Smith, and C. Bustamante. Recent advances in optical tweezers. *Annular Review of Biochemistry*, 77, 205–228, 2008.

97. S. J. Koch, A. Shundrovsky, B. C. Jantzen, and M. D. Wang. Probing protein-DNA interactions by unzipping a single DNA double helix. *Biophysical Journal*, 83, 1098–1105, 2002.

98. E. J. Peterman, F. Gittes, and C. F. Schmidt. Laser-induced heating in optical traps. *Biophysical Journal*, 84, 1308–1316, 2003.

99. P. R. Bianco, L. R. Brewer, M. Corzett, R. Balhorn, Y. Yeh, S. C. Kowalczykowski, and R. J. Baskin. Processive translocation and DNA unwinding by individual RecBCD enzyme molecules. *Nature*, 409,374–378, 2001.

100. A. Bosco, J. Camunas-Soler, F. Ritort. Elastic properties and secondary structure formation of single-stranded DNA at monovalent and divalent salt conditions. *Nucleic Acids Research*, 42, 2064-2074, 2014.

101. D. B. Veprintsev and A. R. Fersht. Algorithm for prediction of tumour suppressor p53 affinity for binding sites in DNA. *Nucleic Acids Research*, 36, 1589–1598, 2008.

102. M. Ferrone, F. Perrone, E. Tamborini, M. S. Paneni, M. Fermeglia, S. Suardi, E. Pastore, D. Delia, M. A.Pierotti, S. Pricl, and S. Pilotti. Functional analysis and molecular modeling show a preserved wild-type activity of p53 (C238Y). *Molecular Cancer Therapeutics*, 5, 1467–1473, 2006.

103. P. Gross, N. Laurens, L. B. Oddershede, U. Bockelmann, E. J. G. Peterman and G. J. L. Wuite. Quantifying how DNA stretches, melts and changes twist under tension. *Nature Physics*, 9, 731–736, 2011.

104. Y. Zhao, D. Chen, H. Yue, J. B. French, J. Rufo, S. J. Benkovic and T. J. Huang. Lab-on-a-chip technologies for single-molecule studies. *Lab on a Chip*, 13, 2183–2198, 2013.

105. M. C. Williams and I. Rouzina. Force spectroscopy of single DNA and RNA molecules. *Current Opinion in Structural Biology*, 3, 330–336, 2002.

106. A. A. Deniz, T. A. Laurence, M. Dahan, D. S. Chemla, P. G. Schultz and S. Weiss. Ratiometric single-molecule studies of freely diffusing biomolecules. *Annular Review of Physical Chemistry*, 52, 233–253, 2001.

107. W. K. Schroll, V. V. Prabhu, E. W. Prohofsky and L. L. Van Zandt. Phonon interpretation of inelastic neutron scattering in DNA crystals. *Biopolymers*, 28, 1189–1193, 1989.

108. H. Urabe, Y. Tominaga and K. Kubota. Experimental evidence of collective vibrations in DNA double helix (Raman spectroscopy). *Journal of Chemical Physics*, 78, 5937–5939, 1983.

109. M. Krisch, A. Mermet, H. Grimm, V. T. Forsyth and A. Rupprecht. Phonon dispersion of oriented DNA by inelastic x-ray scattering. *Physical Review E, Statistical physics, plasmas, fluids, and related interdisciplinary topics*, 73, 061909, 2006.

110. D. L. Woolard, T. R. Globus, B. L. Gelmont, M. Bykhovskaia, A. C. Samuels, D. Cookmeyer, J. L. Hesler, T. W. Crowe, J. O. Jensen, J. L. Jensen and W. R. Loerop. Submillimeter-wave phonon modes in DNA macromolecules. *Physical Review E, Statistical physics, plasmas, fluids, and related interdisciplinary topics*, 65, 051903, 2002.

111. V. N. Blinov and V. L. Golo. Acoustic spectroscopy of DNA in the gigahertz range. *Physical Review E, Statistical physics, plasmas, fluids, and related interdisciplinary topics*, 83, 021904, 2011.

112. A. Wittlin, L. Genzel, F. Kremer, S. Häseler, A. Poglitsch and A. Rupprecht. Far-infrared spectroscopy on oriented films of dry and hydrated DNA. *Physical Review A,* 34, 493–500, 1986.

113. D. L. Woolard, T. Koscica, D. L. Rhodes, H. L. Cui, R. A. Pastore, J. O. Jensen, J. L. Jensen, W. R. Loerop, R. H. Jacobsen, D. Mittleman and M. C. Nuss. Millimeter wave-induced vibrational modes in dna as a possible alternative to animal tests to probe for carcinogenic mutations. *Journal of Applied Toxicology*, 17, 243–246, 1997.

114. A. Matsumoto and W. K. Olson. Sequence-dependent motions of DNA: a normal mode analysis at the base-pair level. *Biophysical Journal*, 83, 22–41, 2002.

115. L. L. van Zandt. Damping of DNA vibration modes by viscous solvents. *International Journal of Quantum Chemistry*, 20, 271–276, 1981.

116. W. L. Peticolas. Low frequency vibrations and the dynamics of proteins and polypeptides. *Methods in Enzymology*, 61, 425–458, 1979.

117. Y. Zhang, H. Zhou and Z. Ou-Yang. Stretching single-stranded DNA: interplay of electrostatic, base-pairing, and base-pair stacking interactions. *Biophysical Journal*, 81, 1133–1143, 2001.

118. M. N.-. Dessinges, B. Maier, Y. Zhang, M. Peliti, D. Bensimon and V. Croquette. Stretching single stranded DNA, a model polyelectrolyte. *Physical Review Letters*, 89, 248102, 2002.

119. J. R. Wenner, M. C. Williams, I. Rouzina and V. A. Bloomfield. Salt dependence of the elasticity and overstretching transition of single DNA molecules. *Biophysical Journal*, 82, 3160–3169, 2002.

120. C. K. Chou and B. Mao. Collective motion in DNA and its role in drug intercalation. *Biopolymers*, 27, 1795-1815, 1998.

Appendix A. Fabrication of DNH using Template Stripping

A.1 Introduction

Template stripping provides high throughput, reproducible and low cost alternative approach for fabricating DNH for optical trapping applications. Some of the techniques that have been used to fabricate nanoapertures are the electron beam lithography (EBL), the nanosphere lithography and the focused ion beam (FIB). Electron beam lithography with ion etching has been used to create conical apertures in gold films with sizes of approx. 10 nm. In spite of the reliability of the process it suffers from scalability. It cannot be used to produce large quantity of nanoapertures as it is a serial process and therefore too time consuming. The nanosphere lithography provides the ability to produce large number of apertures in a single batch process but suffers from the positioning capabilities in comparison to the EBL process. The focused ion beam technique which has been used in this thesis to make the DNH structure work pretty well, with great precision. But the FIB suffers from limited feature size of DNH, high cost and time consuming for mass production. So in this thesis, we suggest an alternative approach of template stripping which provides the required position control along with obtaining smaller feature size and large quantity of production of double nanohole. This brings down the cost by approximately 70 % for a single chip in a single batch process as opposed to that made by FIB. Template stripping has been used to produce large atomically flat surfaces earlier. The silicon wafer is used as a template to make structures such as grooves, pyramids, holes ridges and so on which can be used for different

applications in the field of plasmonics and metamaterial. It allows making structures with sharp features as small as 2 nm which have been demonstrated previously.

A.2 Template Stripped DNHs

The fabrication of template stripped DNH is outlined as follows:

Silicon master preparation

The first step of the process is the fabrication of a silicon master template with the desired double nanohole structures. This is done using a focused ion beam to make nanostructures on clean silicon wafer as shown in Figure A.1. The crystalline nature of the silicon allows for making DNH with high aspect ratio features important for template stripping. It should be noted that the milling depth of the DNH pattern should be large enough so that the gold film is not connected, when stripped off to produce an aperture. In the present case the DNH structure were milled in silicon for depth greater than 100 nm in order to make apertures on a 100 nm gold film.

Gold layer deposition

The second step involves the deposition of gold layer on the silicon template. The gold layer is deposited on silicon by direct evaporation of gold at a rate of 0.2 nm/s. A 100 nm gold film was evaporated on silicon in the present case as shown in Figure A.1 (step2).

Stripping

The final step uses a microscopic glass slide with a very thin layer of UV epoxy on one side as shown in Figure A.1 (step 3). The slide containing the UV epoxy is then gently pressed on the silicon template with the gold layer as shown in Figure A.1 (step 4). The sandwiched structure containing the silicon, gold, epoxy and glass is then exposed to UV light source for bonding of the epoxy to the gold. After the epoxy is adhered to the gold the glass slide is stripped apart from the silicon template. Due to strong bonding between gold and epoxy as compared to gold and silicon the gold layer gets attached to the epoxy. Thus the DNH structures pattern are transferred from the silicon template to the glass slide as shown in Figure A.1 (step 4). The gold left on the silicon template can then be etched using standard gold etchant such as Aqua Regia, in order to reuse the silicon template to produce more gold samples containing the DNH structure.

Template stripped DNH imaging

A scanning electron microscope (Hitachi S-4800 FESEM) was used to image the DNH structures made on the silicon template using FIB and the corresponding DNH made on the gold film using the template stripping process described above. Figure A.2 (a & b) shows the SEM image of DNH obtained from the template stripping process described in the above section. Figure A.2 (c & d) shows the SEM image of the DNH on silicon master template fabricated using FIB milling and subsequently used for template stripping process. The SEM images of DNH on silicon were also taken after the template stripping process and removal of gold residue with a gold gold etchant solution. There

was no significant damage observed after initial fabrication runs. Some of the previous work also suggests that these masters could be re-used almost indefinitely with care.

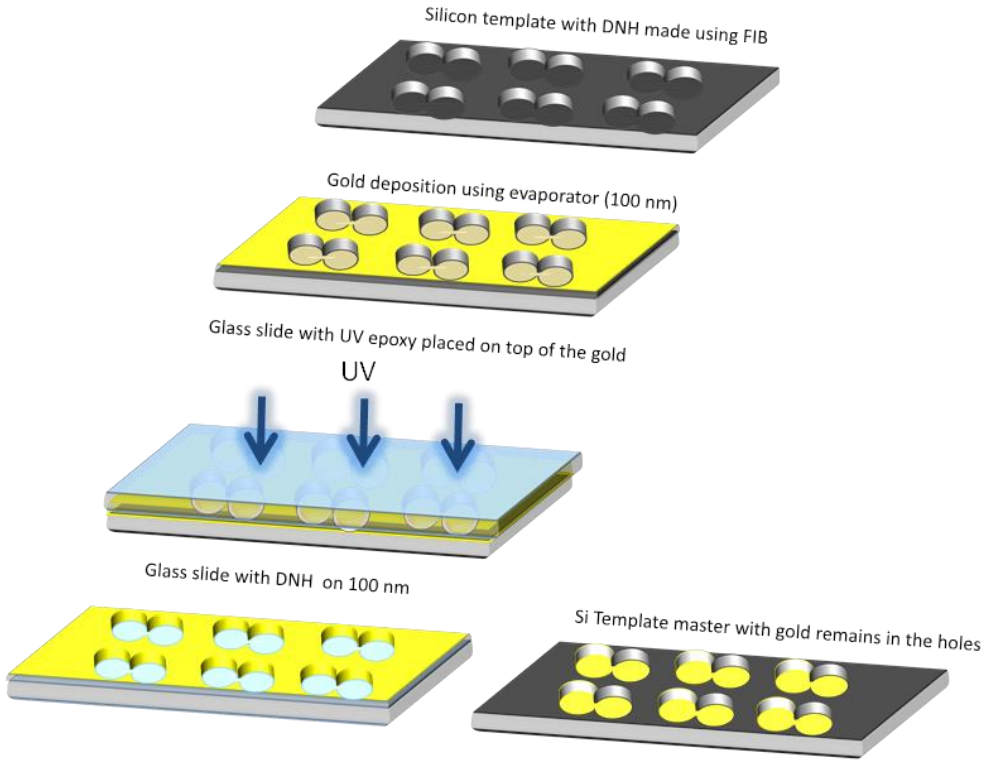

Figure A.1 Process flow for fabrication of template stripped DNH.

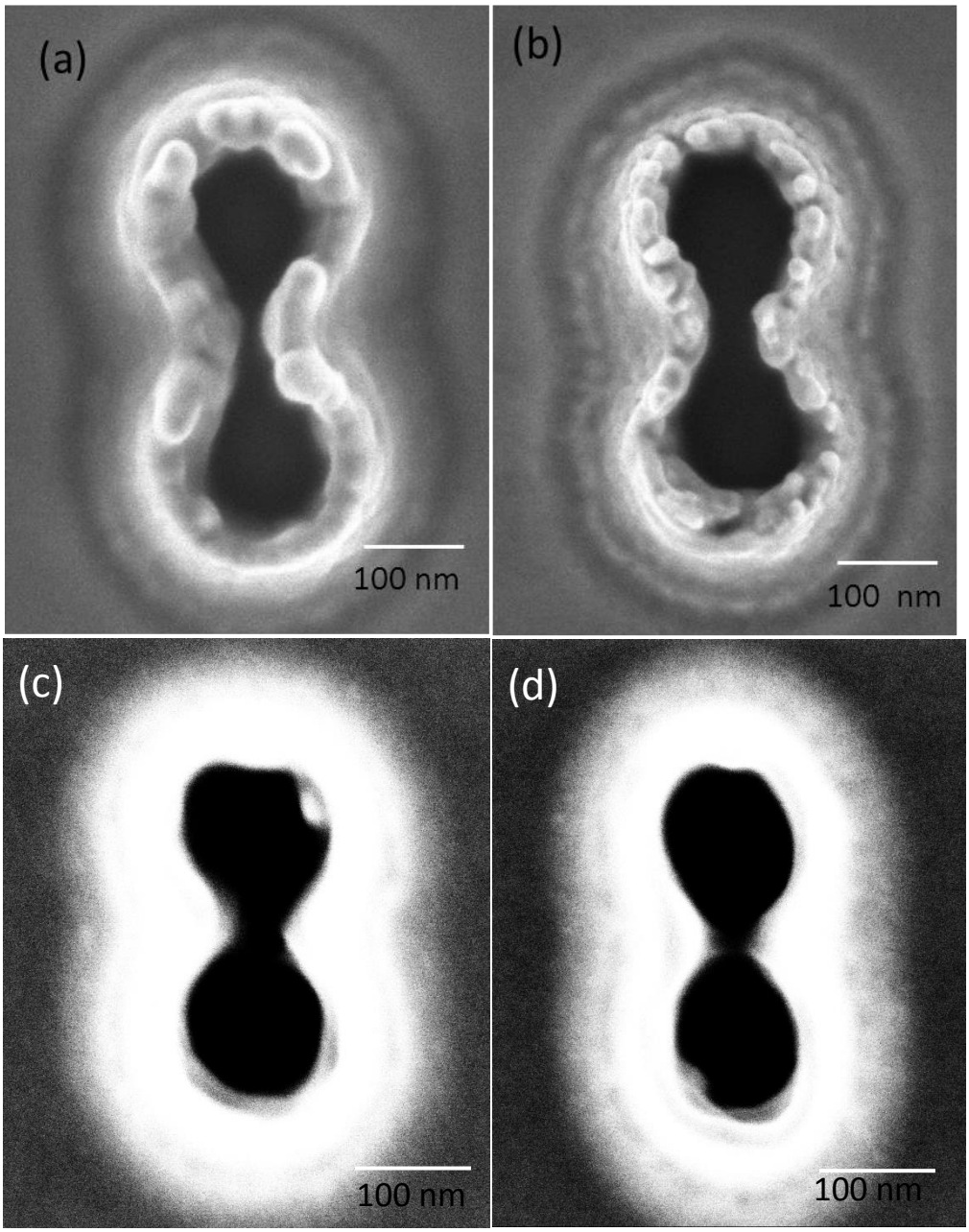

Figure A.2 (a, b) Template stripped DNH fabricated from the silicon template shown in Figure c and d respectively.

From the Figure A.2, it is clear that the template stripped DNHs have nearly similar nanoscale features as the DNHs on the silicon template. An important feature which plays

an important role in trapping is the gap between the cusps of DNH. A point to note is that using this technique it is possible to produce gap sizes smaller than that expected from the silicon template structure. This is due to a curved depth profile of the gap on silicon near the top surface due to the fabrication from the FIB. This results in the fabrication of much smaller gap sizes of size as small as 5 nm, which might be very difficult to produce by direct fibbing of DNH on gold using the FIB. We could repeat the fabrication of the DNH structures frequently and they were used successfully for trapping of the nanoparticles and biomolecules.

Appendix B. Microfluidic DNH Chip for Sensing Applications

B.1 Microfluidic Chip for Optical Trapping

The integration of a microfluidic channel with the DNH tweezer is an important technique in order to perform experiments such as, the in-situ binding, the flow measurements and for other possible optical trapping applications. In this thesis, the microfluidic chip was only used in the sensing experiments described in Chapter 4, just to provide a stationary environment along with similar local conditions during optical trapping of different concentrations and sizes of nanoparticles. This is in order to minimize the influence of the external environment and the microfluidic arrangements, which might change if the solution chamber is changed every time for a different nanoparticle solution, thereby influencing the diffusion of the nanoparticles and hence the results of the experiment. In order to address this particular consideration and seeing possible applications of the microfluidic integration, it is important to describe the fabrication process of the microfluidic channel integration with DNH tweezer.

This appendix describes the procedure for fabricating a microfluidic chip along with the integration of the DNH made on gold substrates. The fabrication process results in a microfluidic channel, which is used to hold a stationary nanoparticles solution in the optical trapping setup. This microfluidic channel consist of a NO.0 glass coverslip (90-130 μm thick) and 80 μm thick PDMS (Polydimethylsiloxane) which acts as a spacer.

Process:

PDMS base (Sylgard184 Silicone Elastomer Base, Dow Corning Canada) is mixed with Sylgard 184 Silicone Elastomer Curing Agent (Dow Corning Canada) in a ratio of 10:1. The PDMS mixture is then placed inside a vacuum chamber for approximately 30 minutes in order to make it smooth without any bubbles. Thereafter a small amount is poured onto the glass coverslip which is mounted on a spin coater mount (Specialty Coating System G3P-8 Spin-Coat System). The glass coverslip is then rotated at a spin rate of 500 rpm for 10 s for spreading, and then at a spin rate of 1000 rpm for 60 s. This results in the formation of an 80 μm PDMS layer on top of the glass coverslip. The coverslip covered with PDMS mixture is then degasified in a vacuum chamber for 30 minutes to remove any air bubbles between the coverslip and the PDMS mixture. The coverslip-covered PDMS mixture is then baked on a hot plate for 10 minutes to harden the PDMS. A small PDMS layer is cut out on the cover slip to make the microfluidic channel as shown in Figure B.1 (left).

The above process is repeated again. Now, a window of about 3 mm by 3 mm in size is cut at the center of the coverslip and removed from the PDMS to make the solution chamber as shown in Figure B.1 (Right). The PDMS layer with the hole at the center of the coverslip is then peeled off from the glass coverslip and placed on top of the channel made on the previous cover slip. The gold sample containing the DNH structure is placed on top of this hole such that the DNH lie within the intersection of the solution chamber and the channel cut on PDMS as shown in Figure B.1 (center). The whole configuration

is then placed in another petri dish and PDMS is poured into it such that it covers all the parts. In this step the PDMS will penetrate below the cover slip and lift it a little. Next, the PDMS is baked and two holes are punched for tubing. Four holes are punched for screws, which hold the whole configuration on an aluminum clamp. Wiring is used in order to support the tubes so that any movement does not affect that tubes' fitting. Figure B.2 shows the chip configuration view from top and side and also the aluminum clamp.

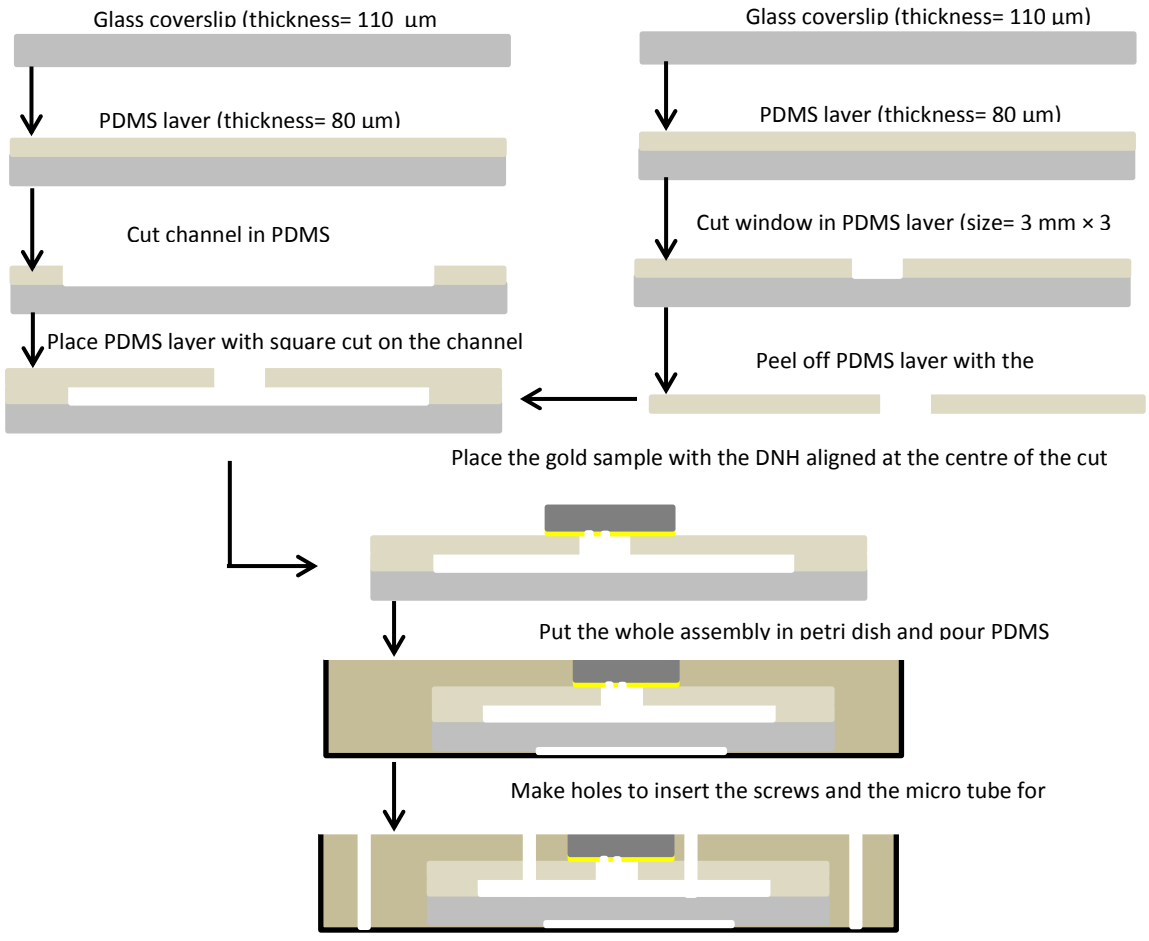

Figure B.1 Fabrication procedure flow diagram showing the making of a microfluidics chip along with DNH integration.

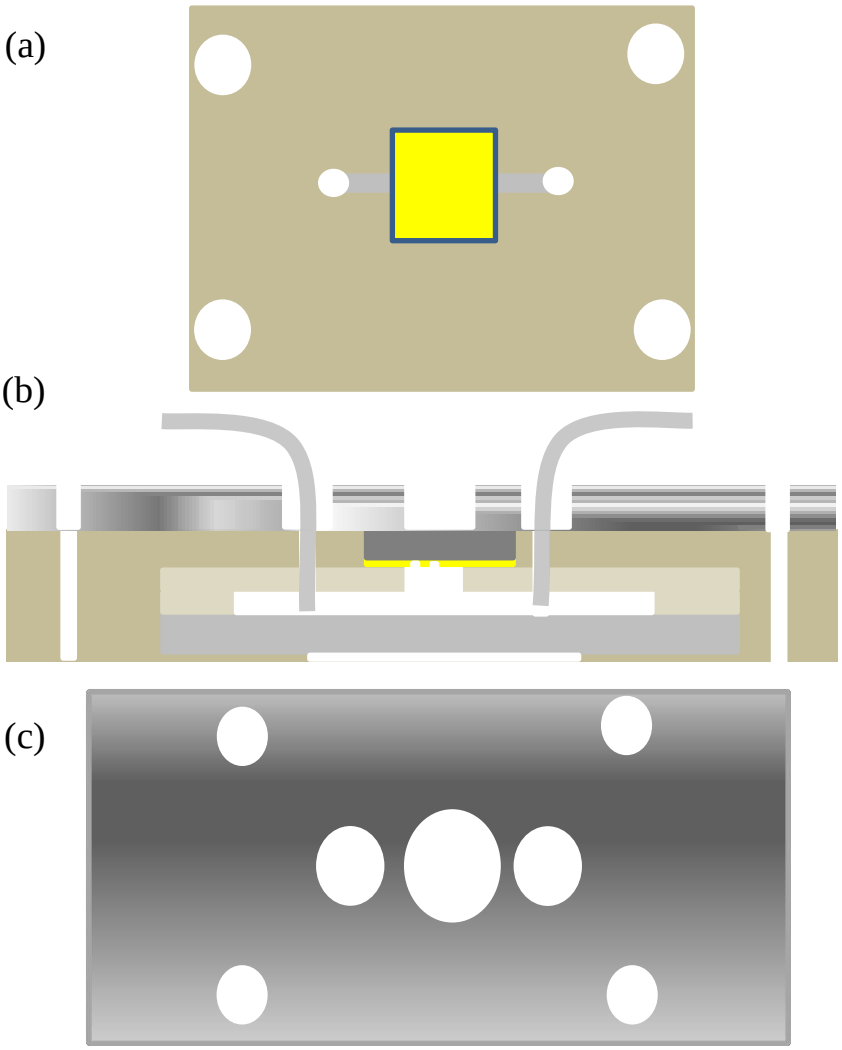

Figure B.2 (a) Top view of the chip. (b) Side view of the chip. (c) Aluminum clamp.